REVIEW

Check for updates

From metal–organic framework powders to shaped solids: recent developments and challenges

Bakytzhan Yeskendir,[ab] Jean-Philippe Dacquin, [ID][a] Yannick Lorgouilloux, [ID][b] Christian Courtois, [ID][b] Sébastien Royer [ID][a] and Jérémy Dhainaut [ID]*[a]

Metal–organic frameworks represent a class of porous materials which have developed considerably over the past few years. Their highly porous structure makes them outperform conventional adsorbents in hot topics such as dihydrogen and methane storage, and carbon dioxide capture. Their consequent modularity, based on the assembly of organic linkers and metal ions or clusters, also brings novel perspectives in catalysis, sensing and drug delivery just to name a few. However, one of the main bottlenecks to their broader use remains their shaping. Especially, shaped materials should present long-term mechanical stability as well as preserve their physical and chemical properties. This makes shaping of MOFs a special case as their thermal and chemical stabilities remain a downside as compared to other traditional porous materials such as silicas and zeolites today. Therefore, ever-increasing efforts have been devoted to the shaping of these materials. In this review, the state of the art for the preparation of shaped 3D MOF-based materials will be presented. Emphasis will be given to the final physical and chemical properties of the shaped solids comparatively to the initial powders, when data are available. In the first part, traditional techniques based on applying a significant force to MOF-based powders will be reviewed. These include pelletization, granulation, and extrusion, which generally lead to an increase of the final volumetric gas uptake of the objects. At the same time, the advantages and disadvantages of each technique will be discussed as well as the main outcome on the final objects. In the second part, the focus will be on newly-emerging techniques such as 3D printing and spray drying. The former also maximizes the volumetric gas uptake of the final materials, and for both techniques the quality of the final objects heavily relies on the working parameters. Finally, the third part will include the so-called "phase separation" shaping techniques which are for the most part performed without using special techniques. This implies shaping *via* physical and chemical phenomena such as sublimation and precipitation. Subsequently, a discussion on the performance of these materials for adsorption-based applications will be provided. Finally, perspectives and future outlook will be discussed.

Introduction

Metal–Organic Frameworks (MOFs; also called Porous Coordination Polymers, PCPs) have attracted a great deal of attention since they were first described in 1995 and developed in the early 2000s.[1,2] They represent a new class of hybrid crystalline microporous materials as they are composed of metal nodes (ions or clusters) bound together by multitopic organic linkers. Such coordination allows for an eventual 1-, 2- or 3-dimensional

framework. In most cases, the metal core is formed from transition metals, while the linker is often comprised of cyclic organic compounds presenting carboxylate groups or N-donors. Over the past decades, researchers from all over the world have probed a significant number of different combinations of metal precursors, organic linkers, and synthesis conditions, leading to the discovery of many new MOF structures. Nowadays, this denomination includes several thousand structures including the famous HKUST-1,[3] UiO-66,[4] ZIF-8[5] and MIL-101.[6]

Owing to their low density and exceptionally high surface area, MOFs have found an initial application as adsorbents in gas separation and storage. Indeed, the available surface area of MOFs can exceed multiple times those of the most well-known porous materials such as zeolites, silicas and activated carbons. According to numerous studies, MOFs outperform most

[a] *Univ. Lille, CNRS, Centrale Lille, Univ. Artois, UMR 8181 – UCCS – Unité de Catalyse et Chimie du Solide, F-59000 Lille, France. E-mail: jeremy.dhainaut@univ-lille.fr*

[b] *Université Polytechnique Hauts-de-France, EA 2443 – LCMPA, 59600 Maubeuge, France*

benchmark adsorbents in terms of gas adsorption[7]. Moreover, MOFs can be subjected to structural modifications by varying the metal node and/or the organic linker *via in situ* or post-synthesis treatments. This, in turn, implies the textural and chemical tunability of MOFs and therefore expands their application to catalysis,[8] drug-delivery,[9] sensing,[10] water purification,[11] and energy storage,[12] just to name a few. Besides, MOFs have been shown to be excellent templates for the production of high-performance materials, following mainly pyrolysis or chemical leaching. A wide variety of MOF-derived nanostructured materials can be obtained, including porous metal oxides, carbides, phosphides, carbons, doped carbons and composites.[13] The unique chemical compositions and pore architectures inherited from the parent MOFs make these materials suitable for unique applications in catalysis[14] and energy storage.[15–17]

Typically, MOFs are produced in polycrystalline powder form, with the size of individual crystals ranging from several tens of nanometers to a few microns. Continuous studies on synthesis optimization and product characterization have stimulated the production of MOFs on a larger scale. Thus, a number of them are now commercially available and provided by BASF (HKUST-1/Basolite C300, ZIF-8/Basolite Z1200, Fe-BTC/Basolite F300), Strem Chemicals (CAU-10, MIL-53(Al), MIL-101(Al), PCN-250(Fe), UiO-66), and others.

Usually, powders are not convenient to use in big industrial reactors as they cause several difficulties from the processing point of view. They induce, for example, consequent pressure drops within the reactor bed. In addition to that, powders can induce clogging, and it is generally complicated to handle and recover them, as they involve additional costly separation steps. In order to overcome these issues, MOF powders should be

Bakytzhan Yeskendir received his MSc in Chemistry and Spectroscopy in 2018 within the framework of the Advanced Spectroscopy in Chemistry Master Program funded by Erasmus Mundus. He is now pursuing his PhD in materials science in the fields of synthesis, characterization, upscaling and shaping of materials for application in catalysis and gas adsorption, with special interest in the design of catalysts and adsorbents based on Metal–Organic Frameworks and zeo-

Bakytzhan Yeskendir

lites, as collaborating work between the MATCAT group led by Pr. Sébastien Royer at the Université de Lille and the LMCPA led by Pr. Christian Courtois at UPHF.

Jean-Philippe Dacquin obtained his PhD from the Université Sciences et Technologies de Lille 1 (France) in 2008. After two postdoctoral years at the Cardiff Catalysis Institute following the University of York with Karen Wilson and Adam F. Lee, he returned to the University of Lille where he holds a position of Associate Professor. He's the administrative head of the bachelor of Chemistry and teaches courses on inorganic chemistry and analytical chemistry. His research is devoted

Jean-Philippe Dacquin

to the preparation of solid catalysts with controlled porosity and their application in environmental catalysis.

Yannick Lorgouilloux was born in France in 1981. He graduated from the University of Limoges, France, with a master's degree in Industrial Ceramics in 2004. After working for 6 years on powder synthesis for heterogeneous catalysis (PhD in 2007 in Mulhouse, France, and 3 years of post-doc in Leuven, Belgium), he is now an Associate Professor at the Polytechnic University Hauts-de-France. His main research activities deal with the control of the porosity and

Yannick Lorgouilloux

microstructure of ceramic materials for various applications, such as piezoelectric materials, transparent ceramics and hierarchically porous catalytic monoliths.

Christian Courtois was born in France in 1963. He graduated from the University of Limoges, France, with a PhD degree in Ceramics and Surface Treatments in 1992. Since 1993 as Associate Professor then Professor at the Université Polytechnique Hauts de France, his research deals with powder synthesis, and control of the microstructure of ceramic materials for various applications, mainly for piezoelectric and other electric materials, and hierar-

Christian Courtois

chically porous catalytic monoliths.

Table 1 Shaped bodies for different types of reactors. Adapted from ref. 18

Shaping technique	Object dimensions (mm)	Shape	Type of reactor
Pelletization	d = 3–15 h = 3–15	Pellets	Fixed bed reactor
Extrusion	d = 1–50 h = 3–30	Extrudates	Fixed bed reactor
Granulation	d = 1–20	Beads	Fixed bed reactor
Spray-drying	d = 0.02–0.2	Microspheres	Fluidized bed reactor

formulated into packed objects with defined size and dimensions. This process is called "shaping" and generally represents the compaction of individual crystallites into millimeter-sized objects. Shaping allows for production of easily-handled objects required for industrial processes and generally has a few objectives:

(1) formulation of powders into mechanically stable objects to withstand a variety of process conditions (elevated pressure, gas/liquid flow, mixing);

(2) reduction of mass transfer limitations within the reactor volume; and

(3) preservation of the physico-chemical properties of the pristine powder.

The latter represents the major challenge especially for MOFs as they are prone to drastic losses in terms of available surface area and pore volume upon the formulation process. Nowadays, there are plenty of shaping techniques available which enable formulation of powders into shaped bodies for use in different types of reactors (Table 1).

Therefore, each of the shaping techniques provides unique features to the final objects in terms of size and appearance for a defined application. This review will focus on conventional shaping techniques such as granulation, pelletization, extrusion, and spray-drying and challenges associated upon

formulation of MOF powders. This will also include the 3D printing method as it can be referred to as a type of extrusion with controlled deposition of the forming paste in three dimensions in space. Therefore, 3D printing allows shaping powders with desired shapes and dimensions for a wide variety of applications. They will be as well discussed in the corresponding section along with the challenges related to the formulation of MOF powders. Besides, a separate section will be dedicated to the so-called non-conventional techniques which include freeze granulation, ice templating and biopolymer precipitation. Membranes and coatings, and sol–gel-based monoliths have been excluded from this review on purpose as they have been recently reviewed.[19]

This review includes discussions on the specifics of each shaping technique such as the influence of pressure on raw powders and their textural properties upon pelletization, or the appropriate choice of a binder for granulation and extrusion. Working parameters for 3D printing and spray-drying will be considered as well. Moreover, special cases where certain MOFs are not eligible for being shaped by one or another technique will be highlighted. This depends on the nature of the parent MOF determined by the coordination state of the metal and the organic ligand. Consequently, to date, shaping has been mostly applied to a few MOF structures summarized in Table 2.

Pelletization

Pelletization (also referred to as "pressing", "compressing" or "tableting") is the most widely used shaping technique and represents the compaction of powder particles by applying pressure. Owing to its simplicity, pelletization is the first shaping technique to have been applied on an industrial scale. Overall, this method implies pressing powder in a die by applying a uniaxial pressure of several tenths of MPa with a

Sébastien Royer obtained his PhD in Chemical Engineering from Laval University – QC – CA in 2004. Since 2015, he has been Full Professor at the University of Lille – FR. He leads the MATCAT research group from UCCS laboratory as well as the UPCAT technological platform devoted to the study of catalyst scale-up (up to 10 kg) and shaping. S. Royer has done research in the fields of catalytic materials engineering, with interest in control of porosity (mesoporous, macroporous, and hierarchical porosity), dispersion and stability of metallic elements, long term stability and regeneration procedures, characteristics of shaped catalysts.

Sébastien Royer

Jérémy Dhainaut received his PhD in Chemistry of Materials from the University of Upper Alsace (Mulhouse) in 2012. He further developed an expertise in the fields of porous materials and their shaping through postdoc positions at the Ceramic Synthesis and Functionalisation Laboratory (Cavaillon), the Institute of Research on Catalysis and the Environment (Lyon), the Laboratory of Catalysis and Solid-State Chemistry (Villeneuve d'Ascq), and the Institute for Integrated Cell-Material Sciences (Kyoto). In 2019, he was appointed as a CNRS Researcher at UCCS. His work focuses on studying the effect of shaping methods on the physico-chemical properties of porous materials including MOFs.

Jérémy Dhainaut

Table 2   Schematic representation of some of the reviewed MOF structures

MOF	Space group	Metal cluster	Organic linker	Framework
HKUST-1	$Fm\bar{3}m$	Cu^{2+}	Benzene-1,3,5-tricarboxylate	
MOF-5	$Fm\bar{3}m$	Zn^{2+}	Benzene-1,4-dicarboxylate	
ZIF-8	$I\bar{4}3m$	Zn^{2+}	Imidazolate	
MOF-74	$R\bar{3}$	$Ni^{2+}, Co^{2+}, Mg^{2+}$	2,5-dihydroxybenzene-1,4-dicarboxylate	
MIL-53	$Imma$	Al^{3+}	Benzene-1,4-dicarboxylate	
UiO-66	$Fm\bar{3}m$	Zr^{4+}	Benzene-1,4-dicarboxylate	
MOF-801	$Pn\bar{3}$	Zr^{4+}	Fumarate	

punch (Fig. 1). Some configurations are based on both upper and lower punches moving towards each other; however, in most configurations one punch remains stationary. In order to achieve maximum compaction, the punches may be left in the compression position for a certain time before recovering the final shaped object. Typically, this process yields cylinder or oblong-type shaped bodies which are called "pellets" or "tablets".

The process parameters entirely depend on the initial powder to be shaped. Mainly, the pressure applied on it should be carefully selected to avoid the complete destruction of the crystal structure (amorphization) and therefore loss of intrinsic
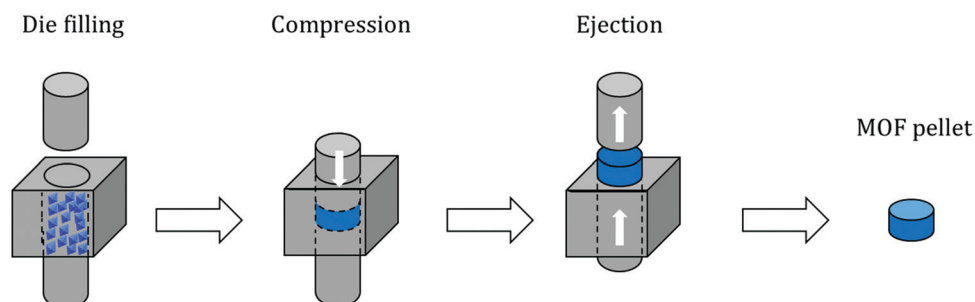

Fig. 1   Schematic representation of the pelletization process applied to polycrystalline MOF powder.

Table 3 Effect of the pelletization process on the textural properties of MOFs

MOF	Metal/linker	Binder, wt%	Applied pressure, MPa	S_{BET}, m^2 g^{-1} Powder	Pellet	Ref.
MOF-5	Zn/BDC	None	180	2160	275 (−87%)	25
MOF-5	Zn/BDC	None	10.3	3450	6 (−99%)	26
MOF-5	Zn/BDC	None	2	2777	1450 (−48%)	27
MOF-5	Zn/BDC	None	80	2762	∼1600 (−42%)	28
MOF-177	Zn/BTB	None	—	4100	3300 (−20%)	32
MIL-53	Al/BDC	PVA, 13	None	—	—	23
MIL-53	Al/BDC	—	—	830	601 (−28%)	34
MIL-53	Al/BDC	—	—	—	560	35
MIL-53	Al/BDC	None	125	796	538 (−32%)	37
ZIF-8	Zn/MIM	None	125	1983	1736 (−12%)	37
ZIF-8	Zn/MIM	None	300	1774	1551 (−13%)	38
ZIF-8	Zn/MIM	None	229	1433	1278 (−11%)	39
ZIF-8	Zn/MIM	Talc	24	1187	951 (−20%)	40
ZIF-8	Zn/MIM	SB	24	1187	959 (−19%)	40
SIM-1	Zn/MIC	None	400	516	370 (−28%)	39
MIL-100	Fe/BTC	Graphite, 3	34	2088	1300 (−38%)	57
MIL-101	Cr/BDC	None	—	2602	2602 (−28%)	41
MIL-101	Cr/BDC	None	—	3677	3302 (−10%)	43
MIL-101	Cr/BDC	None	—	3414	2745 (−20%)	42
MIL-101	Cr/BDC	Al tapes[a]	—	3814	2955 (−23%)	44
MIL-101	Cr/BDC	Graphite, 3	34	4066	2660 (−35%)	57
CPO-27	Ni/DHBDC	None	100	1060	1050 (−1%)	45
MOF-74	Mg/DHBDC	None	30	1249	1034 (−17%)	46
HKUST-1	Cu/BTC	None	180	1145	470 (−59%)	25
HKUST-1	Cu/BTC	None	69	1698	892 (−47%)	47
HKUST-1	Cu/BTC	None	5	1737	1007 (−42%)	48
HKUST-1	Cu/BTC	None	121	1288	1091 (−15%)	49
HKUST-1	Cu/BTC	Graphite, 2	112	1288	949 (−26%)	49
HKUST-1	Cu/BTC	None	24	1897	1377 (−27%)	39
HKUST-1	Cu/BTC	None	400	1897	476 (−75%)	39
UiO-66	Zr/BDC	None	69	1080	1090 (=)	47
UiO-66	Zr/BDC	Graphite, 1	—	1140	885 (−22%)	52
UiO-66	Zr/BDC	None	18	1426	1459 (−)	49
UiO-66	Zr/BDC	None	665	1737	1707 (−2%)	53
UiO-66	Zr/BDC	PVA, 9.3	—	1378	1195 (−14%)	54
UiO-66-NH$_2$	Zr/NH$_2$-BDC	None	127	1182	876 (−26%)	51
UiO-66-NH$_2$	Zr/NH$_2$-BDC	None	164	839	625 (−26%)	49
UiO-66-COOH	Zr/BDC-COOH	None	9.7	710	614 (−14%)	55
UiO-67	Zr/BPDC	None	63	2034	1549 (−24%)	49
MOF-801	Zr/FA	PVB, 5	146	899	569 (−37%)	58

Linker codes: BDC – benzene-1,4-dicarboxylic acid; BTB – 1,3,5-benzenetribenzoate; MIM – 2-methyl imidazole; MIC – 4-methyl-5-imidazolecarboxaldehyde; BTC – benzene-1,3,5-tricarboxylic acid; DHBDC – 2,5-dihydroxy-1,4-benzenedicarboxylic acid; BPDC – biphenyl-4,4′-dicarboxylic acid; and FA – formic acid. Binder codes: PVA – polyvinyl alcohol; SB – pseudoboehmite; and PVB – polyvinyl butyral. "—" not specified. [a] Used as an additive to improve thermal conductivity.

properties. Additionally, the rate of pressure increase should be adequate for the same reason.

The primary goal of pelletization is the formation of densely packed pellets for further employment in large fixed-bed type reactors, or transportation applications in the specific case of MOFs. Many industrial processes rely on using such pellets as adsorbents and catalysts. Indeed, it is easier to handle shaped objects than their powder analogues. Besides, they minimize the risk of a pressure drop, afford an enhanced mixing and distribution inside the bed volume and therefore allow for more efficient production processes. These are achieved upon providing the pellets with pronounced resistance to attrition and breakage.

Compaction itself serves as a source of reinforcement; however, sometimes the use of binders to enhance the mechanical stability of pellets is of particular interest. Binders are usually classified into organic binders such as starch, cellulose and polyvinyl alcohol (PVA) and inorganic binders such as clays, silica and graphite.[20] They facilitate bonding of individual particles by generating a link between them. As an example, it was shown that zeolites X and Y could be pelletized using bentonite as the binder,[21] and kaolinite could be employed to bind ZSM-5 zeolite crystals together.[22] In both cases there is an alteration of both the physical and chemical properties of the final materials compared to the pristine zeolites.

Generally, pelletization leads to drastic losses of textural properties when applied to highly-porous materials. MOFs are especially sensitive to these losses as their frameworks are more fragile and flexible than frameworks composed of inorganic building units. This becomes even more pronounced when pelletization is performed with a binder. Although protocols found for pelletization can largely differ in the literature, Table 3 illustrates the effect of pelletization on MOFs depending on the metal oxidation state and associated linker.

As is evident from the results presented in Table 3, the pelletization process leads to drastic decreases of textural properties as evaluated by the specific surface area, and especially in the case of metals with low coordination (Cu, Zn) – with the notable exception of ZIF-8. High applied pressure reduces interparticular voids and can even collapse the frameworks, while addition of binders leads to pore blocking. One of the earliest studies on pelletization of MOFs was performed by Finsy et al.[23] who studied CO_2/CH_4 adsorption on Al-based MIL-53 pellets. Particularly, in their work the MOF was mixed with the binder, an aqueous solution of polyvinyl alcohol, and upon homogenization heated at a rate of 0.5 °C min^{-1} up to 190 °C. Such a procedure yielded pellets with a binder content of 13 wt%, which were then used for CO_2/CH_4 mixture adsorption. Although no pressure was applied to form pellets, the total accessible pore volume decreased by 19 wt%, which exceeds the content of PVA and suggests partial pore blocking. Following this, the authors further studied the binderless pelletization of V-based MIL-47 to separate xylene isomers[24].

MOF-5

Among other early studies, there is a study by Alcañiz-Monge et al.[25] addressing the effects of compression on the textural properties of MOF-5 compared to silica and zeolites. Typically, each solid was compressed in a 1.45 cm diameter die up to 420 MPa. As expected, the specific surface areas and pore volumes decreased when the applied pressure increased. Predictably, inorganic solids exhibiting frameworks with high mechanical strength were less affected by compression and therefore less prone to drastic losses in surface area. In contrast, MOF-5 whose framework is formed by coordination bonds has lower mechanical strength and is therefore heavily affected by compression. Indeed, its compression at 180 MPa led to a severe broadening of reflections in the XRD pattern, suggesting structural collapse of the framework. This was supported by N_2 physisorption measurements which yielded an extremely low surface area of 275 m^2 g^{-1} for the pellet as compared to 2160 m^2 g^{-1} for the parent powder. Considering these observations, this allows setting up an upper limit for compression forces applied to MOF-5 to 180 MPa, at which this MOF experiences quasi-total structural collapse.

In another early study on MOF-5, Hu and Zhang[26] demonstrated its irreversible amorphization starting from 3.5 MPa. Indeed, the authors showed evidence of peak broadening in the XRD patterns as the compression pressure increased. Moreover, Raman spectroscopy revealed that the MOF-5 structure collapsed via the breaking of the bond between Zn-clusters and the BDC linker. Therefore, upon compression up to 10.3 MPa the final BET surface area was only 6 m^2 g^{-1} as compared to 3450 m^2 g^{-1} of the pristine powder. Further studies on MOF-5 pelletization include the study by Jia et al.[27] who used the MOF for methane adsorption at ambient temperature. The results suggest that a mild compression pressure of up to 2 MPa applied to the MOF-5 powder led to a decrease of the BET surface area from 2777 to 1450 m^2 g^{-1}. The MOF-5 pellet retained around 50% of its initial surface area; however,

volumetric methane uptake measurements revealed lower values when compared to the initial powder. Thus, the MOF-5 volumetric methane capacity was stated to be overestimated. Therefore, later studies on MOF-5 mainly aimed at hydrogen storage. Purewall et al.[28] conducted a study on MOF-5 densification to improve its volumetric hydrogen uptake. Typically, they evaluated the performance of the MOF upon manual pressing until the desired density was reached. Noteworthily, they observed the preservation of the crystal structure and therefore no transformation into an amorphous phase even when pressing the powder until a bulk density of 0.75 g cm^{-3} was reached, which corresponded to approximately 80 MPa applied compression pressure. This is in agreement with earlier studies[25] and differs from the one obtained by Hu and Zhang.[26] Nevertheless, the specific surface area decreased accordingly with increasing pressure, from 2762 m^2 g^{-1} for the pristine powder to 1188 m^2 g^{-1} for the pellet with a bulk density of 0.90 g cm^{-3}. In agreement with that, the hydrogen adsorption capacity varied accordingly. Thus, a densified pellet of 0.51 g cm^{-3} demonstrated a 3.5 times increase in excess volumetric hydrogen uptake, reaching 26 g L^{-1}, with only a 15% decrease in gravimetric uptake at −196 °C as compared to its powder counterpart. Additionally, the authors performed a complementary study[29,30] to address the enhancement of thermal conductivity of the densified MOF-5 pellets, an important parameter defining the hydrogen refueling rate and therefore the material's efficiency. Adding 10 wt% expanded natural graphite (ENG) as an additive (Fig. 2a) increased the thermal conductivity of the final MOF-5/ENG composites by a factor of 5 while decreasing the volumetric hydrogen uptake only by 6% as compared to the neat MOF-5 pellet of 0.51 g cm^{-3}. Interestingly, they further showed that pelletization of MOF-5 (Fig. 2b and c) improved its stability against water as it slowed down subsequent degradation under moderately humid conditions.[31]

MOF-177

Zacharia et al.[32] studied the volumetric hydrogen uptake capacities of MOF-177 pellets prepared by compression. It is worth mentioning that this Zn-based MOF is commercially available, making it interesting for large-scale applications. The authors applied various pressures to prepare monoliths with different densities. It was found that above 0.51 g cm^{-3} MOF-177 underwent amorphization as the XRD patterns of MOF-177 upon compression exhibited broad reflections. Moreover, its BET surface area decreased accordingly from around 4100 m^2 g^{-1} for the pristine powder to 3300 and 2400 m^2 g^{-1} for pellets compressed to bulk densities of 0.51 and 0.59 g cm^{-3}, respectively. Noteworthily, when assessed for hydrogen adsorption at −196 °C and ∼8 MPa, the total H_2 uptake reached 41 g L^{-1} over the MOF-177 pellets with a bulk density of 0.53 g cm^{-3}. Under the same conditions the total H_2 uptake reached 41 g L^{-1} at 8 MPa on MOF-5 pellets with a bulk density of 0.51 g cm^{-3}.[28] Dailly and Poirier[33] further evaluated the hydrogen uptake on MOF-177 pellets provided by BASF over a wide range of temperatures. The results suggest that at −196 °C and 4 MPa, MOF-177 pellets exhibited around 36 g L^{-1} total H_2 volumetric

Fig. 2   Pure MOF-5 pellets and MOF-5/ENG (expanded natural graphite) composites (a) made by Liu et al.[30] Copyright 2012 Elsevier. MOF-5 powder (b) and pellets (c) prepared by Ming et al.[31] Copyright 2015 American Chemical Society. Hexagonal MIL-101 monoliths (d) prepared by Blanita et al.[43] Copyright 2014 Elsevier. MIL-100 granules (e and f) with an average size of around 1 mm made from compressed pellets by Yang et al.[56] Copyright 2019 American Chemical Society.

uptake. It is in a good agreement with the values reported by Purewall et al.[28] and considerably higher than that of the pristine powder, 26 g L^{-1} reported by Zacharia et al.[32]

MIL-53

Al-based MIL-53 is also among the commercially available MOF structures, and is therefore readily available for gas studies. Thus, Heymans et al.[34] applied the densified MIL-53 supplied by BASF for gas separation. Namely, they used it for the separation of CO_2 and H_2S from a stream of CH_4. The results demonstrated preferential adsorption of H_2S over CO_2 and CH_4 at 30 °C over a range of gas pressures. At the same time, it was shown that MIL-53 in pellet form adsorbed less H_2S as compared to its powder counterpart (8 vs. 10 mol kg^{-1}) – a regular phenomenon upon densification. Noteworthily, the total CO_2 uptake decrease upon densification was consistent with the decrease in pore volume and was nearly 20%. Besides, Moreira et al.[35] showed that MIL-53 could also be used as an adsorbent for liquid phase separations. This MOF exhibited preferential adsorption of o-xylene and therefore a certain capacity of separation from a mixture with p- and m-isomers. The work of Majchrzak-Kuceba and Sciubidlo[36] addressed the CO_2 adsorption by densified MIL-53. For this purpose, they applied different compression pressures on the MOF powder. It was shown that MIL-53 pellets could be used as an adsorptive bed for CO_2 removal; however, their XRD patterns (Fig. 3 in the original article) suggest major amorphization of the MIL-53 framework upon pelletization at 29.6 kN m^{-2}. MIL-53 is famous for its ''breathing behavior'', owing to its flexible structure. Interestingly, a structural transition from large pores (MIL-53-lp) to narrow pores (MIL-53-np) was observed in the compression range from 3.7 to 7.4 kN m^{-2}.

The impact of compression on the textural and crystalline properties of MIL-53, as well as on its CO_2 sorption properties, was also studied by Ribeiro et al.[37] They compressed MIL-53 at 62 and 125 MPa with no binder added. The crystallinity was preserved even upon densification at 125 MPa as the XRD patterns were identical to their original powder counterpart. There is, however, a small shift of the reflections towards larger 2θ values. The authors attributed this phenomenon to the structural deformations of the framework upon compression, in accordance with the results provided by Majchrzak-Kuceba and Sciubidlo.[36] In addition, it was shown that the textural properties were altered accordingly. Thus, MIL-53 lost 46 and 32% of the available surface as well as 36 and 24% of the pore volume, which can be partly attributed to the transition from a system of large pores to narrow pores, upon densification at 125 and 62 MPa, respectively. Interestingly, a broad distribution of macropores at around 230 nm was observed. Furthermore, the CO_2 adsorption capacity of MIL-53 decreased from 5.2 mol kg^{-1} to 3.7 and 4.0 mol kg^{-1} when compressed at 1.5, 62, and 125 MPa, respectively. The reduced gas uptake is thus consistent with the decrease in pore volume. Therefore, pelletization is considered as an appropriate shaping method for this MOF.

ZIF-8

Ribeiro et al.[37] also extended their study to ZIF-8. As in the case of MIL-53, the ZIF-8 crystallinity was preserved even upon densification at 125 MPa as the XRD patterns matched with the original powder counterpart. In addition, it was shown that its textural properties were altered accordingly. Thus, ZIF-8 experienced only 7 and 12% loss in BET surface area as well as in pore volume when compressed at 62 and 125 MPa, respectively. Interestingly, it was demonstrated that densification led to the creation of macropores with diameters of about 300 nm and a distribution narrower than in the case of MIL-53. Furthermore, the CO_2 adsorption capacity decreased with the pore volume, from 9.0 mol kg^{-1} with the initial powder, to 8.7 (−3%)

Table 4 Textural and mechanical properties of ZIF-8 pellets compressed with 10 wt% SB and different solvents (10 wt%): NA – nitric acid, CA – citric acid, TA – trichloroacetic acid[40]

Pellet	S_{BET}, m^2 g^{-1}	Mechanical strength, MPa	Gas adsorption capacities at 25 °C, mg g^{-1}			
			CO_2	CH_4	C_3H_8	C_3H_6
ZIF-8	1023	0.19 (=)	340	100	183	210
ZIF-8/SB/NA	959	1.71 (+811%)	270	81	158	170
ZIF-8/SB/CA	933	1.59 (+748%)	280	84	172	190
ZIF-8/SB/TA	1161	0.75 (+300%)	310	92	175	195

and 8.5 mol kg^{-1} (−6%) with pellets pressed at 62 and 125 MPa, respectively.

Chapman et al.[38] studied ZIF-8 compression at industrially relevant pressures up to 1000 MPa. They reported an irreversible structural transformation (amorphization) at pressures higher than 340 MPa. This sets an upper limit for ZIF-8 compression. Interestingly, the authors observed that upon amorphization the ZIF-8 framework remained porous, however with modified sorption behavior. Thus, upon compressing at 300 MPa ZIF-8 lost ∼13% of its initial available surface area.

Among other studies on ZIF-8 densification, there is a study by Bazer-Bachi et al.[39] (who also densified SIM-1). The authors applied a wide range of pressures and showed that the crystallinity of ZIF-8 was preserved upon compression up to ∼230 MPa. At the same time, the loss in BET surface area was about 11%, with the ZIF-8 pellet reaching 1278 m^2 g^{-1}, while the pristine ZIF-8 powder exhibited 1433 m^2 g^{-1}. Noteworthily, these results are in good agreement with the ones reported by Ribeiro et al.[37] and Chapman et al.[38] Upon compression, SIM-1 demonstrated a similar trend with a 28% drop in surface area (516 vs. 370 m^2 g^{-1}) at a decent pressure of ∼400 MPa while preserving its framework topology according to its XRD pattern.

The study by Zhu et al.[40] concerned the effect of the type of binder on the textural and adsorption properties of ZIF-8 upon compression. More precisely, addition of 10 wt% SB (high quality pseudoboehmite) or talc powder led to a slightly reduced BET surface area as compared to the pristine ZIF-8 powder. In contrast, addition of 10 wt% bentonite or methylcellulose led to a more severe decrease in surface area. Besides, the authors studied the influence of acidic solvents on the final properties of the compressed pellets. Thus, mixing the initial ZIF-8/binder blend with 10 wt% citric acid led to a larger decrease in surface area as compared to other probed solvents such as nitric and trichloroacetic acid. Out of the three acids, nitric acid demonstrated the best compromise between high mechanical strength provided to the shaped pellets and high S_{BET} (Table 4).

As is evident from Table 4, although the textural and adsorption properties of the pellets were lower when ZIF-8 was compressed in the presence of an acid, the resulting objects exhibited superior mechanical properties. This might be attributed to the acidic strength of the solvents and therefore their ability to stick individual MOF and SB particles. Indeed, nitric acid is the strongest among the three and hence provided better peptization of SB particles. Besides, the authors found

that the adsorption capacities of the pellets were not altered as the loss upon shaping is consistent with the amount of the binder added.

MIL-101(Cr)

Densification of Cr-based MIL-101 for hydrogen adsorption was extensively studied by Ardelean et al.[41] The parent MOF powder was compressed into pellets with controlled bulk density up to a maximum value of 1.34 g cm^{-3}. The authors found that the MIL-101 crystal structure was preserved at intermediate pellet bulk densities of up to 0.47 g cm^{-3}, while the XRD pattern indicated transformation into an amorphous phase when compressed at 1.34 g cm^{-3}. The specific surface area decreased accordingly, down to 2602 m^2 g^{-1} for the pellets with a bulk density of 0.47 g cm^{-3} as compared to 3623 m^2 g^{-1} for the MIL-101 powder. Nevertheless, when the total volumetric hydrogen capacity was assessed, pellets with densities in the range of 0.45–0.47 g cm^{-3} exhibited 40 g L^{-1} H_2 uptake at −196 °C and 8 MPa. This value is in a good agreement with the previously reported values for MOF-177[32] and MOF-5.[28] Following this, Oh et al.[42] focused on setting an upper limit of H_2 uptake capacity for MIL-101 pellets which was found to be 42.3 g L^{-1} at −253 °C. In further studies, Blanita et al.[43] studied the H_2 adsorption capacity of close-packed hexagonal MIL-101 pellets (Fig. 2d). The total volumetric H_2 uptake reached comparable 40.3 g L^{-1} at −196 °C and 10 MPa for the pellets with a bulk density of 0.47 g cm^{-3}. At 15 MPa, the capacity further increased to 43.7 g L^{-1}. Finally, the authors studied the effect of Al tape addition in order to increase the thermal conductivity between MIL-101 pellets and therefore to improve the kinetics of H_2 adsorption/desorption cycles.[44] Indeed, 8–9 wt% Al tapes led to an increase of the thermal conductivity, up to ∼0.5 W m^{-1} K^{-1}, similar to the values reported by Purewall et al.[29] In turn, such MOF composites presented enhanced H_2 adsorption/desorption rates, allowing ∼0.9 fractional uptake/release in around 40 s.

MOF-74(Ni), (Mg)

This family of MOFs is also known as CPO-27. Tagliabue et al.[45] studied the effect of compression on the textural and adsorption properties of Ni-based CPO-27. They found that the MOF preserved its crystal structure when compressed at 100 MPa, while it collapsed at 1000 MPa. This was supported by N_2 physisorption measurements which confirmed the microporous nature of the former pellet with a BET surface area of 1050 m^2 g^{-1} – as compared to 1060 m^2 g^{-1} for the pristine CPO-27 powder. At the same time, the pellet compressed at 1000 MPa showed negligible BET surface area. Besides, it was demonstrated that the CH_4 adsorption on the shaped MOF was 129 N cm^3 g^{-1} at 30 °C and 3.4 MPa, as opposed to 157 N cm^3 g^{-1} for the parent powder MOF, indicating an 18% loss in gravimetric capacity upon compression.

Remy et al.[46] studied the adsorption properties of another MOF with the CPO-27/MOF-74 topology (Mg-MOF-74) upon pelletization. First, they found that addition of a few drops of methanol into the parent powder preserved the MOF crystal

structure upon pressing at 30 MPa for 1 minute. The thus-shaped pellets demonstrated a BET surface area of 1034 m^2 g^{-1}, lower than that of the parent powder (1249 m^2 g^{-1}). However, the pellets exhibited a similar CO_2 adsorption capacity at 0.05 MPa and 30 °C to the parent Mg-MOF-74 powder, i.e. 7.3 and 7.8 mmol g^{-1}, respectively. Moreover, they show strong affinity for CO_2 and therefore successfully separated CO_2 from an equimolar CO_2/CH_4 mixture. Interestingly, they found that Mg-MOF-74 pellets outperformed zeolite 13X, a benchmark adsorbent, for the CO_2 adsorption at 0.1 MPa and 35 °C on a gravimetric basis (6.9 vs. 4.8 mmol g^{-1}). However, the latter performed better on a volumetric basis (6.9 vs. 6.0 kmol m^{-3}). Nevertheless, the MOF pellets showed an easier regeneration than the zeolite. Importantly, the authors outlined the lower stability of Mg-MOF-74 pellets against impurities such as O_2 and H_2O over a series of runs as compared to zeolite 13X, making the latter the preferred adsorbent for low-pressure CO_2 separation.

HKUST-1

Alcañiz-Monge et al.[25] conducted a study on the pelletization of Cu-based HKUST-1 powder, presenting an initial S_{BET} of 1145 m^2 g^{-1}. However, when compressed at 180 MPa, the resulting HKUST-1 pellets exhibited a halved SSA, i.e. 470 m^2 g^{-1}. A further increase of the pressure up to 420 MPa had no further significant impact on SSA (420 m^2 g^{-1}). Consequently, the XRD patterns recorded for this MOF yielded no reflections, implying structural disorder. Considering these observations, this enables setting up an upper limit for compression force for HKUST-1 at 180 MPa. Above this value, the framework experiences structural collapse.

Peterson et al.[47] performed another study on HKUST-1 to examine the evolution of its physical and chemical properties. Thus, the authors applied pressures of 1000 psi ($\sim$7 MPa) and 10 000 psi ($\sim$69 MPa). While the crystal structure was globally preserved, compressed HKUST-1 exhibited broader reflections as well as high signal-to-noise ratios on the XRD patterns. This suggests partial framework damage. Consequently, there was a certain decrease in BET surface area, from 1698 m^2 g^{-1} for the powder to 892 m^2 g^{-1} for the pellets made at $\sim$69 MPa. These values are somewhat different from the ones reported by Kim et al.,[48] who stated that above 10 MPa the HKUST-1 framework underwent structural degradation. At the same time, Dhainaut et al.[49] reported a low (15%) loss in BET surface area for HKUST-1, reaching 1091 m^2 g^{-1} upon densification at 121 MPa. Besides, they showed that addition of 2 wt% of a binder (graphite) slightly improved the mechanical stability of HKUST-1 pellets without significant loss of BET surface area. They explained this relatively small loss as due to the presence of the remaining solvent within the framework, acting as a scaffold during compression, as well as the slow compression speed applied to the powder bed.

Interestingly, in a study by Peterson et al.[47] the N_2 physisorption isotherms exhibit a hysteresis, suggesting the creation of mesopores upon pelletization due to the breakage of framework bonds. Besides, when measuring NH_3 breakthrough curves, they demonstrated that ammonia eluted faster through the pelletized HKUST-1 as compared to the pure powder owing to its faster diffusion through the mesopores. Importantly, the total NH_3 loading remained intact around 7.2 mmol g^{-1} for all materials, indicating that the sorption sites in HKUST-1 remain available upon compression up to 69 MPa.

Bazer-Bachi et al.[39] also addressed the impact of pressure applied on HKUST-1. Consequently, it was clearly more affected by compression than two other MOFs tested (ZIF-8 and SIM-1). Indeed, already at an applied pressure of $\sim$24 MPa, HKUST-1 lost around 27% of its initial available surface area (1897 vs. 1377 m^2 g^{-1}). Moreover, at a higher pressure of $\sim$400 MPa, the surface area further decreased by 76%, accounting for 453 m^2 g^{-1}, while its XRD pattern displayed broad reflections with poor intensities, suggesting partial collapse of the framework.

Terracina et al.[50] outlined the crucial role of thermal activation in pelletization of HKUST-1. They found that the structural integrity and textural properties could be preserved to a great extent upon activation of the powder right before tableting and reactivation at 147 °C for 1 h immediately after compression. By doing so, the authors demonstrated that the damaging effect of coordinated water molecules could be decreased, as suggested by EPR measurements. Besides, the resulting pellets presented a higher BET surface area of 1935 m^2 g^{-1} as compared to 1620 m^2 g^{-1} for the as-made powder. The higher BET surface area could be due to the creation of additional mesopores, as underlined by Peterson et al.[47] Within the range of applied pressures, the authors found that 40 MPa is an optimal value to compress HKUST-1 into pellets with a good compaction degree.

UiO-66 family

Peterson et al.[51] performed a study on the compression of Zr-based UiO-66-NH_2. They applied a range of pressures from 5000 to 100 000 psi ($\sim$35 to 690 MPa) and observed only minor changes in textural properties upon compressing the powder up to 25 000 psi ($\sim$172 MPa). At this value, they found that both the crystallinity and structural integrity remained intact. At the same time, the BET surface area decreased from 1182 to 876 m^2 g^{-1}. Besides, upon compression the UiO-66-NH_2 pellets mostly retained their efficiency for toxic gas removal (Table 5). Noteworthily, compressed pellets exhibited shorter breakthrough times than their powder analogues especially in the case of NH_3, suggesting diffusion limitations or lower adsorption capacity. The latter is in line with the lower SSA measured.

Under the same conditions, the UiO-66 framework proved to be more stable toward high pressures.[47] Upon compression up

Table 5 NH_3 and CNCl adsorption capacities of UiO-66-NH_2 in both powder and pellet forms[51]

Adsorbent	Applied pressure, MPa	BET surface area, m^2 g^{-1}	Gas loadings under dry (humid) conditions, mol kg^{-1}	
			NH_3	CNCl
UiO-66-NH_2-powder	—	1182	3.3 (2.9)	4.1 (1.2)
UiO-66-NH_2-pellet	172	876	2.2 (1.8)	2.7 (0.9)

to 69 MPa, the BET surface area of the pellet reached 1080 m^2 g^{-1}, which is identical to that of the parent powder. Therefore, when tested for octane adsorption, the UiO-66 pellet compressed at $\sim$69 MPa demonstrated a saturation loading comparable to its powder counterpart (2.1 vs. 2.5 mmol g^{-1}, respectively).

Moreira et al.[52] demonstrated the reverse selectivity of UiO-66 towards liquid-phase separation of xylene isomers. Indeed, the obtained results suggested o-xylene selectivities of 1.8 and 2.4 with respect to m- and p-xylene, at 40 °C with n-heptane as the eluent. Besides, the authors showed that the selectivities were retained upon compression, meaning that no major modification of the pore network took place upon compression. Interestingly, the authors stated that at low concentrations the selectivity values of UiO-66 were comparable to the ones previously reported for MIL-53. However, the latter failed to separate m- and p-isomers unlike UiO-66.

Dhainaut et al.[49] reported a detailed study of the effect of compression on the textural properties of some of the most studied MOFs including UiO-66, UiO-66-NH$_2$ and UiO-67. They found that the impact of pressing UiO-66 and UiO-66-NH$_2$ was in line with the pressure applied as their textural properties decreased accordingly. Thus, they reported a 26% decrease in UiO-66-NH$_2$ BET surface area upon compression at 164 MPa, which is in good agreement with the results reported by Peterson et al.[51] Interestingly, it was found that the UiO-67 structure started collapsing upon compression above 63 MPa, while at 82 MPa it lost $\sim$80% of its initial surface area (2034 vs. 397 m^2 g^{-1}). Based on their results, they proposed to limit the compression to a final bulk density that represents at most 80% of the crystal density of the related MOF.

Bambalaza et al.[53] showed the possibility to press UiO-66 at even higher pressures to improve its volumetric H$_2$ uptake. They applied a wide range of pressures: 150, 290, 440, 590 and 665 MPa to study how the textural and structural properties would be modified. Consequently, they found that even at the highest compression pressure, 665 MPa, the framework retained its crystal structure. Besides, its BET surface area only decreased by $\sim$5% from 1737 m^2 g^{-1} for the powder to 1707 m^2 g^{-1} for the pellet. However, the loss of total pore volume was more significant and reached 16% (from 0.96 to 0.81 cm^3 g^{-1}). Importantly, the thus-formed pellets demonstrated a remarkable increase of volumetric H$_2$ uptake, from 29 to 74 g L^{-1} at −196 °C and 10 MPa as well as from 6 to 13 g L^{-1} when measured at 25 °C and 10 MPa. These results suggested a positive effect of compression on the packing density of UiO-66 (1.45 g cm^{-3} at 665 MPa) and therefore its benefits for improved volumetric H$_2$ uptake without a significant reduction of the gravimetric H$_2$ uptake.

Edubilli and Gumma[54] studied UiO-66 pelletization with addition of a PVA aqueous solution, aiming at a binder content of 9.3 wt% in the final dried pellets. They showed that this composition was optimal to provide enough mechanical strength to withstand a drop test. However, the presence of PVA caused slight pore blocking and it resulted in a decreased BET surface area, from 1378 m^2 g^{-1} to 1195 m^2 g^{-1} (−14%).

Consequently, when probed for CO$_2$ and N$_2$ adsorption, the volumetric uptake decreased by 14–18% for both gases: from 1.87 to 1.62 mmol cm^{-3} for CO$_2$ and from 0.27 to 0.23 mmol cm^{-3} for N$_2$ at 25 °C and 1 MPa. Besides, they showed the capability of UiO-66 to separate CO$_2$ over N$_2$ with a factor of 6.

Khabzina et al.[55] studied UiO-66-COOH and its performance for NH$_3$ removal before and after shaping, using different techniques including extrusion, granulation and pelletization. When compressed at 9.7 MPa, the MOF exhibited a 14% loss in BET surface area − 614 m^2 g^{-1} as opposed to 710 m^2 g^{-1} for the original powder. Importantly, such pellets outperformed the commercial NH$_3$ adsorbents based on activated carbon (AC-3M and AC-Norit RZN$_1$) in terms of both the total amount of adsorbed NH$_3$ and the breakthrough time over a wide range of relative humidities (see Table 10 for detailed data).

MIL-100 family

Yang et al.[56] addressed in their study the effect of the activation temperature on the adsorption properties of Cr-based MIL-100 in both powder and granular forms. The latter were prepared upon crushing and sieving compressed pellets (Fig. 2e and f). They found that activation at 300 °C under vacuum for 12 h led to partial collapse of the framework, as deduced from broader reflections with decreased intensities. Indeed, they proposed 250 °C as the optimal temperature for the MOF activation. Besides, it was demonstrated that at 1 bar and 25 °C the thus-activated MIL-100 powder adsorbed 5.8 mmol g^{-1} CO$_2$ – the highest reported value under the same conditions. This shows the crucial role of thermal activation in releasing the open Cr^{n+} sites which are responsible for the adsorption of CO$_2$ molecules. In addition, the authors showed that once activated at 250 °C the MIL-100 pellets experienced a considerable loss in CO$_2$ uptake, from 5.8 to 4.05 mmol g^{-1}, suggesting poorer accessibility of open Cr^{n+} sites upon densification. Interestingly, by screening other gases the authors concluded that densification affected less the adsorption of CH$_4$ and N$_2$ over MIL-100 pellets as compared to CO$_2$.

Valekar et al.[57] compared the NH$_3$ adsorption capacities of Fe-based MIL-100 pellets with granules made via wet granulation. The results suggested a partial loss of long order arrangement of the framework as well as a considerable loss in BET surface area, from 2088 m^2 g^{-1} for the powder to 1300 m^2 g^{-1} for the compressed pellet. The same detrimental effect of pelletization was observed for Cr-based MIL-101. Fe-MIL-100 pellets showed an NH$_3$ uptake of 3.6 mmol g^{-1}, however, less than that of the MIL-100 granules (4.4 mmol g^{-1}), also with a shorter breakthrough time.

MOF-801

Taddei et al.[58] studied the influence of compression on the textural and adsorption properties of Zr-based MOF-801. They applied four different pressures (146, 292, 438 and 584 MPa) and found that the reflections in the XRD patterns became broader and less intense as the compression pressure increased, implying partial collapse of the framework.

Fig. 3 BET SSA as a function of applied pressure during pelletization (left): (▲) – ZIF-8 by Ribeiro et al.,[37] (▲) – ZIF-8 by Bazer-Buchi et al.,[39] (●) – UiO-66-NH$_2$ by Peterson et al.,[51] (●) – UiO-66-NH$_2$ by Dhainaut et al.,[49] (■) – HKUST-1 by Bazer-Buchi et al.,[39] (■) – HKUST-1 by Dhainaut et al.,[49] and (■) – HKUST-1 by Alcañiz-Monge et al.[25] BET surface area as a function of bulk density (right): (+) – MOF-177 by Zacharia et al.,[32] (✗) – MIL-101 by Ardelean et al.,[41] and (◆) – MOF-5 by Purewall et al.[28]

Interestingly, the compression time was shown to have no effect on the final crystallinity nor the mechanical resistance, assessed by repetitively dropping the pellets from a 36 cm height until they showed considerable damage. Therefore, the shortest time of 15 s was preferred. Besides, the addition of 5 wt% PVB as a binder had a positive effect on the mechanical properties, with higher resistance upon the drop test. The BET surface area of the pristine MOF powder, 899 m^2 g^{-1}, decreased significantly upon compression. There was, however, no significant difference between the pellets compressed at 146, 292 and 438 MPa with 5 wt% PVB as they exhibited BET surface areas of 569 (−37%), 546 (−39%) and 605 m^2 g^{-1} (−33%), respectively. The pellets pressed with 5 wt% PVB under 146 MPa for 15 seconds were further tested, and they retained 86% of the powder's CO$_2$ gravimetric uptake as well as 74% of the powder's working capacity towards H$_2$O adsorption.

To sum up, pelletization is a relatively easy and fast shaping technique which only requires a manual press. Depending on the targeted application, it can be performed with or without a binder. The former case enhances the mechanical stability of the final pellets, yet at the expense of a lower accessible surface area. The structural and textural integrity upon pelletization depends on the applied pressure and the nature of the MOF itself. Thus, several MOFs such as UiO-66-NH$_2$ and ZIF-8 can undergo compression at high pressures, with relatively preserved intrinsic structural properties and minor losses in textural properties. For these MOFs, the loss in BET surface area as a function of applied pressure mostly presents a linear behavior (Fig. 3, left). This implies that for these MOF families pelletization can be considered as an appropriate way of shaping. At the same time, HKUST-1 has a more unpredictable trend, meaning that the textural properties of the final pellets depend as well on the shaping conditions (presence of moisture or linker in excess). Thus, special care should be given to the

preparation of HKUST-1 pellets. Generally, pelletization leads to an increase of the bulk density, thus increasing the volumetric adsorption capacities – a crucial characteristic for gas adsorption applications. Once again, certain MOFs such as MOF-5, MOF-177 and MIL-101 demonstrate a linear trend of their bulk density as a function of BET surface area (Fig. 3, right). This highlights the growing potential of these particular MOFs in H$_2$ storage.

Granulation

Granulation is a commonly-used shaping process which is based on the size enlargement of a parent powder material into an assembly of bigger agglomerates. A typical body shaped *via* granulation is referred to as a "granule" with an average size range of 2–20 mm.[59] Many productions such as the pharmaceutical and food industries rely on the utilization of such granules for processing and storage purposes. Notably, granulation is of great importance for the chemical industry as it allows shaping materials (adsorbents, catalysts) into granules which are subsequently used in fixed-bed reactors. This minimizes the risk of pressure drops during large-scale industrial productions, and ensure homogeneous diffusion.[59]

It should be noted that there are two types of granulation processes distinguished in the literature: wet and dry granulation. Dry granulation is applied when powders are incompatible with the use of solvents. Typically, it implies the compression of a parent powder at high pressures followed by mild crushing and sieving. Mainly, this process resembles and is typically subsequent to pelletization. Therefore, it was described in the previous part.

As the name suggests, wet granulation implies first wetting the initial powder. For this purpose, the powder is loaded in a high shear-rate mixer (Fig. 4a) and a volatile solvent

Fig. 4 Typical wet granulation equipment: a high shear–rate mixer (Maschinenfabrik Gustav Eirich GmbH & Co KG), also referred to as a granulating pan (a) with an adjustable speed and direction of rotation; and a disc pelletizer (ERWEKA GmbH) also referred to as a rolling machine (b) with a controllable speed and inclination angle. Schematic representation of the wet granulation process: (c) mixing; (d) wetting and nucleation; (e) growth; and (f) spherization by attrition and breakage.

(*i.e.* short-chain hydrocarbons or water) is added in portions – generally by spraying for homogeneity. This step is usually fast – a few tens of seconds to minutes – and causes wetting and cohesion of individual particles into primary agglomerates.

Once formed, the agglomerates are further transferred into a rolling machine (Fig. 4b), which finalizes the process by inducing continuous attrition between individual agglomerates over hours, thus facilitating and enhancing their spherical shape. Finally, the beads are dried, thus leading to pure granules of the parent material. The overall wet granulation process is presented in Fig. 4c–f.

However, upon solvent removal, the agglomeration of particles into spherical beads is only ensured by cohesion forces. Owing to their limited strength, the as-produced spheres may not have sufficient mechanical strength to maintain their shape and therefore be used for a targeted application. In this case,

the reinforcement of the shaped granules by addition of binders is of particular interest. There are many types of binders known and used nowadays. Generally, they can be classified into inorganic binders such as clays,[60] silica,[61] and alumina[62] and organic binders such as polyalcohols[63] and carbohydrates.[64] As for the former, not only do they improve the mechanical stability but they also contribute to the physical and chemical properties of the parent powder being shaped. Thus, upon shaping of zeolites with clays as binders there is an evolution of the physicochemical and thus catalytic properties of the initial zeolite.[65] In the same fashion, alumina contributes to the acidic properties of zeolites.[66] On the other hand, organic binders tend to improve the mechanical stability. Besides, they might be easily removed from the shaped composites upon thermal treatment, thus not altering the physical and chemical properties of the initial parent powder.

Table 6 List of MOFs shaped *via* wet granulation

MOF	Metal/ligand	Binder, wt%	D_{gr}, mm	S_{BET}, m^2 g^{-1} Powder	Granules	Ref.
Inorganic binders						
MIL-100	Fe/BTC	Silica sol, 10	1.18–1.7	1772	1619 (−9%)	68
MIL-100	Fe/BTC	Silica, 10	1.0–3.0	—	1568	69
MIL-100	Fe/BTC	MRA, 5	2.0–2.5	2088	1831 (−12%)	57
MIL-100	Fe/BTC	MRA, 5	2.0–2.5	1928	1451 (−25%)	70
MIL-101	Cr/BDC	MRA, 5	2.0–2.5	4066	3685 (−9%)	57
MIL-127	Fe/TazBz	MRA, 5	2.0–2.5	1413	1266 (−10%)	70
MIL-160	Al/FDC	Silica sol, 10	0.5–1.8	1150	1000 (−13%)	67
UiO-66	Zr/BDC	MRA, 5	2.0–2.5	1050	911 (−13%)	57
UiO-66	Zr/BDC	MRA, 5	2.0–2.5	903	619 (−31%)	70
UiO-66-NH$_2$	Zr/2-aminoBDC	MRA, 5	2.0–2.5	875	823 (−6%)	57
Organic binders						
ZIF-8	Zn/MIM	HPC, 5	0.1–0.4	—	—	72
CPO-27	Ni/2,5-(OH)$_2$BDC	PVA, 2	0.3–1.0	937	1319	74
HKUST-1	Cu/BTC	PVA, 2	0.3–1.0	1605	147 (−91%)	74
UiO-66	Zr/BDC	Sucrose, 10	0.5–15.0	1367	674 (−51%)	73
UiO-66	Zr/BDC	PVA/PVB, 3	1.3–1.7	1065	1017 (−5%)	71
UiO-66-NH$_2$	Zr/2-aminoBDC	PVA/PVB, 3	1.3–1.7	958	795 (−17%)	71
MIL-100	Fe/BTC	PVA, 2	0.3–1.0	1212	1172 (−3%)	74
MIL-100	Fe/BTC	PVA/PVB, 3	1.3–1.7	2261	2043 (−10%)	71
MIL-125-NH$_2$	Ti/2-aminoBDC	PVA/PVB, 3	4.0	—	—	75
MIL-127	Fe/TazBz	PVA/PVB, 3	1.3–1.7	1181	1117 (−5%)	71
Binderless granulation						
UiO-66-NH$_2$	Zr/2-aminoBDC	None	0.5–1.4	756	747 (−1%)	76

Ligand codes: BTC – benzene-1,3,5-tricarboxylic acid; BDC – benzene-1,4-dicarboxylic acid; FDC – 2,5-furandicarboxylic acid; TazBz – 3,3′,5,5′-azobenzenetetracarboxylate; and MIM – 2-methyl imidazole. Binder codes: PVA – polyvinyl alcohol; PVB – polyvinyl butyral; MRA – mesoporous ρ-alumina; and HPC – hydroxypropyl cellulose. "—" not specified.

For MOFs, the primary goal of using binders is to enhance the mechanical stability of the granules. For this purpose, compounds capable of creating decently strong bonds with the surfaces of MOFs are preferred as binders. As an example, this implies cohesion of MOF particles *via* hydrogen bonding, and therefore, compounds possessing multiple functional groups (mainly –OH) are beneficial. This includes alcohols (polyvinyl), sugars (sucrose, cellulose), esters (hydroxypropyl cellulose) and others. However, upon shaping they cannot be removed due to the limited thermal stability of MOFs.

It is worth mentioning that the overall properties of the shaped granules depend both on the features of the parent MOF powder and on the properties of the binder. Therefore, the choice of the latter is highly important as well as its total content in the final composition. Indeed, granulation of MOFs should yield compact and stable spheres with a minimum loss of their intrinsic properties including their specific surface area and pore volume. Therefore, the main objective of granulation is to find a balance between providing sufficient mechanical stability and preserving the initial textural properties of MOFs. The up-to-date list of thus-shaped MOFs is given in Table 6.

Inorganic binders

Silica

The effect of binders on the textural properties of shaped granules is evidenced in Table 6. Indeed, there is a certain decrease of S_{BET} for all the studied MOFs; however, once shaped into granules, these MOFs are better fitted for a targeted application. Thus, in 2017 Permyakova et al.[67] studied the heat-storage properties of a series of MOFs including MIL-127(Fe), MIL-125(Ti)-NH$_2$, MIL-100(Fe) and MIL-160(Al). The latter demonstrated one of the highest cycling loading lifts (the amount of water exchanged between adsorption and desorption steps) and therefore high energy storage capacity (the amount of energy stored per unit of mass of a material). Besides, the structural integrity of MIL-160 was preserved upon 10 adsorption/desorption cycles as compared to the other studied MOFs. Therefore, the authors further examined the performances of MIL-160 granules in a pilot-scale reactor. For a typical shaping *via* the wet granulation process, a predefined amount of MIL-160 powder was subjected to mixing with 10 wt% silica sol as a binder and subsequently granulation was finalized in a rolling machine to enhance the spherical shape. Eventually, the granules were dried at 100 °C for 12 h to remove the residual water and yield spherical objects of 0.5–1.8 mm (Fig. 5a).

The thus-shaped spheres were fully characterized, and according to their matching XRD patterns with the pristine powder, the crystal structure of the MIL-160 granules was assumed to be preserved. The morphology of the crystals was also preserved according to SEM images, with a secondary phase observed on the MOF surface attributed to the silica particles. Indeed, their presence was further proven by the

Fig. 5 Photographs of: MIL-160 granules (a) prepared by Permyakova et al.[67] Copyright 2017 Wiley. MIL-100 granules (b) prepared by Martins et al.[69] Copyright 2020 American Chemical Society. MIL-100 (c), MIL-101 (d), UiO-66 (e), and UiO-66-NH$_2$ (f) containing 5 wt% MRA binder prepared by Valekar et al.[57] Copyright 2017 The Royal Society of Chemistry. UiO-66 granules (g) prepared by Ren et al.[73] Copyright 2015 Elsevier. MIL-100, MIL-127, UiO-66, and UiO-66-NH$_2$ granules (h, from left to right in big vessels) with their corresponding powders in small vessels prepared by Chanut et al.[71] Copyright 2016 Wiley.

means of IR spectroscopy as an additional band observed in the spectrum of MIL-160 granules at 1120 cm^{-1}, corresponding to O–Si–O asymmetric stretching. Importantly, N$_2$ physisorption measurements revealed a loss in S_{BET} upon granulation, from 1150 to 1000 m^2 g^{-1} for the parent MIL-160 powder and the corresponding granules, respectively. The same trend was observed for the total pore volume: 0.479 cm^3 g^{-1} (powder) and 0.443 cm^3 g^{-1} (granules). As the loss in specific surface area and pore volume (−13%) slightly exceeded the binder content (10%), partial pore blocking might occur. Nevertheless, the performance of the MOF MIL-160 towards cycling loading lifts was maintained, reaching 0.36 and 0.32 g g^{-1} (−11%), respectively, for the MIL-160 powder and granules measured between 30 °C (adsorption) and 80 °C (desorption) at 1.25 kPa. For the granules, this corresponded to an energy sorption capacity of 305 W h kg^{-1}. This high value was obtained under relatively mild desorption conditions, making MIL-160 an excellent candidate for heat-storage applications.

The same binder was applied for the wet granulation of Fe-based MIL-100 by Kim et al.[68] For a typical shaping procedure, they mixed 700 g of pre-synthesized MIL-100 with 10 wt% silica sol in a mixing granulator. Then, the primary agglomerates were transferred to a spheronizer to enhance the spherical shape. The thus-formed granules were dried at 110 °C for 12 h to remove any residual moisture. Eventually, this process yielded spherical granules with a size distribution of 1.18–1.70 mm. These granules exhibited a similar XRD pattern to the original powder, suggesting that the shaping process had no impact on the crystal structure. In accordance with this, the spheres preserved most of the textural properties of the parent MOF powder, presenting specific surface areas of 1619 and 1772 m^2 g^{-1} and total pore volumes of 0.82 and 0.93 cm^3 g^{-1}, respectively. The authors further applied the granules for the separation of SF$_6$, which is a greenhouse gas, from a N$_2$ stream. Noteworthily, the powder and granulated MIL-100 demonstrated nearly the same SF$_6$ adsorption capacity of 1.673 and 1.658 mmol g^{-1}, respectively. Thus, there was no considerable difference in the adsorption properties upon granulation. Interestingly, the adsorption capacity of the MIL-100 granules kept increasing with pressure, unlike the commercial adsorbent zeolite 13X. Indeed, the latter reached saturation at around 3 bar (with 2.5 mmol g^{-1} at 25 °C), while the former demonstrated gradually increasing gas uptake, reaching around 4 mmol g^{-1} at 3 bar and 25 °C. The authors attributed this phenomenon to the presence of mesopores in MIL-100, which contributed to the adsorption of SF$_6$ once micropores were filled. Furthermore, although the SF$_6$ breakthrough times were nearly identical for the MIL-100 granules and zeolite 13X granules at high pressure (9 bar), the desorption/regeneration of the former was considerably shorter (20 vs. 250 min) and complete, while the latter exhibited residual SF$_6$ after regeneration due to strong interactions.

The same approach was also applied to shape MIL-100 by Martins et al.[69] In a typical shaping procedure, the parent MIL-100 powder was mixed with 10 wt% silica as a binder in a rolling machine. During mixing, water and ethanol were periodically sprayed on the blend to facilitate the agglomeration of individual particles. Eventually, the granules were isolated and dried at 100 °C to remove the residual solvents. This procedure resulted in semi-spherical granules with an average size of 1.0–3.0 mm (Fig. 5b), presenting a micropore volume of 0.58 cm^3 g^{-1} and a specific surface area of 1568 m^2 g^{-1}, which is in agreement with Kim et al.[68] The beads were further applied to ethane/propane and ethylene/propane gas mixture separation. The results suggested preferential C$_3$H$_8$ adsorption over C$_2$H$_6$ and C$_2$H$_4$. This remained the case when the temperature was varied, highlighting the potential of the MIL-100 granules for C$_2$/C$_3$ separation following pressure-swing adsorption (PSA). Moreover, lab-scale vacuum-swing adsorption (VSA) experiments starting from a 0.30 ethane/0.70 propane mixture, at 50 °C and 150 kPa, were conducted. The MIL-100 granules yielded an ethane-rich stream with a purity of 99.5% and a recovery of 86.7%, as well as a propane-rich stream with a purity of 99.4% and a recovery of 97.0%. The same VSA experiment starting from a 0.30 ethylene/0.70 propane mixture resulted in an ethylene-rich stream with a purity of 100% and a recovery of 75.8%, as well as a propane-rich stream with a purity of 94.7% and a recovery of 100%. The obtained results show that MOFs such as MIL-100 adequately shaped are highly promising for industrial separation processes.

Mesoporous ρ-alumina (MRA)

Another class of inorganic binders was first probed by Valekar et al.[57] for granulating a series of MOFs. They produced granules of MIL-100, MIL-101, UiO-66 and UiO-66-NH$_2$ by mixing pre-defined amounts of MOF powders with 5–20 wt% mesoporous ρ-alumina (MRA) in a rolling machine. During mixing, the blend was sprayed with water to facilitate particle agglomeration. The thus-produced granules were further sieved and rounded in a rolling machine. Finally, spheres with sizes of 2.0–2.5 mm were isolated and dried at 110 °C for 12 h (Fig. 5c–f).

The structural properties of the shaped granules were preserved for all the studied MOFs upon granulation. Indeed, the XRD pattern of each granular MOF matched well with its powder counterpart. Besides, the same observation applies to the textural properties as N$_2$ physisorption measurements yielded similar isotherm shapes for MOF powders and granules, while the specific surface areas measured by the BET method suggested a consistent loss within the 1.0–7.7% range when shaped with 5 wt% MRA. Moreover, there was clear evidence of hierarchical meso- and macroporous structures confirmed by mercury porosimetry, due to the inter-particle voids generated upon granulation. Furthermore, the authors provided valuable information on the preservation of the MOFs' chemical properties after shaping. Indeed, NH$_3$-TPD and pyridine-FTIR measurements performed on MIL-100 revealed the presence of Lewis acid sites in the temperature range of 150–200 °C. They originated from unsaturated metal sites within the MOF structure, which were induced mainly upon thermal activation. The binder could partially block the accessibility to the acidic sites of the MOF; however, the

NH$_3$-TPD measurements suggested that these sites remained accessible upon granulation with no change in desorption peak positions. While the acidic strength remained equivalent, the loss in total acidic sites was consistent with the binder content (5, 10 or 20 wt%). The same phenomenon was observed upon pyridine-FTIR measurements. The bands corresponding to pyridine coordination with Fe^{3+} (1014 cm^{-1}) and Fe^{2+} (1005 cm^{-1}), responsible for the Lewis acidity in MIL-100, remained intact. Therefore, the authors demonstrated that granulation with the MRA binder had no effect on the acidic properties of MIL-100.

Interestingly, they also prepared MIL-100 pellets following the pelletization method and compared the thus formed bodies with the granules in terms of NH$_3$ adsorption. The latter exhibited higher adsorption capacity at 25 °C (4.4 vs. 3.6 mmol g^{-1}), suggesting that upon pelletization, the parent powder underwent more drastic structural and textural changes as compared to granulation. This was supported by XRD and N$_2$ physisorption measurements.

A further study on the gas sorption properties of MOF granules was done by Iacomi et al.[70] For this purpose, they followed the protocol proposed by Valekar et al.[57] to form UiO-66, MIL-100 and MIL-127 granules. The textural properties, as evaluated by N$_2$ physisorption measurements, revealed a drastic decrease in specific surface area upon granulation of −10, −25, and −31% for MIL-127, MIL-100 and UiO-66, respectively. At the same time, the total pore volume experienced a loss of −26, −23, and −36%, respectively. The obtained results were attributed to the possible structural degradation upon shaping. Indeed, the losses in textural properties were higher than the 5% reported in the previous study by Valekar et al.[57] and might be due to the higher shear forces applied during the mixing step. Nevertheless, adsorption experiments performed both on the UiO-66 powder and on its granular counterpart (Fig. 5h) suggested higher volumetric uptakes for the latter towards small adsorbates such as N$_2$, CH$_4$ and CO$_2$ as a result of densification upon granulation, as observed by Chanut et al.[71] However, larger adsorbates such as C$_3$H$_6$, C$_3$H$_8$ and C$_4$H$_{10}$ experienced a decreased volumetric uptake. The authors attributed this phenomenon to the pore blocking effect of the binder. Interestingly, upon adsorption of CO and C$_3$H$_6$ on MIL-127 and MIL-100, they reported higher adsorption enthalpies as compared to UiO-66. This indicates the presence of Fe^{2+} sites, generated upon thermal activation by partial reduction of Fe^{3+} sites. Indeed, Fe^{2+} sites induce stronger interactions with molecules with permanent dipole/quadrupole moments or π-electrons such as CO, CO$_2$ and C$_3$H$_6$.

Lastly, as a complementary study, Iacomi et al.[70] performed water and methanol vapor adsorption experiments to address the effect of binders on the surface properties of UiO-66, MIL-100 and MIL-127 MOFs. Generally, both H$_2$O and CH$_3$OH adsorption isotherms remained identical for all three MOFs upon shaping, suggesting that MRA showed no alteration of the hydrophilicity/hydrophobicity balance. Importantly, the slow initial water uptake on UiO-66 is consistent with a hydrophobic surface, while the opposite was observed for MIL-127, highlighting its hydrophilic surface; at the same time, MIL-100 presented intermediate surface hydrophilicity/hydrophobicity features.

Organic binders

Carbohydrate-based binders

Ohsaki et al.[72] showed the possibility to shape ZIF-8 powder in a mixing granulator using two different approaches: liquid or powder addition. The former implied mixing the ZIF-8 powder with a few consecutive portions of an aqueous solution of the binder hydroxypropyl cellulose and successive steps of mixing for 5 min. The powder addition approach, on the other hand, suggested initial mixing of ZIF-8 with the binder in its dry form (5 wt%) followed by the subsequent addition of portions of water (42 wt%) during mixing. Interestingly, the latter was found to be more suitable as it yields granules with an average size of >200 μm, while the liquid addition method resulted in a large percentage of non-granulated ZIF-8 particles. The authors attributed this phenomenon to a more uniform mixing of the MOF with the binder upon the powder addition method which was consequently chosen for the rest of the study, and this highlights the importance of mixing the powder and the binder prior to granulation. The XRD results suggested the preservation of the crystal structure upon granulation as evidenced from the matching patterns of the ZIF-8 powder and the granules. Furthermore, the granules retained a consequent specific surface area, around 90% of the original powder. Noteworthily, the effect of the binder content on the surface area was addressed in the study. Namely, upon increasing the binder percentage up to 20 wt% (at a constant amount of water of 42 wt%) the granules retained around 60% of the initial surface area. The decrease became more drastic at 30 wt% binder loading as the granules retained <10% of the starting surface area. This set the upper limit for the binder content at around 20 wt%. At the same time, the water content was shown to have a low impact on the surface area.

Another example of wet granulation with carbohydrates as binders was provided by Ren et al.,[73] who described the shaping of UiO-66 with sucrose. More precisely, they mixed 450 g of MOF with 50 g of sucrose in a centrifugal granulator followed by the spraying of water. The granules were further subjected to drying at 60 °C for 24 h. The entire procedure yielded spherical beads with an average size of 0.5–15 mm (Fig. 5g).

As confirmed by XRD, the crystal structure remained intact upon granulation. The presence of the binder was assumed as a secondary plate-like phase was observed in the SEM images. Consequently, there was an evident impact on the textural properties of the UiO-66 granules brought about by the binder. Namely, the specific surface area decreased to 674 m^2 g^{-1}, which represents 50% of the SSA of the parent powder. Accordingly, the total pore volume decreased from 0.56 to 0.34 cm^3 g^{-1}. In agreement with that, the hydrogen uptake similarly experienced a coherent decrease, from 1.54 cm^3 g^{-1} for the UiO-66 powder to 0.85 cm^3 g^{-1} obtained for the

granules. Importantly, the authors provided data on the mechanical stability of the granulated UiO-66 based on non-conventional drop tests. Thus, no breakage was observed when dropping the granules on a steel surface from 0.5 m height after 70 consecutive drops. Moreover, attrition tests revealed that only 5% of the initial granule weight ended up as "fines", after 60 min of tumbling at 25 rpm and further sieving. This suggested a considerable mechanical stability of the shaped granules.

PVA and PVB binders

Another class of binders largely used for wet granulation is polyalcohols, such as polyvinyl alcohol (PVA), and their derivatives, including polyvinyl butyral (PVB). The former was used in a study by Hindocha et al.[74] who formulated three MOFs (Cu-BTC (HKUST-1), CPO-27 and MIL-100) into spherical granules. The typical procedure implied pre-mixing 1 g of MOF powder with 2 wt% PVA followed by granulation upon addition of 0.25 mL of water. This formulation yielded spheres of 0.3–1.0 mm on average after sieving. As suggested by XRD results, this procedure had a considerable impact on the HKUST-1 framework, as the granules presented a pattern combining several mixed phases which were absent for the parent powder. In agreement with that, the shaped material showed a considerable decrease in specific surface area upon granulation, from 1605 to 147 $m^2\ g^{-1}$ for the parent powder and the granules, respectively. Consequently, this material, losing its MOF structure, was not able to retain a similar ammonia adsorption capacity, reaching only 19 $mg\ g^{-1}$, while the parent powder could adsorb up to 105 $mg\ g^{-1}$ under the same conditions (500 ppm ammonia, 40% RH). Thus, using water to shape HKUST-1 following wet granulation cannot be considered as an appropriate method.

On the other hand, the CPO-27 and MIL-100 frameworks proved to be more stable under the applied conditions, as the granules' diffractograms yielded matching patterns with their powder counterparts. The MIL-100 granules presented only a slight decrease in SSA (S_{BET} = 1172 $m^2\ g^{-1}$), which is in the range of 2% loss as compared to the parent powder (S_{BET} = 1212 $m^2\ g^{-1}$), consistent with the initial amount of the binder. Surprisingly, the CPO-27 granules exhibited a considerable increase in specific surface area (S_{BET} = 1319 $m^2\ g^{-1}$) as compared to S_{BET} = 937 $m^2\ g^{-1}$ of the as-synthesized CPO-27. This phenomenon was stated to be unclear by the authors.

Both granules exhibited an ammonia adsorption capacity of about 50 $mg\ g^{-1}$ and a corresponding breakthrough time of about 100 min ([NH_3] = 12.5 ppm, Table 7). For comparison, a commercial activated carbon presents an ammonia adsorption capacity of 8 $mg\ g^{-1}$ with a breakthrough time of 9 min. Interestingly, the authors performed attrition tests to probe the mechanical stability of the granules. Upon rolling in a mill for 18 h and subsequent sieving, the MIL-100 granules lost only 2% of their initial weight, while the CPO-27 granules were more affected (−18%). Notably, the granules presented a reduced size due to the long-term attrition (0.3–1.0 mm). For comparison, the authors also performed dry granulation (binderless pelletization then milling-sieving) which was beneficial in the case of CPO-27 as it resulted in a higher ammonia adsorption capacity (64 vs. 51 $mg\ g^{-1}$) as well as an extended breakthrough time (189 vs. 106 min). On the other hand, the "dry-shaped" MIL-100 granules presented similar performances to the "wet-shaped" granules. Therefore, the choice of either shaping process depends on the MOF itself and its targeted application.

A mixture of PVA and PVB was used as a binder in the study by Chanut et al.[71] The authors first mixed 5 g of MOF powder with a 3 wt% polymer blend, followed by periodical spraying of ethanol for a total of 50 mL to cause primary particle agglomeration. Upon sieving, a fraction with sizes between 1.3 and 1.7 mm (Fig. 5h) was rounded using a rolling device to achieve the final shape. Eventually, the spheres were dried at 110 °C for 12 h to remove the residual ethanol.

By analyzing the XRD patterns, a slight degradation of UiO-66-NH_2 and MIL-100 structures can be deduced from the decrease in the intensities of the principal reflections as compared to their powder counterparts. This was further supported by N_2 physisorption measurements which revealed a certain decrease of their textural properties due to a partial structural collapse. At the same time, the corresponding losses in specific surface area and micropore volume for the UiO-66 and MIL-127 granules are within 3%, which is in agreement with the binder content. In terms of adsorption properties, there is a general trend observed: after granulation, the gravimetric uptake decreased (less gas adsorbed per weight of granules than that per weight of powder), while the volumetric uptake increased (more gas adsorbed per volume of granules than that per volume of powder). This implies that the wet granulation process caused densification and therefore an increase in bulk density. The latter relates to the amount of adsorbent stackable in a reactor vessel and thus is an important factor when evaluating adsorption capacities for real-life applications.

Probing molecules with and without dipole/quadrupole moments such as CO, CO_2, and CH_4 on both powder and granular UiO-66 and UiO-66-NH_2 yielded similar adsorption profiles. This implies that granulation had no significant impact on the surface properties of the MOFs. Interestingly, the adsorption of larger butane molecules on MIL-100 granules revealed an "S" shape isotherm with a sharp increase at elevated pressures, while a Langmuir-type adsorption curve was observed with the powder. The authors attributed this phenomenon to high partial pressures required to displace the polymeric chains of PVA/PVB and open the pores for butane adsorption. Notably, using the MIL-127 powder, the enthalpy

Table 7 Adsorptive and mechanical properties of the MOF granules prepared by Hindocha et al.[74]

MOF	NH$_3$ adsorption capacity, mg g^{-1}	Breakthrough time, min under 12.5 ppm of NH$_3$	Weight loss upon attrition test, %
CPO-27	51	106	18
MIL-100	50	100	2
HKUST-1	19	43	11

profile of CO adsorption showed a total decrease along with a considerable drop at initial adsorption energies, while a linear behavior was obtained with MIL-127 granules. The authors attributed this phenomenon to the inaccessibility of Lewis acid sites after granulation of MIL-127. It possibly originated from the binder presence partially preventing Fe^{3+} reduction to Fe^{2+} during the thermal activation of MIL-127. However, as mentioned by the authors, more experiments are needed to further address this phenomenon.

A similar wet granulation methodology was applied by Regufe et al.[75] Namely, the same binder system (3 wt% PVA/PVB blend) was mixed with Ti-based MIL-125_NH$_2$ and further agglomerated in a pan-type granulation with the addition of an ethanolic solution. Ti-based MOF granules with an average size of 4.0 mm were further applied for gas adsorption and syngas purification. Adsorption measurements of numerous gases resulted in the following sequence of adsorption capacities: $CO_2 > CH_4 > N_2 > CO > H_2$ with 8.5, 7.1, 5.4, 3.5 and 0.3 mol kg^{-1}, respectively. The authors further conducted pressure-swing adsorption (PSA) experiments on these granules. Interestingly, the hydrogen purification from a CO/H$_2$ (30%/70%) mixture reached 100%. In a different experiment, starting from a mixture containing 30% CO_2, 22% CO and 48% H_2, a suitable CO/H$_2$ mixture for the Fischer–Tropsch process, with CO_2 impurity down to 3% was obtained.

Binderless granulation

So far, only one successful example of binderless MOF granules has been reported. Leloire et al. prepared UiO-66-NH$_2$ granules by the stepwise addition of a water/ethanol mixture in a high shear-rate mixer, followed by the use of a rolling machine to both reinforce their mechanical resistance and increase their sphericity.[76] After drying, well-rounded granules of 0.5 to 1.4 mm were obtained. Interestingly, their BET surface area was close to that of the powder (747 vs. 756 m^2 g^{-1}). Moreover, the authors observed by FT-IR spectroscopy the disappearance of a band at 1686 cm^{-1}, attributed to the complexation of unsaturated zirconium cations at the surfaces of the UiO-66-NH$_2$ crystallites with free carboxylic groups. Of note, the vibration band at 1660 cm^{-1}, typically attributed to the presence of residual DMF entrapped, decreased after granulation. Hence, partial extraction of DMF molecules during the shaping step occurred. As expected, the granules' average compressive strength remained low (0.3 N). They were nonetheless subjected to gamma irradiation and steam, after which they demonstrated

slightly higher compressive strengths (0.5 and 0.4 N, respectively) and BET surface areas (770 and 1051 m^2 g^{-1}, respectively). Finally, the granules were charged with 7.8 mg of labelled radioiodine per gram of MOF, then subjected to conditions mimicking a severe nuclear accident (30 hours at 120 °C under a pressure of 3.5 bar of humid air (R.H. = 20%) and ^{60}Co irradiation). No loss of ^{131}I$_2$ was observed.

As a conclusion, granulation is a widely used shaping technique to produce spherical beads of a few millimeters in diameter. Granulation is only possible through the addition of solvents and binders, which facilitate coagulation between the individual MOF particles. Therefore, special care should be given to the MOFs whose structure might collapse upon addition of a solvent (water or alcohols). For example, HKUST-1 undergoes hydrolysis in the presence of moisture; hence its granulation can only be done under restricted conditions. In turn, binders are divided into inorganic and organic and serve to reinforce the mechanical stability of the final beads. Depending on their nature and amount, they can strongly affect the textural and chemical properties of the original MOF powders. Some of the features are highlighted in Table 8.

Extrusion

Extrusion is another important manufacturing process used in many industrial productions such as metallurgy, plastics, food, and pharmaceuticals. Besides, extrusion is considered to be the most commonly used technique for shaping catalysts and adsorbents for industrial applications in fixed-bed reactors. As the main principle, extrusion relies on passing the preformed paste inside an extruder through a die. Depending on the form of the die, the final objects can have different shapes: hollow tubes, sheets, strips, or cylinders with various cross-sections. This wide variety of final morphologies makes extrusion an advantageous shaping technique as compared to pelletization or granulation. A typical body shaped via extrusion is referred to as an extrudate. Generally, in order to formulate a parent powder into extrudates, it is necessary to first suspend it in a liquid (usually water) to form a paste. The thus-formed paste is further transferred into an extruder where it is pushed with a piston/ram or a screw towards the die (Fig. 6). Upon passing the die, the extrudates (sheets, cylinders) are cut into pieces of desired length and subsequently dried to remove the residual solvent.

Table 8 Types of binders and their effect on the properties of pristine MOF powders

| MOF | Binder, wt% | Effect of the binder on different properties | | | Ref. |
		Mechanical	Textural	Chemical/adsorption	
Fe-MIL-100	ρ-Alumina, 5	Crushing strength of 6.7 N	~12% loss of BET SSA, higher than binder content	No alteration of acidic properties, preservation of Lewis acid sites	57
UiO-66	Sucrose, 10	5% breakage upon tumbling after 60 h at 25 rpm	50% loss of BET SSA	45% loss of H$_2$ adsorption capacity	73
Fe-MIL-100	PVA, 2	Only 2% weight loss upon attrition for 18 h in a mill	3% loss of BET SSA, consistent with binder content	Higher NH$_3$ adsorption capacity than that after pelletization	74
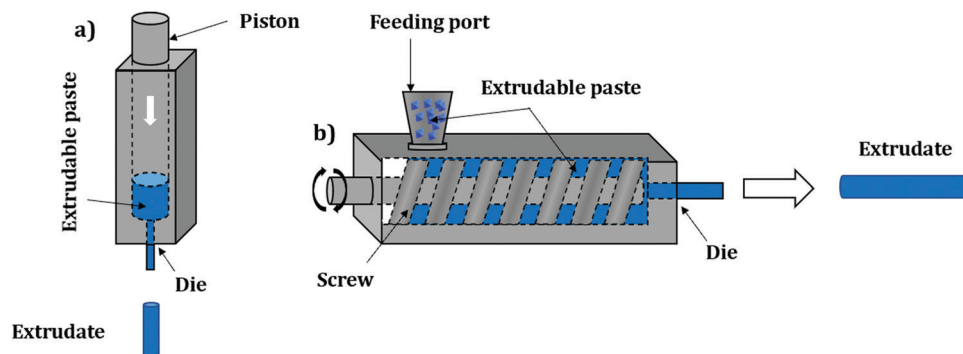
Fig. 6 Schematic representation of the extrusion process on a piston-type extruder (a) and on a single screw-type extruder (b).

Generally, extruders are divided into screw and piston types. The former allows continuous processing and might consist of one (single screw), two (twin screw) or multiple screws which operate in simultaneous and parallel rotations. On the other hand, piston extruders operate in batch mode; however, they enable the extrusion of pastes with high viscosity and compaction.

The paste formulation is crucial and requires special attention. Indeed, mixing of the parent powder with a liquid should yield a paste with suitable rheological properties to enable extrusion. There are many aspects which define the flow behavior such as the size and shape of the powder particles, their chemical properties, *etc.* Overall, the paste viscosity is dictated by the liquid content and can be decreased upon increasing the total liquid/solid ratio. More viscous pastes might require higher pressures for displacement within an extruder; however, unlike pelletization, extrusion does not affect as much the compaction of the particles as they are suspended in a liquid. Besides, in some cases the flowability,

plasticity, or ability of the paste to withstand deformation upon extrusion can be enhanced by adding plasticizers. These are typical organic compounds based on cellulose or polyalcohols which facilitate the formation of the overall network. Generally, they are removed from the final extrudate composition by calcination.

As with granulation, extrusion implies the addition of binders to ensure sufficient mechanical strength to extrudates by developing cross-linking forces between the individual particles. Therefore, the choice of binder and its content are governed by the same principles as in the case of granulation and pelletization. Namely, the binder should provide sufficient mechanical stability with the minimum loss of intrinsic physical and chemical properties of the parent powder. Thus, zeolites extruded with clays and boehmite as binders and cellulose-based plasticizers experienced certain alterations of textural and chemical properties as well as a clear enhancement of mechanical resistance.[77]

Removal of organic components (plasticizer and binder) from extrudates strongly depends on the thermal stability of

Table 9 List of MOFs shaped *via* extrusion

MOF	Metal/ligand	Binder, wt%	Plasticizer	S_{BET}, m^2 g^{-1} Powder	Extrudates	Ref.
Piston extruder						
HKUST-1	Cu/1,3,5-BTC	MSE, 8.2	MHPC	—	484	78
UiO-66-COOH	Zr/1,2,4-BTC	Polysilox. resin, 5.5	H$_2$O	710	418 (−41%)	55
Single screw extruder						
HKUST-1	Cu/1,3,5-BTC	Kaolinite, 20	H$_2$O	1750	900 (−49%)	79
MIL-101	Cr/BDC	Bentonite, 40	H$_2$O	202^a	183^a (−9%)	80
MIL-101	Cr/BDC	Bentonite, 25	H$_2$O	346^a	195^a (−44%)	81
Manual extrusion						
HKUST-1	Cu/1,3,5-BTC	PVA, 15	H$_2$O	1737	963 (−45%)	48
HKUST-1	Cu/1,3,5-BTC	PVA, 2.9	H$_2$O/PrOH	∼1700	∼1610 (−5%)	84
UTSA-16	Co/CA	PVA, 2–3	H$_2$O/PrOH	—	—	82
UTSA-16	Co/CA	PVA	H$_2$O/PrOH	—	805	83
ZIF-8	Zn/MIM	PVA, 2.9	H$_2$O/PrOH	∼1680	∼1640 (−2%)	84
ZIF-8	Zn/MIM	PVC	DMF	—	—	86
MOF-74	Mg/2,5-(OH)$_2$BDC	KH570	MeOH	1230	1170 (−5%)	85
MIL-53	Al/BDC	MC, 2–10	H$_2$O/EtOH	1525	1280 (−16%)	87
MIL-53-NH$_2$	Al/2-NH$_2$BDC	MC, 2–10	H$_2$O/EtOH	—	—	87

Ligand codes: 1,3,5-BTC – benzene-1,3,5-tricarboxylic acid; 1,2,4-BTC – benzene-1,2,4-tricarboxylic acid; BDC – benzene-1,4-dicarboxylic acid; CA – citric acid; and MIM – 2-methyl imidazole. Binder codes: MSE – methoxy-siloxane ether; PVA – polyvinyl alcohol; PVC – polyvinyl chloride; KH570 – 3(trimethoxysilyl)propyl methacrylate; and MC – methyl cellulose. Plasticizer codes: MHPC – methyl hydroxyl propyl cellulose and DMF – *N*,*N*-dimethylformamide. "—" not specified. ^{a} Measured by Hg intrusion.

the parent powder. Zeolites, alumina, and silica are able to withstand calcination and therefore organic removal without structural changes. However, this is not the case for MOFs. Hence, upon extrusion, binders and plasticizers are usually retained in the extrudates due to the limited thermal stability of MOFs (Table 9).

Piston extruder

The pioneering work on MOF extrusion was made by Küsgens et al.[78] They successfully shaped HKUST-1 using a ram extruder by mixing the pre-synthesized MOF powder with methoxy-siloxane ether $(CH_3Si(O)_{1.1}(OCH_3)_{0.8})$ as a binder and methyl hydroxyl propyl cellulose as a plasticizer. They proposed an optimal composition of the paste for the forming process: 180 g of MOF, 80 g of water, 25 g of binder, and 20 g of plasticizer. The paste was subsequently extruded and cut into 200 mm-long strings which were dried at 120 °C for several hours to remove the residual water. The XRD pattern of the thus-shaped extrudates matches with that of the parent HKUST-1 powder, indicating the preservation of the MOF crystal structure upon extrusion in the presence of water. However, N_2 physisorption resulted in a S_{BET} of 484 m^2 g^{-1}, which is fairly low for this MOF even when taking into account 36 wt% of organic additives and suggests either partial hydrolysis of the HKUST-1 framework or pore blockage.

Khabzina et al. also studied the use of UiO-66-COOH extrudates for NH_3 removal.[55] Extrusion was accomplished in a piston extruder through a 1.5 mm die. For a typical formulation, the predefined amount of the parent MOF (72.5 vol%) was mixed with a polysiloxane-based resin as a binder (5.5 vol%) and water (22 vol%). The thus-formed paste was further transferred into the extruder to produce 300 mm long extrudates. They were further dried at room temperature and cut into ~1.5 mm length. According to N_2 physisorption measurements, the extrudates retained around 60% of the initial specific surface area upon shaping the parent powder, making up 418 and 710 m^2 g^{-1}, respectively. The core of the study was the exceptional performance of the extrudates for NH_3 capture as compared to commercial activated carbon-based (AC) adsorbents. The UiO-66-COOH extrudates reached, respectively, 40 and 34 mg cm^{-3} of volumetric NH_3 uptake at 0 and 40% relative humidity when subjected to a flow of N_2 containing an NH_3 concentration of 1200 ppm. At the same time, the commercial AC exhibited 20 and 29 mg cm^{-3}, respectively. The same trend was observed for the breakthrough time, reaching 48 and 43 minutes for the MOF extrudates, against 21 and 32 minutes for the AC. Besides, the authors stated a considerable resistance of the extrudates to attrition, with a mass loss of 1.4% upon sieving (Table 10).

Interestingly, the authors also performed other types of shaping on UiO-66-COOH. As seen from Table 10, not only the extrudates but also the pellets compressed at 97 bar outperformed the commercial adsorbent (AC). At the same time, the relatively poor performance of the beads made via freeze granulation was attributed to their low bulk density.

Table 10 Adsorptive and mechanical properties of UiO-66-COOH shaped bodies[55]

Adsorbent	NH_3 uptake at 1200 ppm, mg cm^{-3}		Breakthrough time, min		Attrition,[a] %
	0% RH	40% RH	0% RH	40% RH	
Extrudates	40	34	48	43	1.4
Compressed pellets	33	33	41	40	1.7
Beads	14	16	18	20	0
Commercial AC	20	29	21	32	0.2

[a] Attrition tests were performed by rotating a cylinder containing a baffle and the shaped UiO-66-COOH at 60 rpm for 30 min. The percentage corresponds to the total mass of the fine particles – less than 425 μm – after sieving.

Single screw extruder

Studies on HKUST-1 extrusion were also performed by Majano and Pérez-Ramírez.[79] A HKUST-1 powder with a specific surface area of 1750 m^2 g^{-1} was mixed with 20 wt% kaolin as a binder and water was used to induce paste formation. The paste was further pushed through a 2 mm die using a single screw extruder, and the extrudates were subsequently dried at 65 °C overnight. As confirmed by XRD, the crystal structure was retained upon extrusion, but N_2 physisorption revealed a S_{BET} of 900 m^2 g^{-1}. This value is around 50% of the initial surface area of the HKUST-1 powder and indicates considerable pore blocking caused by the binder, and/or partial framework hydrolysis.

A study by Hong et al.[80] was conducted on the extrusion of Cr-based MIL-101 for CO_2 adsorption, using a single screw extruder and bentonite clay as a binder. A predefined amount of MIL-101 powder was mixed with bentonite clay (40 wt%) and water to form a paste. The paste was further extruded into monoliths with square channels which were subsequently dried at 10 °C for several days followed by firing at 150 °C for 33 h. Upon firing, the extrudates were cut into 7 cm long cylinders (Fig. 7a). According to the XRD patterns, the MIL-101 crystal structure was retained upon processing. However, the extrudates demonstrated reflections with considerably lower intensities, which was attributed by the authors to the binder's presence. Moreover, the extrudates experienced a small decrease of their textural properties, yielding a specific surface area of 183 m^2 g^{-1}, while it was 202 m^2 g^{-1} for the MOF powder – as measured by mercury intrusion. It should be noted that MIL-101 generally has a way higher specific surface area – even exceeding 5000 m^2 g^{-1} – when assessed by N_2 physisorption. In line with the mercury intrusion measurements, the CO_2 adsorption capacity of the MIL-101 extrudates and powder reached 1.5 and 1.9 mmol g^{-1} at 4.5 bar and 25 °C, respectively.

Recently, Hong et al.[81] published a comparative study to assess the CO_2 adsorption capacities of MIL-101 and 13X zeolite extrudates, the benchmark adsorbent. The extrusion process was nearly the same as described in their previous work with a slight modification of the paste composition to lower the binder content to 25 wt% (against 40 wt%) and the drying step to 5 °C (against 10 °C), while firing was increased to 205 °C
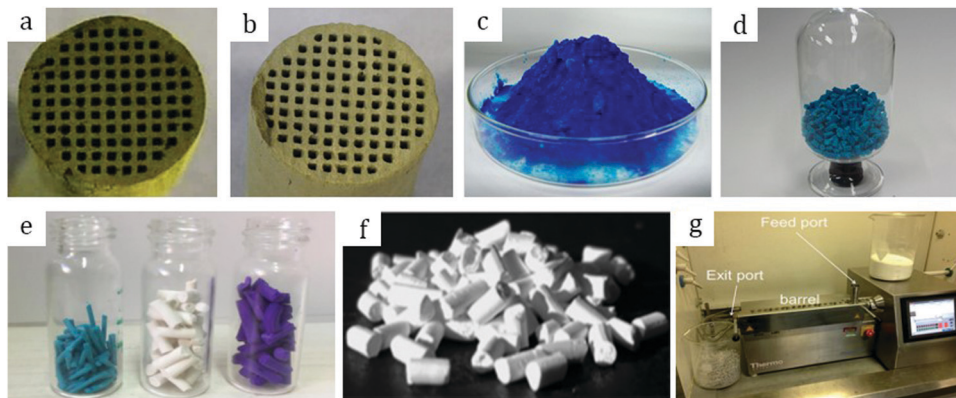
Fig. 7 Photograph of MIL-101 extrudates (a) of 7 cm long cylinders with a channel size of 0.9 mm made by Hong *et al.*[80] Copyright 2015 Elsevier. Photograph of MIL-101 extrudates (b) of 10 cm long cylinders with a channel size of 0.9 made by Hong *et al.*[81] Copyright 2020 Elsevier. As-synthesized HKUST-1 (c) and its extruded form (d) prepared by Kim *et al.*[48] Copyright 2012 Elsevier. HKUST-1 (left), ZIF-8 (middle), and UTSA-16 (right) extrudates (e) prepared by Delgado *et al.*[84] Copyright 2017 Elsevier. MIL-53 extrudates (f) prepared by Kriesten *et al.*[87] Copyright 2019 Wiley. A twin screw extruder (g) used by Crawford *et al.*[92] Copyright 2015 The Royal Society of Chemistry.

(against 150 °C) (Fig. 7b). The thus-prepared extrudates exhibited a specific surface area, as assessed by Hg intrusion, of 195 m^2 g^{-1}, comparable to the MIL-101 powder. As a result, the MIL-101 extrudates demonstrated a CO_2 breakthrough adsorption capacity of 1.11 mmol g^{-1}, higher than that of 13X zeolite extrudates (0.81 mmol g^{-1}) under 2 bar (absolute pressure) of 40 vol% CO_2 at room temperature.

Manual extrusion

In some cases, the extrusion process can be reproduced using laboratory or home-made equipment. Thus, Kim *et al.*[48] reported the manual fabrication of $Cu_3(BTC)_2$ (HKUST-1) extrudates. Typically, they first formed a paste by mixing the parent MOF with the binder, a 15 wt% solution of polyvinyl alcohol in water. Thereafter, the paste was transferred to a home-made extruder, and the as-produced extrudates were subsequently cut and dried at 120 °C for 12 h under vacuum (Fig. 7c and d). Upon extrusion, the crystal structure of HKUST-1 was preserved as confirmed by the XRD patterns. However, there was a considerable decrease in specific surface area associated with shaping, from 1737 to 963 m^2 g^{-1}. The total loss, around 45%, indicates partial pore blocking. Similar results were reported by Majano and Pérez-Ramírez[79] when using 20 wt% kaolin as a binder.

The extrudates were further applied for CO_2 and water-vapor adsorptions. The latter revealed identical isotherm shapes for both the powder and extrudates. This suggests that the intrinsic hydrophilicity/hydrophobicity balance of HKUST-1 was not altered upon shaping. Besides, CO_2 adsorption experiments at 25 °C revealed gravimetric uptakes of 218 and 129 mg g^{-1} for the MOF in powder and extruded forms, respectively. The decrease of CO_2 uptake demonstrated by the latter is in agreement with the loss in specific surface area upon extrusion.

In 2014, Grande *et al.*[82] performed a study on the manual extrusion of Co-based UTSA-16 with emphasis on the paste composition. To form the paste, they combined polyvinyl alcohol as the binder and a water/propanol (1/1) mixture as the plasticizer. The paste was further extruded into strips using a syringe of a chosen diameter. The thus-shaped MOFs were then dried at 80 °C for 12 h. When varying the binder content, no significant loss in specific surface area with 2 wt% binder was observed. A further increase to 3 wt% PVA led to a 5% loss of SSA. Notably, the authors stated that an activation temperature lower than 120 °C was insufficient to remove the water/propanol mixture. At the same time, 2 wt% binder was found to be adequate to provide a decent crushing strength of around 20 N upon conventional compression tests, comparable to commercial zeolite 4A extrudates (12 N). For comparison, the absence of a binder resulted in a lower mechanical strength of around 7 N.

The adsorptive capacities of these UTSA-16 extrudates towards model gases, and especially CO_2, were evaluated in a following study by Agueda *et al.*[83] As compared to their powder counterpart, the UTSA-16 extrudates, exhibiting a BET surface area of 805 m^2 g^{-1}, demonstrated a 15% loss of CO_2 uptake at 25 °C. This was attributed to the partial pore blocking caused by the binder presence. Still, the CO_2 uptake of the extrudates is in the same range (4.0 mol L^{-1} at 1 bar) as those of commercial adsorbents based on activated carbon and zeolite 13X: 1.5 and 5.5 mol L^{-1} at 1 bar, respectively.

Following UTSA-16, Delgado *et al.*[84] studied the extrusion and resulting adsorptive properties of HKUST-1 and ZIF-8 extrudates (Fig. 7e). Their textural properties as measured by N_2 physisorption revealed a moderate decrease in surface area when shaped with 2.9 wt% binder, from 1700 m^2 g^{-1} (HKUST-1 powder) to 1610 m^2 g^{-1} (HKUST-1 extrudates, ~5% loss). The loss was even reduced to 2% for ZIF-8, from 1680 to 1640 m^2 g^{-1}. This indicates a negligible pore blocking effect caused by the binder, as reported by Grande *et al.*,[82] as well as excellent structural stability upon manual extrusion – while HKUST-1 experienced a more pronounced textural and structural degradation using piston and single-screw extruders. As expected, the ZIF-8 extrudates demonstrated lower H_2 and CO_2 uptakes as compared to HKUST-1 extrudates in a temperature range of 25–65 °C and pressures up to 50 bar, due to the lower

affinity of gases with the ZIF-8 surface. As a link to the previous studies, heats of CO_2 adsorption for the given MOFs as well as for the UTSA-16 extrudates were provided. The latter showed the highest value of released heat (38 kJ mol^{-1}) at 20 bar and 25 °C, twice as much as those of the HKUST-1 and ZIF-8 extrudates. This indicates a considerable affinity of the UTSA-16 surface towards CO_2, making it a promising candidate for CO_2 capture.

Another study on manual extrusion was done by Pu et al.[85] They investigated the shaping of Mg-based MOF-74/CPO-27 with KH570 (3-(trimethoxysilyl)propyl methacrylate) as a binder. For a typical extrusion procedure, they mixed a pre-defined amount of the parent MOF with a KH570 methanolic solution to form a paste. It was then extruded through a 1 mL injection syringe to form strips which were subsequently dried and cut into the final extrudates with dimensions of 1.5 mm length and 2 mm diameter. This procedure had no visible effect on the structure of the extruded MOF crystals as observed by XRD. Moreover, the thus-shaped MOF-74 exhibited a SSA of 1170 m^2 g^{-1}, as compared to 1230 m^2 g^{-1} ($\sim$5% drop) shown by its powder form as measured by the BET method with CO_2 as the adsorbate. The extrudates presented a slightly preferential uptake of ethylene (6.06 mmol g^{-1}) over ethane (5.49 mmol g^{-1}) at 25 °C and 1 bar, as in the case of its powder counterpart (7.37 and 6.61 mmol g^{-1}, respectively). Of note, the deterioration of adsorptive properties upon extrusion exceeds 5% and might thus indicate partial pore blocking. Comparatively, zeolite 13X, one of the commercial adsorbents, demonstrates ethylene and ethane uptakes of 3.32 and 2.70 mmol g^{-1}, respectively, under the same conditions.

The study by Cousin-Saint-Remi et al.[86] addressed the careful choice of binder for the preparation of mechanically stable extrudates from ZIF-8 powder, a MOF demonstrating relative stability upon more constraining processes such as pelletization (Table 3). Within the scope of their study, a series of binders were tested but only a few yielded robust objects. Thus, when shaped with typical inorganic binders such as silica, bentonite or kaolinite clays, the final objects broke apart upon extrusion. Methylcellulose and polystyrene were not appropriate either, due to the targeted application – COV adsorption. Therefore, a few polymeric binding agents, namely polyvinyl chloride (PVC), polyvinyl formal (PVF) and polyetherimide (PEI), yielded appropriate extrudates. For a typical formulation procedure, 1 g of the parent MOF was mixed with 7.5–30 wt% binder followed by the gradual addition of 10 mL of solvent (DMF, DMSO or DMA). The thus-formed paste was extruded through the 2 mm-tip of a syringe and subsequently dried overnight at room temperature. These extrudates were further applied to ethanol vapor adsorption at 50 °C, and the results suggested a slight decrease in total gravimetric capacity at 127.5 mbar for the ZIF-8 extrudates compared to their parent powder, from 0.28 to 0.24 g g^{-1} ($-$15%). This decrease agrees with the total content of binder, suggesting a negligible pore blocking effect caused by its presence. Furthermore, the breakthrough experiments done with a mixture of acetone, ethanol and 1-butanol diluted in water demonstrated the preferential adsorption of the latter on ZIF-8. Notably, the extrudates exhibited a broadening of elution profiles compared to the powder, indicating additional diffusion resistance created by the binder.

Extrusion of an Al-based MIL-53 MOF was studied by Kriesten et al.[87] They investigated more specifically the framework "breathing" properties of MIL-53 and their evolution upon shaping. For the shaping procedure, they mixed a predefined amount of the parent MOF with 2–10 wt% methyl cellulose (MC) as a binding agent followed by the dropwise addition of a 50/50 vol% water/ethanol mixture. Upon mixing, the thus-formed homogeneous paste was further extruded through the 5 mm-tip of a syringe to draw strips which were dried at room temperature, and finally cut into extrudates with lengths of 1.8 to 4.4 mm and diameters of 1.33 to 2.22 mm (Fig. 7f). As confirmed by XRD, the crystallinity of MIL-53 was preserved upon shaping for all the extrudates with a binder content of up to 10 wt%. Furthermore, they retained the majority of their intrinsic textural properties. Thus, the parent MIL-53 exhibited a S_{BET} of 1525 m^2 g^{-1}, while the extrudates with 2, 5 and 10 wt% MC showed S_{BET} of 1405, 1280 and 1158 m^2 g^{-1} corresponding to 5.9, 11.6 and 15.5% decreases, respectively. The difference might indicate a slight pore blocking effect caused by the binder. Notably, a second type of MC binder with higher molecular weight yielded a comparable decrease in BET surface area.

Interestingly, the framework "breathing" property of MIL-53 was shown to be preserved upon shaping by in situ XRD under humid conditions. Indeed, the phase transition from large to narrow pores was demonstrated to take place over the 20–45% relative humidity (RH) range. Higher RH resulted in a faster phase transition. It was thus evident that the binder had no hindrance to the transition, and in fact, there was no relation between its content and the kinetics of the phase transition. Moreover, this breathing property was also observed upon CO_2 adsorption at 30 °C. As with N_2, there was only a slight decrease of total CO_2 uptake ($\sim$4%) upon adsorption on MIL-53 extrudates formed with 3 wt% binder as compared to the powder. Furthermore, the shape of the isotherm was preserved, revealing the breathing phenomenon resulting in an isotherm with a hysteresis loop.

Reactive extrusion

Reactive extrusion, related to mechanochemical synthesis, is generally based on reactions between solid precursors with little to no solvent added. The energy needed to initiate the reactions is classically provided by frictions and shocks as found in milling or grinding processes. The main advantage of the mechanochemical approach for MOF synthesis is the minimization or complete avoidance of the use of solvents which are often hazardous liquids. Up to now, this approach has been applied to many MOFs among which are HKUST-1,[88] ZIF-8,[89] UiO-67,[90] and MOF-5.[91] Although mechanochemistry allows faster syntheses as compared to classical solvent-assisted syntheses, its up-scaling remains an issue.

In 2015, Crawford et al.[92] described the mechanochemical synthesis of MOFs using a twin screw extruder (TSE) (Fig. 7g), thus combining synthesis and shaping in one step. Indeed, the

rotating screws composed of different zones (conveying, shearing, kneading) displace the starting solid MOF precursors along the heated barrel with good control over the residence time, and the mixing duration and intensity. Hence, through the combination of shearing and compression forces, solid-state reactions between the precursors can be obtained. Ideally, upon reaching the exit port, the product is formed and it is further drawn through a die into extrudates. Of note, the controllable heating of the barrel allows better control over the reaction conditions as compared to conventional milling approaches.

For instance, the authors used copper hydroxide and trimesic acid mixed with methanol as a feed material to produce HKUST-1. Upon extrusion at room temperature, the product was washed with ethanol and dried to yield HKUST-1 extrudates with a specific surface area of 1738 $m^2\ g^{-1}$ and a crystal structure expected for this MOF. Furthermore, the authors showed that ZIF-8 extrudates can be made by both single and twin screw extrusion processes. For this, they used a blend of zinc carbonate and 2-methylimidazole with no solvent added and extruded it at 200 °C. In both cases, the processes yielded a crystalline product with the ZIF-8 topology and high surface areas: 1604 $m^2\ g^{-1}$ (twin screw) and 1750 $m^2\ g^{-1}$ (single screw). Lastly, the authors produced a highly crystalline Al-fumarate with a BET surface area of 1010 $m^2\ g^{-1}$ by extruding a mixture of Al-sulfate, fumaric acid and sodium hydroxide at 150 °C. It is worth noting that this approach enables the production of MOFs with decent space-time yields (STY) as single and twin screw extrusions are continuous processes.

To conclude, extrusion is another widely used technique to process MOF powders into different shapes. Compaction of the individual MOF particles is driven by the difference of diameter between upstream and downstream while keeping constant the flowrate. For flowability to be obtained, the MOF powders are typically mixed with a binder and a plasticizer, with the latter enabling the formation of a rheofluidifying paste. Since the binder cannot be removed from a shaped MOF object, certain care should be given to fine-tuning the binder content in order to avoid critical pore blocking. Generally, extruders with different forms and numbers of screws allow the formation of hollow or dense objects with different shapes and sizes. This advantage makes extrusion a preferred technique over pelletization. In addition, manual extrusion of a paste through a syringe is also possible. Comparative data are given in Fig. 8 for two well-studied MOFs: HKUST-1 and ZIF-8.

A positive effect of extrusion is evident from Fig. 8 as in the case of ZIF-8; the loss in surface area upon extrusion is negligible (−2%) and coherent with the amount of added binder, while upon pelletization the loss in surface area is more pronounced (−13%). At the same time, for HKUST-1 the decrease in surface area is somewhat comparable upon pelletization and extrusion. However, the latter is made with 20 wt% binder, which causes drastic pore blocking, while the loss in surface area upon pelletization is due to the considerable framework collapse.

3D printing

3D printing (also known as "additive manufacturing" or "robocasting") has attracted significant interest as a shaping tool over the past decade. Its recent applications have expanded beyond the fabrication of thermoplastic composites for daily use to find unique applications in medicine, architecture and many other fields.[93] As with other shaping techniques in materials science, 3D printing enables the assembly of parent powders into solid 3D objects of various shapes and sizes. It specifically allows the manufacture of structured adsorbents or catalysts for large industrial reactors. For MOFs, the most common technology applied is direct ink writing (DIW).[94] The basic principle of this method resembles the conventional extrusion process and is composed of similar steps. Namely, the first step implies the formation of a paste by suspending the parent powder in a liquid (water or short-chain alcohols).

Fig. 8 Comparison of the extruded[84] and pelletized[38] ZIF-8 (left); and the pelletized[47] and extruded[79] HKUST-1 (right). Numbers indicate the BET SSA upon shaping the pristine powder into extrudates and pellets.
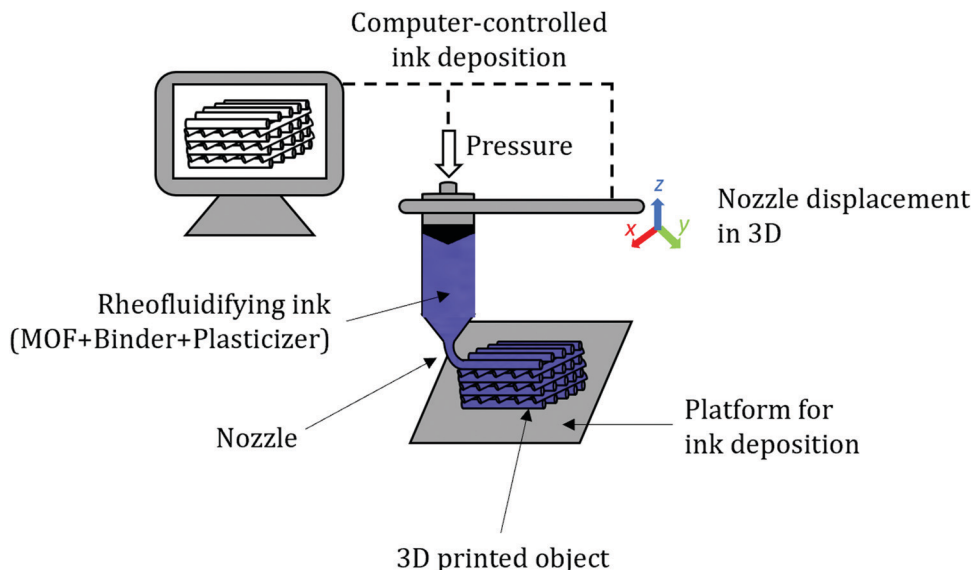
Fig. 9 Schematic representation of the 3D printing process *via* the Direct Ink Writing (DIW) method.

Thereafter, the paste is pushed through a thin printing nozzle and subsequently deposited on a substrate in a controllable layer-by-layer manner designed using a slicing software package. Upon building up the desired object with a pre-defined geometry and dimensions, it is further subjected to a thermal treatment for the removal of the liquid constituents. Apart from DIW, other approaches include Digital Light Processing (DLP) and Selective Laser Sintering (SLS). The former employs UV irradiation to locally cure a resin containing a monomer and the parent powder. In turn, SLS implies the melting of a thermoplastic material with a laser beam in the presence of the parent powder.

A typical 3D printer for DIW consists of a substrate, a nozzle (syringe or extrusion head) and a series of interconnected vertical and horizontal bars which enable the displacement of the nozzle along the x, y, and z axes (Fig. 9). The substrate is also mobile and often responsible for the movement along the x and y axes.

As in the case of extrusion, the paste formulation is a crucial step in 3D printing and should yield a final composition with appropriate rheological properties. Apart from the parent powder and a liquid, the paste is also composed of a binder and a plasticizer. The former provides adequate mechanical resistance to the final 3D objects, while the latter improves the flowability and plasticity of the paste to be printed. One of the major differences is the printing nozzle: while the die in extruders can reach sizes up to a few centimeters, in 3D printers the nozzle (or needle) is typically smaller than millimeters in diameter. Such a thin nozzle allows designing objects with complex geometries that would be challenging to obtain *via* a conventional method.

Recently, 3D printing has been applied to a large number of structured adsorbents and catalysts. Thus, Al_2O_3 was shown to be printable into monoliths exhibiting high catalytic efficiency as well as good recyclability.[95] Zeolites 13X and 5A have also

been printed into monoliths for CO_2 removal purposes,[96] while a 3D-printed zeolite (ZSM-5) has been probed for CO_2, CH_4 and N_2 separation. Among the other printed structures can be found carbons,[97] amorphous aluminosilicates[98] and other classes of adsorbents.[99]

3D printed MOFs have become a frequently discussed topic in the literature. Their excellent textural properties make them promising materials for gas adsorption, storage and purification purposes. These include the most studied representatives such as HKUST-1, ZIF-8 and UiO-66 (Table 11).

As is evident from Table 11, different binder/plasticizer systems have been probed, as well as a binderless approach. In some cases, the mechanical stability of the printed objects is provided by polymer matrices on which MOFs are deposited upon printing.

MOF growth on pre-printed matrices

The earliest studies on 3D printing include the surface coating of a thermoplastic polymeric matrix, acrylonitrile butadiene styrene (ABS), with a Cu-based HKUST-1 MOF by Wang *et al.*[100] The authors first immersed the printed ABS objects in a solution containing the Cu-precursor, followed by immersion in a solution containing the organic ligand. Eventually, the objects were dried and washed prior to further immersion. The procedure was repeated up to 8 cycles (Fig. 10a). Upon the final drying step, the HKUST-1/ABS composites were shown to exhibit reflections characteristic of HKUST-1, revealing its successful crystallization on the ABS surface. Moreover, the composite was able to remove methylene blue from an aqueous solution, due to the Cu^{2+} sites present in the MOF.

Following a comparable method, Zhang *et al.* deposited up to eight layers of HKUST-1 on PLA films.[101] After the eighth cycle and further activation, a dark blue film was obtained, presenting the main diffraction peaks of HKUST-1 in its XRD pattern. Moreover, crystals with an octahedral shape are clearly

Table 11 List of MOFs formulated *via* 3D printing

MOF	Metal/ligand	Binder, wt%	Plasticizer	S_{BET}, m² g⁻¹ Powder	S_{BET}, m² g⁻¹ 3D object	Ref.
MOF growth on pre-printed matrices						
HKUST-1	Cu/BTC	ABS	None	—	—	100
HKUST-1	Cu/BTC	PLA	None	—	—	101
HKUST-1	Cu/BTC	SiO₂	None	—	223	103
UTSA-16	Co/CA	Kaolin, 10	MC	630	620 (−2%)	102
MIL-100	Fe/BTC	SiO₂	None	—	82	103

MOF	Metal/ligand	Matrix, wt%	Plasticizer, wt%	S_{BET}, m² g⁻¹ Powder	S_{BET}, m² g⁻¹ 3D object	Ref.
Direct writing of MOF-based inks (DIW) within polymer matrices						
MOF-5	Zn/BDC	ABS, 90	None	—	—	104
HKUST-1	Cu/BTC	ABS, 90	None	776	329 (−58%)	105
ZIF-8	Zn/MIM	ABS, 90	None	1446	436 (−70%)	105
ZIF-8	Zn/MIM	PLA, 60	None	1752	531 (−70%)	106
ZIF-8	Zn/MIM	TPU, 40	PVDF-HFP, 20	1752	706 (−60%)	106
UiO-66	Zr/BDC	TPU, 40	PVDF-HFP, 20	1144	303 (−74%)	106

MOF	Metal/ligand	Binder, wt%	Plasticizer	S_{BET}, m² g⁻¹ Powder	S_{BET}, m² g⁻¹ 3D object	Ref.
Direct writing of MOF-based inks (DIW)						
UTSA-16	Co/CA	Bentonite, 10	PVA	631	444 (−30%)	107
UTSA-16	Co/CA	Boehmite, 31	HPC	—	540	118
Ni(bdc)(ted)₀.₅	Ni/BDC, TED	PVA, 20	EtOH:DMSO	1802	1325 (−27%)	108
CPL-1	Cu/PZDC, PYZ	HEC, 6.7	PVA	198	68 (−66%)	115
UiO-66-NH₂	Zr/2-aminoBDC	HEC, 7.3	PVA	1123	871 (−22%)	115
HKUST-1	Cu/BTC	HEC, 19.5	PVA	1581	1181 (−25%)	115
HKUST-1	Cu/BTC	SA	Gelatin	1563	83 (−95%)	116
HKUST-1	Cu/BTC	None	EtOH	1850	1134 (−39%)	117
HKUST-1	Cu/BTC	Bentonite, 21	MC:PVA	830	500 (−40%)	111
HKUST-1	Cu/BTC	Bentonite, 15	PVA	830	470 (−43%)	111
HKUST-1	Cu/BTC	Torlon, 37.5	PVP	—	290	110
MOF-74	Ni/2,5-(OH)₂BDC	Torlon, 52.9	PVP	—	80	110
MOF-74	Ni/2,5-(OH)₂BDC	Bentonite, 15	PVA	1180	737 (−38%)	107
ZIF-7	Zn/BIM	Silica, 15	H₂O:MeOH	16	40	108
ZIF-8	Zn/MIM	Bentonite, 16.7	MC	1415	1070 (−24%)	112
ZIF-8	Zn/MIM	HEC, 13.2	PVA	1711	1690 (−1%)	115
ZIF-8	Zn/MIM	SA	TOCNF	—	900	119
MIL-100	Fe/BTC	SA	TOCNF	—	—	119
MIL-101	Cr/BDC	Bentonite, 15	PVA	2400	2200 (−8%)	109

MOF	Metal/ligand	Matrix, wt%	Photoinitiator	S_{BET}, m² g⁻¹ Powder	S_{BET}, m² g⁻¹ 3D object	Ref.
UV irradiation-assisted 3D printing, digital light processing (DLP)						
UiO-66	Zr/BDC	TMPPTA, 44	HMPP, PPO	1590	633 (−60%)	120
HKUST-1	Cu/BTC	PEA/PGD	I-819, I-184	—	—	121
HKUST-1	Cu/BTC	AAm, 25	I-2959	—	—	122

MOF	Metal/ligand	Matrix, wt%	Plasticizer	S_{BET}, m² g⁻¹ Powder	S_{BET}, m² g⁻¹ 3D object	Ref.
Laser-assisted 3D printing, selective laser sintering (SLS)						
NH₂-MIL-101	Al/2-aminoBDC	PA12	None	—	—	123
MOF-801	Zr/FA	PA12	None	—	—	123
HKUST-1	Cu/BTC	PA12	None	—	—	123
HKUST-1	Cu/BTC	PA12	None	—	40	124
ZIF-67	Co/MIM	PA12	None	—	640	123
ZIF-8	Zn/MIM	PA12	None	1359	332 (−76%)	123

Ligand codes: BTC – benzene-1,3,5-tricarboxylic acid; CA – citric acid; BDC – benzene-1,4-dicarboxylic acid; MIM – 2-methyl imidazole; TED – 1,4-biazabicyclo[2.2.2]octane; BiM – benzimidazole; PZDC – pyrazine-2,3-dicarboxylic acid; PYZ – pyrazine; and FA – fumaric acid. Binder/matrix codes: ABS – acrylonitrile-butadiene-styrene; PLA – polylactic acid; TPU – thermoplastic polyurethane; PVA – polyvinyl alcohol; HEC – 2-hydroxyethyl cellulose; SA – sodium alginate; TMPPTA – trimethylolpropane propoxylate triacrylate; PEA – 2-phenoxyethyl acrylate; PGD – polyethylene glycol diacrylate; PA12 – polyamide 12; and AAm – acrylamide + *N*,*N*′-methylenebisacrylamide (0.06 wt% acrylamide). Plasticizer codes: MC – methyl cellulose; HPC – hydroxypropylcellulose; DMSO – dimethyl sulfoxide; TOCNF – 2,2,6,6-tetramethylpiperidine-1-oxyl radical-mediated oxidized cellulose nanofibers; PVP – polyvinylpyrrolidone; and PVDF-HFP – poly(vinylidene fluoride-*co*-hexafluoropropylene). Photoinitiator codes: HMPP – 2-hydroxy-2-methylpropiophenone; PPO – phenylbis(2,4,6-trimethylbenzoyl)phosphine oxide; I-189 – Irgacure-819; I-184 – Irgacure-184; and I-2959 – Irgacure-2959. "—" not specified.

Fig. 10 Photographs of MOFs grown on pre-printed matrices: HKUST-1/ABS composites (a) printed in the form of numbers representing the number of cycles prepared by Wang et al.[100] Copyright 2014 Springer Nature. 3D shapes made with 1%, 5%, and 10% MOF-5 composites (b); filament used in the printing process (c); 3D object with a scale (d); image of the designed object (e); and top and side views of the 3D printed object (f and g) prepared by Kreider et al.[104] Copyright 2017 Wiley.

visible in the SEM images. This functionalized film was applied for malachite green remediation in river water at a concentration of 10 mg L^{-1}. After 10 minutes, 90% of the initial MG was adsorbed. The film was recycled up to 5 times, however with a certain decrease of efficiency over the cycles.

Another post-printing MOF growing method was applied by Lawson et al.,[102] who prepared UTSA-16/kaolin 3D printed composites. A paste was composed of a binder (kaolin), a plasticizer (methyl cellulose) and UTSA-16 precursors with adjustable loadings. Further, the paste was extruded into monoliths and subsequently exposed to solvothermal conditions to initiate crystal growth. This procedure enabled the obtention of UTSA-16/kaolin composites, with MOF loadings as high as 90 wt%. According to XRD, the monoliths exhibited patterns matching with the pristine UTSA-16 powder. Besides, they exhibit pronounced textural properties with a S_{BET} of 620 m^2 g^{-1}, as high as that of their powder analogue (630 m^2 g^{-1}). These composites were shown to exhibit excellent CO$_2$ separation properties over a mixture of CH$_4$, N$_2$ and H$_2$. Thus, the MOF-loaded monolith demonstrated CO$_2$/CH$_4$, CO$_2$/N$_2$ and CO$_2$/H$_2$ selectivities of 49, 238 and 3725, respectively. These values are comparable to those of the pristine UTSA-16 powder (52, 250, and 3750, respectively).

More recently, Zhou et al.[103] deposited two MOFs, HKUST-1 and MIL-100(Fe), on the surfaces of silica grids printed following the direct-ink writing (DIW) approach and presenting two levels of macroporosity: large macropores of about 1 mm, generated by 3D-printing a grid-like pattern, and smaller macropores of about 2 μm, due to the addition of polystyrene beads in the ink. After combustion of the beads and sintering at 900 °C, fully macroporous solids were obtained (total pore volume = 0.01 cm^3 g^{-1} as given by N$_2$ physisorption). The grids were then surface-treated with KOH solution and coated with dopamine hydrochloride to improve the MOFs' adhesion. Finally, MIL-100(Fe) and HKUST-1 MOFs were grown at the surfaces of the macropores under solvothermal conditions. The obtained MOFs were highly crystalline and the crystal size was about 100 nm. All bands identified by XPS and FT-IR spectroscopy were attributed to the MOF structures. Finally, these grids were attached to a 3D-printed plastic stirring device, and used for the Fenton-like catalytic degradation of a blend of dyes (methylene blue, rhodamine B, malachite green and crystal violet, 20 mg L^{-1} each) from wastewater. 0.9 M H$_2$O$_2$ was added

prior to each cycle, and up to 50 cycles were performed. Based on UV-visible spectrometry, after 20 minutes complete degradation of the dyes was observed with both MOFs at the end of the first cycle, while after 50 cycles the activity decreased to 75% and 52% using MIL-100(Fe) and HKUST-1, respectively.

Instead of depositing MOFs at the surfaces of pre-printed structures, another more direct approach would be to print MOF–polymer composite filaments. This pathway was first published by Kreider et al.,[104] who addressed the shaping of the Zn-based MOF-5 into monoliths via the use of a conventional thermoplastic 3D printer using ABS as the matrix. Although ABS is amongst the most used thermoplastic polymers for 3D printing, it only improves the mechanical stability of the printed objects by providing its own properties rather than by generating bonds with the individual MOF particles. Therefore, the amount of polymer should be adequately large to provide sufficient mechanical resistance to the final printed objects. Thus, the authors dissolved ABS in acetone with addition of a certain amount of pre-synthesized MOF-5 (from 1 to 10 wt%, on a dry basis). Upon solvent evaporation, the film was recovered and extruded into 1.75 mm-wide filaments, which were subsequently 3D-printed via a nozzle heated at 230 °C onto a platform heated at 115 °C to yield objects of different shapes (Fig. 10b–g).

The thus-shaped objects were found to exhibit XRD patterns similar to a MOF-5 degraded by humidity. This was attributed to the formulation procedure prior to printing rather than to the printing procedure itself. Nevertheless, these 3D printed objects were shown to have the ability to adsorb H$_2$ despite the complex polymer environment.

Nearly the same 3D printing process was applied by Bible et al.[105] to prepare ZIF-8/ABS and HKUST-1/ABS composites with a MOF content of 10 wt%. Interestingly, the composites exhibited reflections characteristic of the parent MOF powders, suggesting that the crystal structures were preserved upon the formulation procedure. Moreover, as said previously HKUST-1-based materials tend to degrade upon exposure to a humid environment. However, the XRD pattern of a HKUST-1/ABS composite remained unchanged after keeping it in water for a week, suggesting that ABS, a hydrophobic material, prevents water from binding with Cu^{2+} ions and thus prevents significant hydrolysis. Both composites exhibited adsorptive features towards nitrogen with specific surface areas, S_{BET}, of 436 and

329 m^2 g^{-1} for ZIF-8/ABS and HKUST-1/ABS, respectively. Notably, the absence of a sharp increase in N$_2$ uptake at low pressures, characteristic of microporous materials, was attributed to the slowed diffusion of N$_2$ through the ABS-containing objects, and therefore incomplete micropore filling.

A similar methodology adopted by Evans et al.[106] yielded rigid ZIF-8/PLA (polylactic acid) composites with MOF contents up to 40 wt%. To achieve a homogeneous dispersion within the polymer matrix, the MOF powder was first suspended in ethyl acetate and mixed with PLA dissolved in CH$_3$Cl. The mixture was cast and left for drying before subsequent extrusion. Eventually, the thus-extruded filaments were used for 3D-printing through a 400 μm diameter nozzle preheated at 200 °C. This protocol yielded 3D printed composites with XRD patterns presenting well-resolved reflections characteristic of ZIF-8, along with a S_{BET} of up to 531 m^2 g^{-1}, as compared to 1752 m^2 g^{-1} for the original ZIF-8 powder (−70%). This suggests blocking by few pores caused by PLA. The same shaping procedure was repeated with a thermoplastic polyurethane (TPU) polymer to yield flexible ZIF-8/TPU composites with the same 40 wt% MOF loading. Interestingly, a higher S_{BET} of 706 m^2 g^{-1} was retained (−60% compared to the powder), suggesting that the whole porosity remained accessible. Finally, the authors applied their methodology for the 3D-printing of another emblematic MOF, UiO-66, giving a composite material presenting a S_{BET} of 303 m^2 g^{-1}.

Direct writing of MOF-based inks (DIW)

The first successful trial of direct ink writing using MOFs was performed by Thakkar et al.,[107] who shaped MOF-74 and UTSA-16 powders into monoliths. For this purpose, they used bentonite clay as a binder and polyvinyl alcohol (PVA) as a plasticizer. Firstly, the paste formation step included mixing two solutions: the MOF powder and the binder in ethanol (1) and the PVA dissolved in water and ethanol (2). Upon mixing, the paste was transferred into a syringe and extruded through a 0.85 mm diameter nozzle in a layer-by-layer fashion, yielding monolith

structures with uniform channels. Eventually, the printed objects with dimensions of 1.5 cm height × 1.5 cm diameter were dried at 100 °C to prevent cracks.

The thus-shaped MOFs were extensively characterized. The crystal structure was demonstrated by XRD to be preserved upon 3D printing. The slightly lower reflection intensities were attributed to the binder and plasticizer presence. In agreement with that, N$_2$ physisorption measurements showed a consequent decrease in S_{BET} upon printing, from 1180 to 737 m^2 g^{-1} for MOF-74 and from 631 to 444 m^2 g^{-1} for UTSA-16. This suggests a decrease of 38 and 30% compared to their powder analogue, respectively. Interestingly, while the pore size distribution remained unchanged in the case of MOF-74, with the majority of pores in the range of 1–4 nm, the UTSA-16 monoliths were shown to possess mesopores 20–25 nm in size. This was attributed to the formation of straight channels as the result of interactions between the water present in the paste and the citrate units in the MOF framework. The cross-sectional area of the monoliths viewed via SEM revealed wall thicknesses/channel widths of 0.4/0.7 mm and 0.8/1.1 mm for MOF-74 and UTSA-16, respectively. Interestingly, this alteration of the size originated from the different viscosities of the two pastes. Thus, the less viscous UTSA-16 paste expanded upon deposition and yielded thicker walls and larger channel sizes as compared to the more viscous MOF-74 paste (Fig. 11a). The MOF monoliths were further applied to CO$_2$ adsorption measurements. Starting from a 0.5% CO$_2$/N$_2$ gas mixture, the CO$_2$ uptake capacities of MOF-74 and UTSA-16 3D-printed solids reached 1.35 and 1.31 mmol g^{-1}, respectively. These values correspond to 79 and 87% of the CO$_2$ uptake capacity of the corresponding MOF powders and agree with their total content in the monoliths.

A further study by Thakkar et al.[108] addressed the 3D printing of two MOFs, Ni-based Ni(bdc)(ted)$_{0.5}$ and Zn-based ZIF-7, for ethane-selective adsorption. The paste was formed by mixing pre-synthesized Ni(bdc)(ted)$_{0.5}$ dispersed in EtOH with PVA dissolved in DMSO. After evaporation of a consequent fraction of EtOH a homogeneous, extrudable paste was

Fig. 11 Photographs of objects 3D-printed via the DIW method: monoliths (a) prepared by Thakkar et al.[107] Copyright 2017 American Chemical Society. Ni(bdc)(ted)$_{0.5}$ monolith (b) with its SEM images (c and d) and SEM images of ZIF-7 (e and f) monoliths prepared by Thakkar et al.[108] Copyright 2018 American Chemical Society. ZIF-8 monolith (g) and its optical image (h) made by Lefevere et al.[112] Copyright 2019 American Chemical Society.

obtained. In the case of ZIF-7, the paste was formed by first mixing the pre-synthesized MOF powder and silica with the subsequent addition of a water:methanol mixture. Upon mixing at 60 °C, the composition turned into a smooth, homogeneous paste. Each paste was loaded into a 3 mL tube equipped with a piston and extruded through a 0.85 mm nozzle into monoliths in a layer-by-layer manner. Eventually, the thus-formed 3D objects were dried at 100 °C for a few hours (Fig. 11b–f).

The XRD patterns of the monoliths were found to be comparable to those of their powder analogues, suggesting that the crystal structure was retained upon shaping. The intensities however experienced a certain decrease, which was attributed to the presence of PVA. Further analyses revealed pronounced textural properties for Ni(bdc)(ted)$_{0.5}$ as given by N$_2$ physisorption. Its monolithic form exhibited a S_{BET} of 1325 m^2 g^{-1}, while its powder form presented a S_{BET} of 1802 m^2 g^{-1}. The difference was 27%, a value which agrees well with the initial MOF content in the paste (80 wt%). The corresponding values for ZIF-7 were 16 and 40 m^2 g^{-1}, respectively, for its powder and printed forms. Its porosity is inaccessible to N$_2$ and the slightly higher available surface area was attributed to the silica binder in the printed composition. Interestingly, conventional compression tests revealed an excellent mechanical stability of up to 1.7 MPa for Ni(bdc)(ted)$_{0.5}$ due to the high content of binder (20 wt%), which provided considerably strong bonding of particles. At the same time, ZIF-7 monoliths withstood compression up to 0.8 MPa, showing that silica might be less appropriate than PVA for strongly bonding MOF particles. When probed for ethane/ethylene adsorption, Ni(bdc)(ted)$_{0.5}$ monoliths showed total uptakes of 4.1 and 2.9 mmol g^{-1}, respectively. These values were found to be proportional to the MOF content. Notably, ZIF-7 monoliths showed total uptakes of 1.8 and 2.5 mmol g^{-1}, respectively. Both isotherms exhibited an S-shape, revealing the pore-opening feature of this MOF upon increasing pressure.

In another study, Lawson et al.[109] addressed the 3D printing of Cr-based MIL-101 for CO$_2$ capture. The paste formation and printing processes were similar to those reported by Thakkar et al.[107] Eventually, they succeeded in printing MIL-101 monoliths with bentonite clay (15 wt%) as the binder and PVA (5 wt%) as the plasticizer. Such a composition yielded printed objects with a S_{BET} of 2200 m^2 g^{-1}, which is only ∼8% less than that of the pristine powder (2400 m^2 g^{-1}). The corresponding CO$_2$ uptakes at 1 bar and 25 °C were 0.75 and 1.0 mmol g^{-1}, respectively. Notably, the decrease in the uptake is consistent with the MOF loading (80 wt%). Besides, the authors functionalized the monoliths with amino groups via pre- and post-impregnation using polyethylenimine (PEI) and tetraethylene-pentamine (TEPA) to enhance the CO$_2$ capture. The presence of amino moieties was confirmed by FTIR analysis through a broad contribution in the range of 3600–2750 cm^{-1}, while the intrinsic MOF peaks were preserved. This suggests the structural integrity of the MOF upon printing. Interestingly, TEPA-MIL-101 and PEI-MIL-101 composite monoliths showed an improved CO$_2$ uptake of, respectively, 2.6 and 1.7 mmol g^{-1}.

Table 12 CO$_2$ adsorption capacities of the MOFs prepared by Lawson et al.[109] under 3000 ppm CO$_2$ in N$_2$ at 25 °C

| MOF | CO$_2$ adsorption capacity, mmol g^{-1} | | Ref. |
	Powder	Printed monoliths	
UTSA-16	1.00	0.50	107
MOF-74	1.25	1.00	107
Zeolite 13X	1.40	1.20	96
Zeolite 5A	1.45	1.25	96
TEPA-MIL-101	1.63	1.60	109

Moreover, the impregnated objects demonstrated higher values of CO$_2$ capture under 3000 ppm of CO$_2$/N$_2$ than commercial benchmark adsorbents (Table 12), making them promising materials for the CO$_2$ capture.

Lawson et al.[110] also investigated the use of Torlon®, which is a family of polyamide-imides with good mechanical, chemical and thermal stability, as a binder. The mixture of Torlon®, MOF powder (HKUST-1 or MOF-74(Ni)), N-methyl-2-pyrrolidone (NMP), water and DMF (for HKUST-1) was rolled for at least 24 hours prior to use. Woodpile structures with channels of 1 mm were printed, but the resulting printing quality was fairly poor. Moreover, the microporosity of both printed MOF structures, HKUST-1 and MOF-74(Ni), was drastically reduced. For instance, the HKUST-1 solid printed with 37.5 wt% Torlon® displayed a S_{BET} of 290 m^2 g^{-1}, while the MOF-74(Ni) structure collapsed following hydrolysis as observed by PXRD. Notably, the MOF/Torlon® composites presented a mechanical resistance of over 637 MPa, three magnitudes higher than that of the solids obtained with bentonite (0.48–0.56 MPa). Their CO$_2$ adsorption capacity at 25 °C was examined, but the resulting capacities were lower than those previously mentioned (0.6 mmol g^{-1} for HKUST-1/Torlon® and 0.3 mmol g^{-1} for MOF-74(Ni)/Torlon®).

Finally, Lawson et al.[111] studied the post-printing crystallization of HKUST-1 starting from a gel containing all precursors. In this case, a mixture of bentonite (21 wt%), methylcellulose (2 wt%) and PVA (6 wt%) was used to obtain satisfactory rheological properties. The as-printed grids presented a fair replication of the initial model, and they were further placed in a convection oven at 120 °C for 20 hours to induce crystallization of the MOF. The resulting material presented a S_{BET} of 500 m^2 g^{-1}, slightly higher than that of a comparative solid directly 3D-printed starting from the HKUST-1 powder (470 m^2 g^{-1}). While the solids were extensively washed with acetone, residual DMF was observed by FTIR spectroscopy as characterized by a band at 2100 cm^{-1}. Finally, the CO$_2$ capacities of both solids at 25 °C were compared. While the solid prepared from the HKUST-1 powder presented a CO$_2$ capacity 50% higher (2.1 mmol g^{-1} against 1.4 mmol g^{-1}), which is not in line with their respective S_{BET}, the solid obtained by growing HKUST-1 crystals on the as-printed solid displayed enhanced mass transfer kinetics (diffusivity × 10^8 (cm^2 s^{-1}): 8.75 against 5.25). This was attributed to the presence of a larger extent of mesopores (V_{meso} (cm^3 g^{-1} STP) = 0.16 against 0.09).

Further reports on shaping ZIF-8 *via* DIW include the work by Lefevere *et al.*,[112] who managed to formulate the MOF with a blend of inorganic and organic binders. The former was added to improve the mechanical stability of the shaped objects, and the latter to enhance the rheological properties of the paste. Typically, the parent ZIF-8 powder (66.7 wt%) was mixed with bentonite (16.7 wt%) and methylcellulose (16.7 wt%) with a subsequent addition of water and mixing to form a homogeneous printable paste. Once homogenized, it was further loaded into a 50 mL syringe and extruded through 250 and 600 μm diameter nozzles in a layer-by-layer fashion at room temperature (Fig. 11g and h).

Upon printing, the objects were thermally treated in an inert atmosphere to remove the organic binder. It was found that elimination of methyl cellulose without structural degradation of ZIF-8 took place at 450 °C. Upon such thermal treatment, the ZIF-8 and bentonite contents in the printed objects were 80 and 20 wt%, respectively. The crystal structure remained intact upon thermal activation as confirmed by XRD diffractograms. Besides, IR analysis demonstrated the preservation of the bands characteristic of the original MOF powder, with additional bands at 1100 cm^{-1} corresponding to Si–O stretching, implying the presence of bentonite. Ar physisorption measurements revealed a 24% decrease of S_{BET}, from 1415 $m^2\ g^{-1}$ (ZIF-8 powder) to 1070 $m^2\ g^{-1}$ (ZIF-8 monolith). This decrease is consistent with the binder content and suggests only a minor pore blocking. Further adsorption studies of a gas mixture (ethanol, *n*-butanol, isopropanol and water) on ZIF-8 monoliths demonstrated the preferential adsorption of *n*-butanol at 40 °C as it eluted the last, with a breakthrough time of 43 h. Further studies on *n*-butanol adsorption from an acetone–butanol–ethanol (ABE) gas mixture over 3D printed ZIF-8 were done by Claessens *et al.*[113] They showed a higher affinity of *n*-butanol towards ZIF-8 monoliths and therefore their eligibility for the separation of *n*-butanol from the ABE gas mixture.

3D printing also enabled the preparation of porous conducting matrices as cathode supports based on MOFs for Li-O$_2$ batteries in a study by Lyu *et al.*[114] For this purpose, they chose Co-based ZIF-67 which was mixed with Pluronic F127 in water

to form a printable ink. The latter was used to generate a hierarchical porosity within the shaped objects. The paste was further transferred into a 20 mL syringe equipped with nozzles of up to 400 μm and printed in a layer-by-layer manner. Upon printing, the composites were dried and decomposed at 800 °C under N$_2$ to form Co nanoparticles entrapped in N-doped mesoporous carbon flakes. These materials exhibited a BET surface area of 640 $m^2\ g^{-1}$. The thus-formed Co-based electrocatalysts increased the cell's specific energy and therefore the energy density value up to 798 W h kg_{cell}^{-1}, which is higher than those of the currently well-established Li-ion batteries. This suggests the integration of MOF-derived carbon-based nanomaterials as promising composites for advanced battery systems.

A detailed study on the rheology of printable inks was done by Dhainaut *et al.*[115] on a series of MOFs. Namely, Cu-based CPL-1 and HKUST-1, Zr-based UiO-66-NH$_2$, and Zn-based ZIF-8 inks were formulated. A typical paste was prepared by mixing a predefined amount of the parent MOF, polyvinyl alcohol (PVA) as the plasticizer, and a gel of 2-hydroxyethyl cellulose (HEC) as the binder. The paste was further extruded through a 0.8 mm diameter needle in a layer-by-layer manner on a surface preheated at 60 °C. Eventually, the thus-printed objects were exposed to vacuum drying at 90 °C (Fig. 12a and b). All crystal structures were retained upon printing, as confirmed by matching XRD patterns. A decrease in the intensities of the reflections was attributed to the presence of organic additives within the 3D objects. Besides, the gas (N$_2$ and CO$_2$) sorption capacities of these materials experienced a certain drop upon printing; however, the values mostly remained in the range of the organics' percentages (Table 11), as estimated by TGA measurements. As evidenced from Table 11, HKUST-1 experienced a higher (24%) loss of S_{BET} as compared to the estimated content of organic additives. This can be explained by the partial degradation of the framework upon dispersion in a water/ethanol mixture during the paste formation step. Nevertheless, methane adsorption experiments revealed decent uptakes of 81, 55 and 38 g kg^{-1}, respectively, for printed HKUST-1, ZIF-8 and UiO-66-NH$_2$ monoliths at 25 °C and 40 bar. The values are
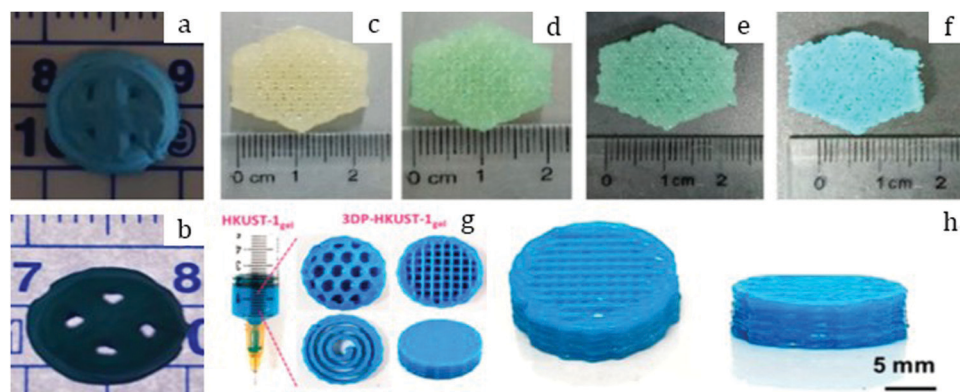

Fig. 12 Photographs of objects 3D-printed *via* the DIW method: CPL-1 before (a) and after drying (b) prepared by Dhainaut *et al.*[115] Copyright 2020 American Chemical Society. Printed objects with HKUST-1 loadings of 0% (c), 2.5% (d), 3.7% (e) and 13% (f) prepared by Pei *et al.*[116] Copyright 2020 Elsevier. HKUST-1 gel in a syringe (g) and monoliths (g and h) prepared by Lim *et al.*[117] Copyright 2019 American Chemical Society.

close to the ones reported for their powder analogues. Interestingly, adsorption of ethane/ethylene gas over printed CPL-1 monoliths revealed no ethane uptake above 8 bar, while adsorption of ethylene increased linearly up to 16 bar, thus making this MOF a highly-preferential ethylene adsorbent.

Direct ink writing of HKUST-1 was also reported by Pei et al.[116] The paste was formed by mixing a pre-synthesized HKUST-1 powder with sodium alginate and gelatin in water until a homogeneous ink was formed. The latter was then printed through a 0.21 mm nozzle in a layer-by-layer manner at room temperature. The thus-formed objects were then immersed in a $CaCl_2$ solution to initiate cross-linking and eventually exposed to drying at 80 °C to obtain the final objects (Fig. 12c–f). As confirmed by XRD, the printed HKUST-1 objects exhibited reflections characteristic of the original powder, suggesting that the crystal structure remained intact upon printing. Besides, the S_{BET} was 83 m^2 g^{-1} at ~13 wt% HKUST-1 loading, while its powder counterpart reached 1563 m^2 g^{-1}, suggesting a drastic 95% loss and therefore pore blocking caused by the alginate species and gelatin. Nevertheless, it was shown that the printed objects retained the adsorptive properties of the parent MOF towards the most common dyes and exhibited recyclability properties. Thus, the removal efficiency of the 3D printed objects towards methylene blue increased from 43.6 to 79.5, 90 and 96% as the HKUST-1 loading increased from 0 to 2.5, 3.7 and 13%, respectively. The results were consistent upon 10 consecutive adsorption–regeneration cycles.

The binderless shaping of HKUST-1 via DIW was reported by Lim et al.[117] They demonstrated that a colloidal gel containing only the parent MOF dispersed in ethanol can serve as an ink for printing at room temperature. This paste was extruded through a syringe with a 300 μm diameter tip to yield circular objects with a diameter of 15 mm and a thickness of 2 mm. Eventually, the thus-shaped objects were dried in a desiccator (Fig. 12g and h).

According to XRD results, the printed objects retained the original crystal structure of HKUST-1 upon formulation. A certain peak broadening was observed for all materials, suggesting small MOF crystals. Indeed, as confirmed by SEM, the shaped objects were composed of HKUST-1 crystals with sizes in the 20–50 nm range. However, a significant decrease of the S_{BET} was measured, from 1850 m^2 g^{-1} for the parent powder to 1134 m^2 g^{-1} for the 3D-printed solids. As no binder was present, this decrease might be ascribed to the partial collapse of the HKUST-1 framework.

Lately, Grande et al. applied 3D-printed UTSA-16 solids for selective CO_2 capture.[118] For the binding system, they used a mixture of boehmite and hydroxypropyl cellulose, representing 36 wt% of the final dry solid content. Interestingly, the presence of boehmite might provide some Lewis acidity, which was not probed. The as-obtained solids with a diameter of 28 mm presented a woodpile structure with only little sagging in the middle. After activation, the S_{BET} reached 540 m^2 g^{-1}, which is higher than expected as UTSA-16 powder typically presents a S_{BET} of 630 m^2 g^{-1}. While the solids retained selectively CO_2 over N_2, the additional presence of water molecules desorbed the CO_2 molecules.

A one-pot approach based on the in situ growth of ZIF-8 and MIL-100 MOFs onto anionic cellulose nanofibers (TOCNF) was first described by Sultan et al.[119] The latter acts as an anchor for stabilizing ionic Zn and Fe species, prior to their precipitation in the presence of triethylamine. The water-based ink was formulated by mixing the metal precursor solution, TOCNF, TEA, and the linker solution. Prior to printing, sodium alginate was added as a plasticizer to improve the ink printability.
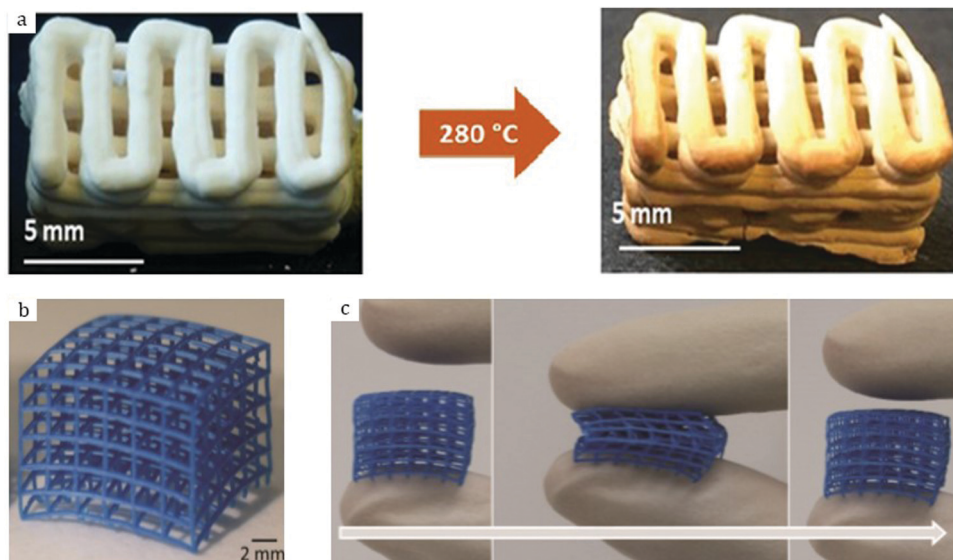

Fig. 13 Photographs of objects 3D-printed via the DLP method: UiO-66 composite (a) before and after drying prepared by Young et al.[120] (the color change from white to light-brown was attributed to the polymer and photoinitiator degradations). Copyright 2019 Royal Society of Chemistry. HKUST-1/polymer composite (b) and demonstration of its flexibility (c) prepared by Halevi et al.[121] Copyright 2017 Wiley.

Monoliths of 8 cm^3, with a pore size of 1 mm and a wall thickness of 0.5 mm, were obtained following ink deposition using a 410 μm diameter nozzle and a printing speed of 10–80 mm s^{-1}. This protocol was finalized by subsequent soaking of the printed object in a calcium chloride solution, acting as a cross-linking agent. Furthermore, it was shown that drugs can be encapsulated into the printed objects with a subsequent pH-dependent release. Thus, curcumin, an anticancer drug, was encapsulated in both TOCNF/ZIF-8 and TOCNF/MIL-101, while methylene blue, a hemoglobin-regulating drug, was incorporated into TOCNF/ZIF-8. Hence, 3D printing was demonstrated to be suitable for preparing MOF-based drug carriers. Both active compounds were shown to be released under acidic conditions at pH ~5.5.

UV irradiation-assisted 3D printing, digital light processing (DLP)

Young et al.[120] used a DLP approach to print MOF-based objects. In their work, the ink was formulated by mixing the parent MOF with ethanol and adding an acrylate-based polymer binder (trimethylolpropane propoxylate triacrylate (TMPPTA) and EBECRYL® 8413) as well as an initiator blend (phenylbis(2,4,6-trimethylbenzoyl)phosphine oxide in 2-hydroxy-2-methylpropiophenone). The thus-formed paste with a total MOF content of 52 wt% was further loaded into a 25 mL syringe and extruded through a 16-gauge (~1.3 mm) needle at room temperature. The objects were irradiated with 365 nm UV-light during printing prior to heating at 280 °C for 30 min (Fig. 13a). This was followed by washing with dichloromethane and drying at 50 °C under vacuum. The printed objects retained the crystal structure of the original UiO-66 powder as was evident from the matching XRD patterns and FTIR bands. Besides, a band corresponding to vinyl groups (at around 2900 cm^{-1}) vanished upon printing, indicating the successful polymerization of the binder following UV-light irradiation. Furthermore, the binder partially liberated the porosity when removed by heating, yielding a specific surface area of 633 m^2 g^{-1}, while that of its powder analogue was 1590 m^2 g^{-1}.

A similar approach was developed by Halevi et al.,[121] starting from Cu-based HKUST-1 powder to obtain MOF-embedded flexible polymeric structures. For this purpose, they used a blend of 2-phenoxyethyl acrylate (PEA) and polyethylene glycol diacrylate (PGD) as the polymeric matrix, while Irgacure-819 and Irgacure-184 were applied as photoinitiators. The ink containing all components and a MOF content of 10 wt% was loaded into a DLP 3D printer to yield flexible HKUST-1/polymer 3D composites (Fig. 13b and c). The use of a hydrophobic polymer matrix enhanced the hydrolytic stability of the water-sensitive HKUST-1 and enabled its use for the adsorption of methylene blue (MB) in an aqueous medium. Thus, the HKUST-1/polymer composite retained around 6.5 mg g^{-1} of MB, which is comparable to the 7 mg g^{-1} capacity of the pristine MOF powder. However, for a longer adsorption duration (around 9 h) the latter released MB back into the aqueous solution, indicating its structural collapse due to hydrolysis. Instead, the 3D printed composite retained the adsorbed MB after 9 h, owing to its enhanced stability in water.

Liu et al. developed a DLP approach based on the use of a DIW 3D printer.[122] For that, they formulated an ink in which, in addition to gelling agents (hydroxyethyl cellulose and sodium alginate), 25 wt% acrylamide and 0.4 wt% of a photoinitiator were also added. The resulting solids were photocured for 15 minutes, prior to immersion in a suspension containing HKUST-1 precursors. After 24 hours, HKUST-1 crystals were formed onto and within the photocured solids as observed by SEM. However, the main reflection of HKUST-1 was barely visible by XRD, indicating that at least some of the Cu^{2+} remained amorphous. The resulting MOF composites
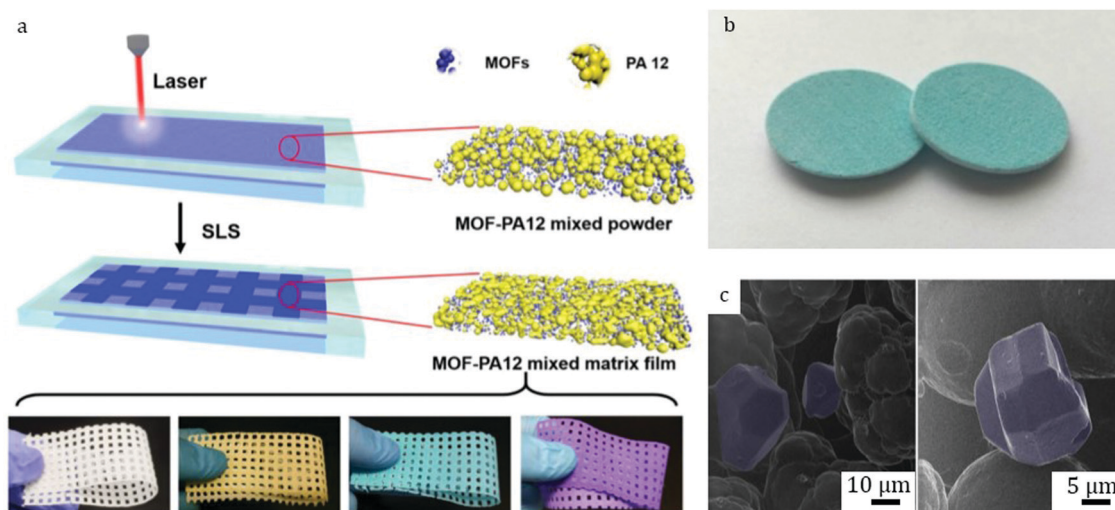

Fig. 14 Schematic representation of the SLS 3D printing process (a, top) and photograph of printed objects: MOF/polymer matrices (a, bottom) from left to right: PA12 film, NH$_2$–MIL–101/PA12, HKUST–1/PA12, ZIF–67/PA12 prepared by Li et al.[123] Copyright 2019 American Chemical Society. MOF/PA12 composites with 20 mm diameter and 1.5 mm thickness (b) and HIM images of their surfaces with MOF particles highlighted in purple (c) prepared by Lahtinen et al.[124] Copyright 2019 Wiley.

presented a large shape deformation (453%) and a high tensile strength (278 kPa). When applied to MB adsorption (30 μm in water), full adsorption was observed after 5 hours. Unfortunately, the recyclability was not reported.

Laser-assisted 3D printing, selective laser sintering (SLS)

The SLS technology was successfully employed by Li et al.[123] to produce a series of MOF-polymer mixed matrix films (MMFs) starting from polyamide 12 (PA12) and five different MOFs: ZIF-67, NH$_2$-MIL-101, MOF-801, HKUST-1 and ZIF-8. Each of the MOF powders was thoroughly mixed with the matrix before deposition as a thin layer on a quartz support. Then, a CO$_2$ laser beam ($\lambda \sim 10.6$ μm) was applied at a scanning speed of 1.78 m s^{-1} and a laser power of 9.6 W (16% of maximal power, to avoid MOF decomposition). Eventually, MMFs with differently-sized grid patterns and MOF contents up to 40 wt% were formed (Fig. 14a). As confirmed by the XRD analysis, the thus-formed films retained the initial MOF crystal structure while also exhibiting broad reflections attributed to PA12. Besides, the MMF containing 40 wt% ZIF-8 exhibited a surface area of 332 m^2 g^{-1}, against 1359 m^2 g^{-1} for pure ZIF-8 powder. Hence, while partial pore blockage was caused by the PA12 matrix, the MOF particles were not encapsulated into the polymer matrix and remained accessible for adsorption of guest molecules. Thus, the MMF containing NH$_2$-MIL-101 was demonstrated to be as efficient as its powder counterpart for methylene blue adsorption (81% removal efficiency), and it retained its performance after 5 adsorption–desorption cycles.

The same SLS method was applied by Lahtinen et al.[124] to produce HKUST-1/PA12 porous filters with a MOF loading of 10 wt%. A 14 W CO$_2$ laser operating at 40% laser power and 2.4 m s^{-1} laser speed was employed to obtain the composites (Fig. 14b and c). The temperature of printing was set to 170 °C, which was low enough to retain the crystal structure of HKUST-1 within the polymer matrix, as confirmed by XRD. Besides, HKUST-1/PA12 pellet-like composites exhibited a moderate S_{BET} of 40 m^2 g^{-1}, which was attributed to the low MOF content. Nevertheless, the printed filters presented an adsorption capacity for CO$_2$ in line with the MOF content, reaching a 0.6 wt% increase in mass upon adsorption, while the pristine powder exhibited a 6.0 wt% increase. This suggests that the SLS technique brings no significant alteration of the structural and chemical properties of pristine MOF powders.

To sum up, 3D printing is a relatively new shaping technique which is based on extrusion through a thin tip in a controlled manner. This grants 3D printing some essential advantages over classical extrusion such as a wide variety of possible shapes to form. However, proper control of the rheological properties is crucial in the case of 3D printing as the paste should retain its form once deposited on a substrate. Besides, MOFs can be introduced into a polymer matrix depending on the nature of the latter in different ways (by SLS, DLP or MOF growth on the printed polymer matrix). At the same time, direct writing of MOF-based inks has also been successfully developed. Comparative data are given in Table 13.

Table 13 Comparison of DIW 3D printing and manual extrusion

Technique	MOF	Binder, wt%	Plasticizer	Loss of SSA, %	Ref.
3D printing (DIW)	HKUST-1	HEC, 19.5	PVA	−25	115
3D printing (DIW)	ZIF-8	Bentonite, 16.7	MC	−24	112
Manual extrusion	HKUST-1	PVA, 2.9	H$_2$O/PrOH	−5	84
Manual extrusion	ZIF-8	PVA, 2.9	H$_2$O/PrOH	−2	84

As is evident from Table 13, both extrusion and DIW can yield shaped objects while preserving the textural properties of pristine MOFs. The loss in surface area in the case of the 3D printed objects is somewhat higher than the binder content which is due to the presence of the plasticizer. The final printed objects have a developed network of millimeter-sized channels thanks to the layer-by-layer deposition upon printing. This can significantly improve the diffusion of gas or liquid within the shaped objects.

Spray-drying

The spray-drying technique has been known for over a century. As the name suggests, it is used to dry powder-like materials in a continuous fashion. Compared with ovens and conveyor belts, spray-dryers allow treating several tons per hour of wet product. Over the past few decades, the application potential of spray-drying has considerably expanded and now includes the food industry,[125] the pharmaceutical industry,[126] and many others.[127]

The basic principle behind the spray-drying procedure lies in the atomization of a slurry into micron-sized droplets within a heated chamber. During this process, the droplets containing the dispersed powder are quickly evaporated, leaving the dried powder to be further captured and collected. The spray-drying process strongly relies on the following three parameters: the inlet temperature (T_{in}) up to which the circulating gas is heated, flow rate at which the gas is introduced in the chamber, and feed rate at which the precursor solution or slurry is injected into the atomizer (Fig. 15a). The variation of these parameters depends on the final purpose of spray-drying.

Interestingly, upon drying, the individual particles dispersed in the slurry feed adopt the shape of the atomized droplets and thus form larger, micron-sized spherical agglomerates. Therefore, the entire spray-drying process can also be viewed as a technique for shaping particles into microbeads, particularly adapted for fluidized-bed reactors.[59]

Moreover, spray-drying allows the direct synthesis of various materials.[128] In 2002, du Fresne von Hohenesche et al.[129] successfully prepared MCM-41 spherical microbeads with a defined arrangement of macro- and mesopores with the help of a spray-dryer. Since then, the same approach has been used for preparation of other types of porous materials,[130] allowing spray-drying to be considered as a tool for simultaneous synthesis and shaping.

A few years ago, the group of D. Maspoch[131] developed a strategy for a fast, facile and scalable synthesis of MOFs using a
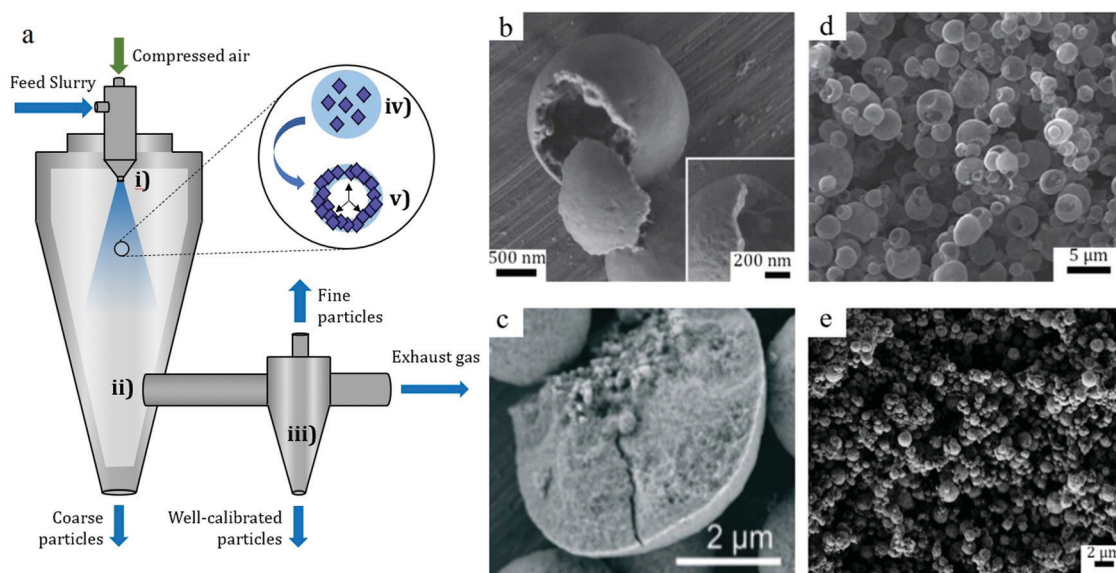
Fig. 15 Schematic representation (a) of the spray-drying process: (i) atomizer; (ii) drying chamber; (iii) cyclone separator for gas/powder separation; (iv) sprayed droplet with a MOF precursor; and (v) dried droplet with MOF crystals at the edge. SEM image of a HKUST-1 hollow bead (b) prepared by Carne-Sanchez et al.[131] Copyright 2013 Springer Nature. SEM image of a UiO-66 dense bead (c), prepared by Garzon-Tovar et al.[138] Copyright 2016 Royal Society of Chemistry. HKUST-1 hollow beads produced with a B-290 Mini Spray Dryer (d) and a Nano Spray Dryer B-90 (e), prepared by Carne-Sanchez et al.[131] Copyright 2013 Springer Nature.

spray-dryer. In a typical synthesis, the solution (or suspension) containing the MOF precursors is atomized into a chamber. There, upon constant contact with a hot gas, the precursors rapidly react, thus forming MOF nanoparticles inside the droplets. At the same time, they are assembled into dense or hollow spherical structures (Fig. 15b and c). Eventually, the droplets are completely evaporated and freshly formed MOF microbeads are collected. This approach has been successfully applied to a wide variety of MOFs, including some of the most-studied HKUST-1, UiO-66, ZIF-8, and MOF-5, among others. Generally, the final size of the microbeads varies from a few hundreds of nanometers to a few microns.

The final shape of the solid particles might alter the MOF's physical and chemical properties. Some of them are summarized in Table 14 with up-to-date references on MOFs produced by spray-drying.

One step synthesis, hollow structures

As evidenced from Table 14, the formation of either hollow or dense microbeads upon spray-drying is primarily dictated by the nature of the MOF itself. Thus, HKUST-1 and ZIF-8 tend to arrange into spheres with a void core, while the whole family of UiO and its derivatives build up into compact, dense microbeads. This trend was first described by Carnez-Sanchez et al.[131] in their pioneering work on using spray-drying for the synthesis of MOFs. They were the first to show that individual droplets sprayed in the chamber could be viewed as microreactors to crystallize MOFs and form spherical hollow superstructures which resulted from the assembly of individual nano-crystallites. Indeed, this approach was successfully applied to a large family of MOFs with a particular stress on the Cu-based

HKUST-1. For its preparation, the feed solution was spray-dried at an inlet temperature of 180 °C, a feed rate of 4.5 mL min^{-1} and a flow rate of 336 mL min^{-1}. This led to the formation of a blue powder composed of spherical agglomerates (superstructures) with an average size of 2.5 ± 0.4 microns and exhibiting the HKUST-1 phase as confirmed by XRD (Fig. 15d). Additionally, the thus-shaped HKUST-1 retained its high porosity, showing a S_{BET} of 1209 m^2 g^{-1}, a value in agreement with HKUST-1 typically prepared under solvothermal conditions.[132] Besides, the authors performed a study on the impact of spray-drying conditions on the morphology of the final superstructures. Namely, an increase in the flow rate from 336 up to 474 mL min^{-1} led to the formation of considerably smaller discrete HKUST-1 nanoparticles forming the superstructures, from 160 ± 40 down to 107 ± 30 nm. At the same time, no considerable impact was observed when decreasing the inlet temperature from 180 down to 100 °C, leaving the mean size unchanged. Interestingly, it was demonstrated that MOF superstructures can be miniaturized by decreasing the size of the sprayed droplets. This can be achieved by using another spray-dryer: for instance, the Nano Spray Dryer B-90 (Büchi Labortechnik) enabled the production of hollow MOF microbeads with an average size of 950 ± 300 nm (Fig. 15e).

Another interesting finding was the possibility to synthesize MOFs such as Fe-based MIL-88A, which instantly produce an amorphous phase once their precursors are mixed at room temperature. Spray-drying allows overcoming this issue by using a three-fluid nozzle which ensures that the precursors do not mix before the drying chamber or just before they enter the atomizer (T-junction). The authors further applied this approach to a large family of MOFs (see Table 14). Furthermore,

Table 14 List of the MOFs produced *via* the spray-drying technique

MOF	Metal/ligand	Spray dryer	T_{in}, °C	Feed rate, mL min^{-1}	Flow rate, mL min^{-1}	S_{BET}, m^2 g^{-1}	Ref.
One step synthesis, hollow structures							
HKUST-1	Cu/BTC	B-290	180	4.5	336	1209	131
HKUST-1	Cu/BTC	B-290	180	4.5	336	1430	133
HKUST-1@PS	Cu/BTC	B-290	130	4.5	336	757	133
Cu-BDC	Cu/BDC	B-290	180	4.5	336	543	131
NOTT-100	Cu/BPTC	B-290	180	4.5	336	1140	131
Cu-PB	Cu/K$_3$Co(CN)$_6$	B-290	180	4.5	474	617	131
MOF-5	Zn/BDC	B-290	180	4.5	336	1215	131
MOF-14	Cu/BTB	B-290	180	4.5	336	—	131
Zn-MOF-74	Zn/DHBDC	B-290	180	4.5	336	—	131
Mg-MOF-74	Mg/DHBDC	B-290	180	4.5	336	—	131
Ni-MOF-74	Ni/DHBDC	B-290	180	4.5	336	—	131
MIL-88A	Fe/FA	B-290	180	4.5	336	—	131
MIL-88B	Fe/2-NH$_2$-BDC	B-290	180	4.5	336	—	131
IRMOF-3	Zn/2-NH$_2$-BDC	B-290	180	4.5	336	—	131
ZiF-67	Co/MIM	AF-88	180	6.7		1861	136
ZiF-8	Zn/MIM	B-290	180	4.5	474	941	131
ZiF-8	Zn/MIM	SD-1000	150	5		1440	134
ZiF-8	Zn/MIM	AF-88	180	6.7		1634	136
Zn/Co-ZiF	Zn, Co/MIM	AF-88	180	6.7		1746	136
MOF	**Metal/ligand**	**Spray dryer**	**T_1/T_{in}, °C**	**Feed rate, mL min^{-1}**	**Flow rate, mL min^{-1}**	**S_{BET}, m^2 g^{-1}**	**Ref.**
Two steps, seed-mediated spray-drying method, dense structures							
UiO-66	Zr/BDC	B-290	80/180	4.5	336	—	131
UiO-66	Zr/BDC	B-290	80/220	5	300	—	137
CID-1	Zr/IP, BPY	B-290	80/220	5	300	—	137
Two steps, continuous flow spray-drying method, dense structures							
UiO-66	Zr/BDC	B-290	115/180	2.4	336	1106	138
UiO-66	Zr/BDC	B-290	115/180	2.4	336	945	143
UiO-66-NH$_2$	Zr/2-NH$_2$-BDC	B-290	115/180	2.4	336	752	138
UiO-66-NH$_2$	Zr/2-NH$_2$-BDC	B-290	90/150	2.4	336	1036	141
UiO-66-NO$_2$	Zr/2-NO$_2$-BDC	B-290	115/180	2.4	336	679	138
UiO-66-Br	Zr/2-Br-BDC	B-290	115/180	2.4	336	527	138
UiO-66-(OH)$_2$	Zr/2,5-(OH)$_2$-BDC	B-290	115/180	2.4	336	401	138
UiO-66-2,6-NDC	Zr/2,6-NDC	B-290	115/180	2.4	336	557	138
UiO-66-1,4-NDC	Zr/1,4-NDC	B-290	115/180	2.4	336	431	138
UiO-66-acetamido	Zr/2,5-(OH)$_2$-BDC	B-290	115/180	2.4	336	586	138
UiO-66-(SH)$_2$	Zr/2,5-(SH)$_2$-BDC	B-290	115/180	2.4	336	597	143
CeO$_2$@UiO-66	Zr/BDC	B-290	115/180	2.4	336	747	143
CeO$_2$@UiO-66-(SH)$_2$	Zr/2,5-(SH)$_2$-BDC	B-290	115/180	2.4	336	539	143
CeO$_2$/Fe$_3$O$_4$@UiO-66-(SH)$_2$	Zr/2,5-(SH)$_2$-BDC	B-290	115/180	2.4	336	—	143
MIL-100	Fe/BTC	B-290	135/180	2.4	336	1039	138
[Ni$_8$(OH)$_4$(H$_2$O)$_2$(L)$_6$]$_n$	Ni/L	B-290	100/180	2.4	336	377	138
Zr-fumarate	Zr/FA	B-290	90/150	2.4	336	664	141

Ligand codes: BTC – benzene-1,3,5-tricarboxylic acid; BDC – benzene-1,4-dicarboxylic acid; BPTC – biphenyl-3,3′,5,5′-tetracarboxylic acid; BTB – 1,3,5-tris(4-carboxyphenyl)benzene; DHBDC – 2,5-dihydroxy-1,4-benzenedicarboxylic acid; FA – fumaric acid; MIM – 2-methyl imidazole; IP – isophthalate; BPY – 4,4′-bipyridine; NDC – naphthalenedicarboxylic acid; and L – 1*H*-pyrazole-4-carboxylic acid. Spray-dryer codes: B-290 – B-290 Mini Spray Dryer (Büchi Labortechnik); SD-1000 – SD-1000 Spray Dryer (Tokyo Rikakikai); and AF-88 – AF-88 Laboratory Spray Dryer (AFIND Scientific Instrument Co. Ltd). "—" not specified.

spray-drying allows the encapsulation of guest molecules in the voids of the formed superstructures. Thus, it was possible to incorporate magnetic iron oxide nanoparticles inside the HKUST-1 hollow microbeads in order to apply the thus formed composite for the removal of fuel contaminants and to easily separate the MOF with a magnet afterwards.

The following study by Carne-Sanchez *et al.* in 2015[133] showed the possibility to use a spray-dryer to encapsulate MOFs, particularly water-sensitive HKUST-1, into a hydrophobic polymer matrix – polystyrene (PS) – to produce HKUST-1@PS composites with improved hydrolytic stability. The feed suspension was composed of the pre-synthesized HKUST-1

dispersed in DMF and a defined portion of PS dissolved in dichloromethane. It was then spray-dried at a feed rate of 4.5 mL min^{-1}, a flow rate of 336 mL min^{-1} and an inlet temperature of 130 °C. The resulting product yielded spherical composite microbeads with an average size of 3.6 ± 1.7 µm, exhibiting the XRD pattern expected for HKUST-1. The presence of the PS amorphous phase could be assumed by a broad hump on the diffractograms at 2θ = 15–25°, which increased in intensity with the PS content in the composite. Moreover, the total content of the polymer strongly impacted the textural properties as PS is not adsorptive towards nitrogen. Accordingly, N$_2$ physisorption measurements revealed a decrease in

S_{BET} from 1430 m^2 g^{-1} (pre-synthesized HKUST-1) to 97 m^2 g^{-1} (HKUST-1@PS composite with 33 wt% MOF). The optimal composition was found to be the one containing 63 wt% MOF, which yielded a S_{BET} of 1202 m^2 g^{-1}, thus preserving the textural properties of the initial MOF powder. Moreover, upon immersion in water overnight, the pre-synthesized HKUST-1 powder was completely degraded. At the same time, the MOF composite preserved its structural and textural integrity both upon immersion in water and upon exposure to humid conditions (80% RH) for one week.

An aqueous spray-drying synthesis of the Zn-imidazole ZIF-8 was done by Tanaka *et al.*[134] In a typical synthesis, an aqueous suspension containing Zn-acetate and 2-methylimidazole was spray-dried at T_{in} = 150 °C and a feed rate of 5 mL min^{-1}. These conditions yielded dense spherical particles with an average size of 3.9 μm as confirmed by SEM and TEM. However, the XRD results suggested the formation of an unknown phase different from that of the original ZIF-8. Moreover, the product poorly adsorbed nitrogen as revealed by N$_2$ sorption measurements. Notably, the authors observed the coordination of dissolved species and therefore the solution turning into a suspension right before spraying. The authors explained this phenomenon as due to the hindrance of crystallization created by acetic acid, a by-product originating from the Zn-precursor. The presence of the acid in the as-synthesized product was demonstrated by means of FTIR spectroscopy and TGA. Accordingly, during the spray-drying process, the as-released acetic acid caused a rearrangement of Zn-(2-methylimidazole) bonds, leading to the amorphization of the final product due to the incomplete coordination of the ligands around the metal. Interestingly, the presence of non-coordinated ligands was similarly evidenced by TGA. However, redispersing the spray-dried particles in an alcohol enabled the recrystallization and thus the formation of the targeted ZIF-8 framework. Interestingly, the size of the alcohol molecule influenced the size of the nanocrystals: specifically, the longer the carbon chain the larger the nanocrystals. However, the microbead size remained in the same range. Upon recrystallization, the product yielded an XRD pattern characteristic of ZIF-8 with a S_{BET} of 1440 m^2 g^{-1}, which is consistent with the results published elsewhere.[135] Surprisingly, once these ZIF-8 microbeads were redispersed in an alcoholic solution, they undergo a transition from dense to hollow superstructures. Hence, the recrystallization process is fed by gradually dissolving the amorphous by-product from the surface to the core of the microbeads.

Independently, Chaemchuen *et al.*[136] studied the spray-drying of ZIF-8 and its derivatives, the Co-based ZIF-67 and a bimetallic Zn/Co-ZIF. As they faced the same issues as Tanaka *et al.*,[134] they applied slightly different conditions for spray-drying, namely an inlet temperature T_{in} = 180 °C and a feed rate of 6.7 mL min^{-1}. The thus-prepared products were amorphous. Upon recrystallization in a MeOH solution and drying, they obtained ZIF-8, ZIF-67 and Zn/Co-ZIF microbeads with the ZIF topology as suggested by the matching XRD patterns. The textural properties studied by N$_2$ physisorption revealed a S_{BET} of 1634 m^2 g^{-1} for ZIF-8, 1861 m^2 g^{-1} for ZIF-67 and

1746 m^2 g^{-1} for Zn/Co-ZIF. The former is considerably higher as compared to the ZIF-8 microbeads produced by Tanaka *et al.*[134] *via* the same aqueous phase approach. However, this cannot be attributed not only to different spray-drying conditions, but also to a difference in starting concentrations of the ZIF-8 precursors. Last but not least, the spray-dryer machines used for the syntheses come from different manufacturers.

Two step, seed-mediated spray-drying method, dense structures

Mitsuka *et al.*[137] provided an example of a MOF synthesized in 2 consecutive steps. This includes the formation of MOF seeds accomplished by heating up the mixed precursors to a certain temperature (T_1) in a separate vessel, and further spray-drying the thus-formed suspension. Noteworthily, the first step initiates the formation of primary MOF nuclei and the second step, spray-drying, contributes to crystal growth. This approach is generally applied for MOFs consisting of high-nuclearity Secondary Building Units (SBUs), *i.e.*, of metal-clusters composed of multiple metal nuclei such as the UiO family. Following this method, the authors described the successful spray-drying of UiO-66, producing spherical superstructures. The XRD pattern showed reflections matching with the ones of the classical UiO-66 synthesized by the solvothermal method. There is, however, a slight peak-broadening observed in the case of the spherical beads. This was attributed to the decreased size (less than 100 nm) of the individual UiO-66 nano-particles forming the microbeads, compared to the 500 nm sized crystals obtained *via* the solvothermal approach (Fig. 16a). The presence of the typical UiO-66 chemical features was further proven by IR spectroscopy, revealing all bands characteristic of the UiO-66 framework. However, the N$_2$ physisorption performed on both samples indicated a decrease of about 30% in adsorbed N$_2$ for the spray-dried spherical microbeads. Therefore, some amorphous parts might remain. CID-1, which is a MOF with the formula Zn$_2$(ip)$_2$(bpy)$_2$, was also obtained (see Table 14).

Two step, continuous flow spray-drying method, dense structures

Garzon-Tovar *et al.*[138] also reported the spray-drying of a series of MOFs with high-nuclearity. To do so, they combined continuous flow and spray-drying methods (Fig. 16b and c). As in the case of Mitsuka *et al.*,[137] the former is beneficial to initiate the nucleation step, while the latter favors the crystal growth. Thus, the so-called spray-drying continuous flow-assisted synthesis was applied to produce spherical microbeads of UiO-66 and its derivatives.

In particular, they performed a full study on the production of UiO-66 spherical microbeads. First of all, they found that introducing a continuous flow reactor before the spray-dryer is a crucial step as the application of the spray-dryer alone yielded an amorphous product, as reported by Mitsuka *et al.*[137] Moreover, the sole use of a continuous flow reactor without the spray-dryer gave rise to the product with a low yield (12%) as well as poor textural properties (S_{BET} = 708 m^2 g^{-1}). Thus, the

Fig. 16 SEM image of the spray-dried UiO-66 (a) prepared by the seed-mediated spray-drying method.[137] Copyright 2016 The Chemical Society of Japan. Schematic representation of the spray-drying continuous flow-assisted method (b) and the corresponding photograph (c).[138] Copyright 2016 Royal Society of Chemistry. UiO-66 (d) prepared by the continuous flow spray-drying method.[138] Copyright 2016 Royal Society of Chemistry. UiO-66-NH$_2$ (e) prepared by the continuous flow spray-drying method.[141] Copyright 2018 Royal Society of Chemistry.

combination of both was required. The authors further showed that the optimal conditions for the synthesis of UiO-66 and its derivatives included an inlet temperature of 180 °C, a flow rate of 336 mL min^{-1} and a feed rate of 2.4 mL min^{-1}. The chosen inlet temperature corresponds to the minimum temperature required for the complete evaporation of the solvent, DMF. The UiO-66 microbeads produced under these conditions yielded dense spherical superstructures with an average size of 4.3 ± 2.6 μm composed of individual nanoparticle aggregates (Fig. 16d). XRD confirmed the presence of the UiO-66 structure. In terms of textural properties, the spray-dried microbeads exhibited pronounced porosity with a high S_{BET} of 1106 m^2 g^{-1}, which is in good agreement with that of UiO-66 produced by classical solvothermal methods (1150–1250 m^2 g^{-1}).[139,140]

Additionally, lower feed rates of 1.8 and 1.2 mL min^{-1} were attempted and consequently the authors observed clogging inside the flow reactor. Moreover, the products obtained under these conditions exhibited poor textural properties with S_{BET} of 667 and 687 m^2 g^{-1}, respectively. The authors attributed this phenomenon to the formation of UiO-66 mostly in the flow reactor before it reached the spray-dryer. Importantly, they concluded that the longer the residence time in the flow reactor the higher the content of the MOF formed within it, and therefore the lower the quality of the final product. This explains the lower textural properties of the UiO-66 beads synthesized by Mitsuka et al.[137] as in their case the initial feed solution was subjected to nucleation for 2 h. Another parameter to highlight is the temperature of the flow reactor, T_1. Garzon-Tovar et al.[138] initiated the nucleation at 115 °C for as long as 63 s (which corresponds to 2.4 mL min^{-1} flow rate) and outlined another important observation: a decrease in temperature in the flow reactor led to a decrease in S_{BET} as well as in the

yield of the product. Thus, upon applying 90 °C they obtained UiO-66 microbeads exhibiting a S_{BET} of 465 m^2 g^{-1}, which is comparable to the approximately 110 mL g^{-1} at STP (of adsorbed N$_2$) obtained by Mitsuka et al.[137] using the same nucleation temperature. Furthermore, Garzon-Tovar et al.[138] successfully expanded the spray-drying continuous flow-assisted synthesis to other members of the UiO-66 family as well as to other MOFs with high-nuclearity SBUs based on MIL-100(Fe) and Ni [Ni$_8$(OH)$_4$(H$_2$O)$_2$(L)$_6$]$_n$ (Table 14).

Avci-Camur et al.[141] continued exploiting the spray-drying technique for the synthesis of MOFs, targeting the UiO-66 family and more specifically UiO-66-NH$_2$ by the combined continuous-flow spray-drying method under aqueous conditions. For this purpose, the authors used water-soluble ZrOCl$_2$·8H$_2$O and 2-aminoterephthalic acid as the metal-precursor and the ligand, respectively. In this work specific stress was given to the use of a modulator, the acetic acid. Generally, the application of monotopic acids such as hydrochloric, formic and acetic acids facilitates the formation/crystallization of the UiO-family of MOFs.[142] Accordingly, it was shown that an increase in the acid concentration caused significant changes in textural properties. Thus, the UiO-66-NH$_2$ prepared with 14% acetic acid in the feed solution yielded microbeads with a S_{BET} of 840 m^2 g^{-1} when spray-dried at T_{coil} = 90 °C, T_{in} = 150 °C, flow rate = 336 mL min^{-1} and feed rate = 2.4 mL min^{-1}. However, at elevated (56%) concentrations of the acid, the S_{BET} significantly increased up to 1036 m^2 g^{-1} under the same operating conditions. It should be noted that a further increase (70%) in the acid content led to a partial loss in crystallinity viewed as a decrease in reflection intensities in the XRD pattern as well as a loss in S_{BET} down to 655 m^2 g^{-1}. This suggests a competition between the modulator and the

ligand for coordination with the metal clusters and therefore subsequent structural collapse upon exceeding occupation of the clusters by the modulator. The optimal acid concentration was found to be 30%. At this value, the spray-dried UiO-66-NH$_2$ yielded microbeads with a size distribution of 4–10 μm (Fig. 16e) and exhibiting the UiO-66 structure according to XRD results. Besides, the S_{BET} value, 1261 m^2 g^{-1}, lies in the range of non-functionalized UiO-66 made *via* the solvothermal route with DMF, and is much higher than that of the spray-dried UiO-66-NH$_2$ prepared by Garzon-Tovar *et al.* (S_{BET} = 752 m^2 g^{-1}).[138] Finally, the same protocol was applied to the Zr-fumarate MOF. The corresponding information is given in Table 14.

A further study done by Boix *et al.*[143] in Maspoch's group led to the incorporation of inorganic nanoparticles into UiO-66 microbeads. The process followed the same sequence of steps, including the formation of primary nuclei in the flow reactor at 115 °C with a feed rate of 2.4 mL min^{-1}, an inlet temperature of 180 °C, and a flow rate of 336 mL min^{-1}. The thus-formed UiO-66 microbeads exhibited an average size of 1.5 ± 1.0 μm with a crystalline framework corresponding to the UiO-66. Additionally, the beads had a high surface area (S_{BET} = 945 m^2 g^{-1}), which was slightly below than the one obtained by Garzon-Tovar *et al.* (S_{BET} = 1106 m^2 g^{-1})[138] following the same method. The difference might be attributed to the Zr-source used in each case: zirconium propoxide and zirconium tetrachloride, respectively. Interestingly, the UiO-66 itself was shown to be active towards the adsorption of toxic heavy metals such as Cr(VI) and As(V) with removal efficiencies of 99 and 45%, respectively. However, once functionalized with thiol (–SH) groups and doped with CeO$_2$ nanoparticles, it became active and efficient towards heavier metal species including Cd(II), Cu(II), Pb(II) and Hg(II) with removal efficiencies of 87, 99, 99 and 98%, respectively. Importantly, CeO$_2$-doped UiO-66-(SH)$_2$ microbeads retained their removal efficiency after 10 adsorption/desorption cycles in a continuous flow column, making them appropriate for further developments as water-purifying adsorbents.

Recently, Boix *et al.*[144] extended their study and incorporated CeO$_2$ doped UiO-66 microbeads made *via* spray drying into millimeter-scale porous polyethersulfone (PES). This was achieved by a dropwise addition of a suspension containing CeO$_2$@UiO-66 microspheres and dissolved PES in DMF into a precooled water/ethanolic solution. As a result, PES precipitated, forming a hard shell around the droplets and therefore yielding CeO$_2$@UiO-66@PES granules with an average size of 2 mm. The thus-formed granules with 26% microbead loading showed a 61% removal efficiency of an As(III) and As(V) mixture as well as removal efficiencies of 75% Hg(II) and 72% Pb(II), to name a few. This makes the CeO$_2$@UiO-66@PES granules an excellent adsorbent for purifying drinking water from heavy metal pollutants with the potential to be used in the cartridges of home water-filter pitchers.

As a concluding remark, it should be noted that spray-drying, initially intended for drying powdery materials, can be used as a direct synthesis and shaping technique for MOFs. It enables the formation of spherical microbeads with an average size of up to ten micrometers. The microbead size depends on the spray-drying conditions, and mainly on the size of the sprayed droplets at the exit of the nozzle. Generally, this technique allows obtaining highly crystalline MOF microbeads with textural and morphological properties depending on the process conditions and especially the temperature, feed rate and gas flow. Besides, MOFs based on high-nuclearity metal clusters (UiO-66, MIL-100(Fe)) tend to form dense structures, while MOFs with low-nuclearity metal clusters (HKUST-1, ZIF-8) generally form hollow structures. Furthermore, the productivity of the MOF spray-drying process might be improved by implementing a continuous flow of the reaction mixture, with possible space-time yields (STY) of ∼20 kg m^{-3} d^{-1}.[138]

Phase separation methods

Apart from the shaping techniques considered above, there are other approaches enabling obtaining MOFs with various shapes. In particular and as its name suggests, phase separation relies on using two phases: one containing the MOF, and the other either immiscible or at least with tunable miscibility.

Beads

One specific phase separation process, sometimes referred to as "molecular gastronomy", relies on using hydrocolloids such as alginate, cellulose, chitosan, starch and other biopolymers together with cross-linking agents: typically, group II metal ions or bases. Generally, when a cross-linking agent comes in contact with an aqueous slurry of a biopolymer and the pristine MOF, it precipitates the biopolymer which entraps the MOF particles and serves as the matrix (Fig. 17a). This approach was first described by Spjelkavik *et al.*[145] who formulated Ni-based CPO-27 into spherical beads of a few millimeters. More precisely, they used either a solution of CaCl$_2$ or BaCl$_2$ as the cross-linking agent, which was added dropwise into an aqueous CPO-27/alginate slurry. Eventually, after a certain time, the spheres were isolated, washed and dried to yield beads with MOF contents up to 90 wt%. Besides, the authors found that the crystal structure remained intact by the end of this procedure. In addition, they outlined the importance of the gelation (residence) time. Thus, the longer the gelation time, the more drastic the loss in surface area for the final beads. Therefore, the authors suggested 0.5 h to be a fair compromise between rigidifying the objects and maintaining the accessibility to the pores of CPO-27.

Lee *et al.*[146] systematically studied the shaping of UiO-66 into spherical beads by the "alginate" method. Namely, they addressed the impact of different parameters such as the MOF content, gelation time, and activation temperature on the properties of the final beads. Thus, they found that the alginate had no effect on the crystal structure of the MOF. Besides, the loss in specific surface area upon shaping was within the expected range and consistent with the alginate content. Thus, for the beads with polymer contents of 2.4 and 4.8 wt%, the

Fig. 17 Schematic representation of the "molecular gastronomy" method (a). UiO-66 beads (b–f) prepared by Lee et al.[146] showing the effect of the concentration of the gelation solution on the final shape of the beads: b – 0.2% (w/v); c – 0.5% (w/v); d – 2.0% (w/v); and e and f – 10% (w/v). Copyright 2020 Elsevier. Preparation of MIL-125(Ti) beads (g) with chitosan as a binding biopolymer.[149] Copyright 2018 MDPI.

decreases in S_{BET} were 4.0 and 6.5%, respectively, relative to the parent UiO-66 with a S_{BET} of 1241 m^2 g^{-1}. Interestingly, it was shown under these conditions that the gelation time had no significant impact on the textural properties as the beads with 3 min and 14 h of gelation yielded comparable N_2 isotherms. Moreover, the final shape of the beads was dictated by the concentration of $CaCl_2$ in the gelation solution (Fig. 17b–f). Importantly, the optimal activation temperature was found to be in the range of 120–135 °C to avoid the biopolymer degradation.

Farrusseng et al.[147] studied the shaping of the Al(OH)-fumarate MOF for the heat-pump application. They found that the "alginate" method had little effect on the MOF textural properties, leading to losses in specific surface area comparable to the initial alginate content, as reported by Lee et al. As an example, beads with ~12 wt% alginate demonstrated a 10% reduction of S_{BET} as compared to the pristine MOF (997 vs. 1098 m^2 g^{-1}). Consequently, the water sorption capacity of the MOF-based beads was reduced by the same extent, suggesting no pore blocking caused by the polymer. Importantly, the alginate content in the beads also had no significant impact on mass and heat transfers.

Yang et al.[148] modified the "alginate" method by adding an extra cross-linker agent: polyacrylic acid (PAA). Interestingly, this polymer presents a large molecular weight and rapidly polymerizes, limiting the polymer's ability to diffuse into the

MOF's porosity. This procedure was applied to numerous MOFs, including MIL-127(Fe), MIL-101(Cr), HKUST-1, UiO-66, ZIF-8, and Fe-BTC. All beads presented MOF loadings higher than 84.9 wt% and almost preserved BET surface areas (normalized by the MOF loading), except for HKUST-1, which partially collapsed due to its exposure to strongly acidic conditions (pH = 2.7). SEM-EDX analysis on the cross-section of a bead concluded that the MOF crystals were homogeneously distributed. Computational modeling was performed to unveil the chemical interactions between alginate, PAA, and Ca^{2+}. Spontaneous binding of carboxyl and/or hydroxyl groups to Ca^{2+} was observed. Moreover, ab initio simulations between MIL-127(Fe), a representative MOF, and both polymers unveiled that Ca^{2+} would bind to the free carboxylic groups of the ligands on the surfaces of the MOFs and the polymers, while polar carboxyl and hydroxyl groups of PAA and alginate would bind to the metal sites of MIL-127(Fe). This was experimentally verified by FT-IR and Raman spectroscopies. According to the authors, improved mechanical stability of the composite beads should be obtained, but it was not measured.

Finally, Yang et al.[148] prepared polydopamine-grafted Fe-BTC-based beads for the extraction of lead from Rhône river water (600 ppb). Under continuous flow, one gram of beads could reduce the concentration of 10.8 liters of water below the EPA limit of 15 ppb. Of note, most commercial adsorbents were poorly performing below 150 ppb due to the presence of

competitive ions. Thus, the authors concluded that the composite beads were selective for Pb^{2+} over less toxic ions. Moreover, they could be readily regenerated in the presence of EDTA.

Liang et al.[149] studied the shaping of a Ti-based MIL-125 MOF with chitosan as a binding biopolymer into spherical beads. They first mixed chitosan and an $FeCl_3$ solution, followed by the addition of the MOF. Once well mixed, a 3% $Na_5P_3O_{10}$ solution was added dropwise to initiate the crosslinking step (Fig. 17g). The thus-formed beads were recovered, washed and dried. The authors showed that such a formulation had no impact on the crystal structure nor the framework composition as confirmed by XRD, FTIR spectroscopy and XPS analyses. Therefore, the beads exhibited a consequent capacity for the removal of Pb(II) species, with only an $\sim$12% decrease in efficiency (from 100 to 88 mg g^{-1}) after five consecutive cycles.

Chitosan was also used by Omer et al.[150] to produce magnetic ZIF-67 beads with a diameter of 1.65 mm. For that, they dispersed the as-made ZIF-67 crystallites and Fe_3O_4 nanoparticles in water under sonication. The suspension was then mixed into a solution of chitosan dissolved in acetic acid, and the resulting mixture was added dropwise into NaOH solution, and aged for 15 minutes prior to the recovery of the beads using a magnet. The FT-IR spectrum of the beads revealed broad bands at 1062 and 3441 cm^{-1}, attributed to the stretching vibration of C–N and O–H from chitosan, respectively. The presence of Fe_3O_4 and ZIF-67 was also attested to by broad bands at 557 and 1405 cm^{-1} (Fe–O stretching), and 413 cm^{-1} (Co–N stretching), respectively. A soft-ferromagnetic behavior was observed using a vibrating sample magnetometer, while a significant decrease in the saturation magnetization was observed and attributed to the presence of non-magnetic ZIF-67 and chitosan. SEM images and digital micrographs showed that the beads were irregular and presented a core–shell structure, with ZIF-67 particles mostly located at the core. A type IV isotherm was measured by N_2 physisorption, with an H4 hysteresis loop typically characterizing the presence of mesopores. The BET surface area of such composite beads reached 221 m^2 g^{-1}: for comparison, ZIF-67 powders generally present BET surface areas above 1100 m^2 g^{-1}. Hence, partial pore blockage by the chitosan was suspected. Nonetheless, the composite beads presented a higher Cr(VI) adsorption capacity (71 mg g^{-1}) than the MOF itself (45 mg g^{-1}). The composite beads' reusability was evaluated and, after the seventh cycle, the capacity of the beads only decreased from 71 to 61 mg g^{-1}. XPS spectroscopy was performed to propose an adsorption mechanism in three steps: 1 – protonation of the amino groups of the chitosan and coulombic interaction between the positively charged beads and the anionic Cr(VI); 2 – reduction of Cr(VI) to Cr(III) by the electron-donor groups; and 3 – formation of coordinate–covalent bonds between Cr(III) and the composite beads.

Besides biopolymers, other types of polymers can lead to the formation of beads. For instance, HKUST-1-polyacrylonitrile (PAN) composite beads were formed by Riley et al.,[151] by adding dropwise a DMSO mixture containing dissolved PAN and dispersed HKUST-1 crystallites into an aqueous solution. The MOF loading was varied from 10 to 90 wt% (on a dry basis). The final beads presented a size distribution of 3.17 $\pm$ 0.26 mm, and the MOF crystals were evenly distributed within the beads. X-ray computed tomography and SEM on cross-sectioned beads revealed the presence of 0.5–1 μm macropores homogeneously distributed. Thus, PAN allowed obtaining hierarchically porous beads following phase separation. The maximal compressive strength of 90 wt% HKUST-1 beads reached 18 MPa. Finally, the beads were used for xenon capture, comparatively to the powder. The 90 wt% HKUST-1 beads presented a capacity 30% lower than that of the powder, which might be due to partial pore blockage by the PAN. Finally, the beads were gamma irradiated up to 100 kGy and the MOF retained most of its crystallinity, making it an interesting candidate for further demonstration tests.

Park et al.[152] shaped a diamine-functionalized epn-Mg_2(dobpdc) MOF (dobpdc = 4,4'-dioxido-3,3'-biphenyldicarboxylate, epn = 1-ethylpropane-1,3-diamine) into beads using poly(vinylidene fluoride) (PVDF). For this, the pristine MOF powder was dispersed in a DMF solution containing the polymer dissolved. Then, the slurry was added dropwise through a syringe into a water/ethanol (5 : 1, v/v) mixture. Spherical beads of a few millimeters were rapidly formed and subsequently recovered, washed with MeOH and dried. Thereafter, the beads were immersed in an epn solution in toluene to graft the diamine precursor onto the MOF. Upon this multi-step process, the structural integrity of the MOF crystals was preserved as observed by XRD. The beads containing 60 wt% MOF showed a CO_2 adsorption capacity of 1.48 mmol g^{-1} at 1000 ppm and 25 °C, as compared to 2.49 mmol g^{-1} for the pristine MOF functionalized with epn. This value agrees with the polymer content in the beads and represents a 41% loss. Moreover, the beads demonstrated fair stability towards CO_2 adsorption under humid conditions (60% RH), losing only 22% of their efficiency after regeneration at 70 °C for 1 h, and outperforming the powder counterpart, which lost 72% of its capacity after regeneration. This highlights an enhanced stability of the composites under humid conditions due to the presence of the hydrophobic polymer.

Another type of phase separation technique relies on the use of freezing solvents. Gökpinar et al.[153] studied the freeze-granulation of a series of MOFs: two Zr-based (UiO-66 and Zr-fumarate) and two Al-based (MIL-160 and Al-fumarate). In any case, the parent MOF powder was mixed with the PVA binder pre-dissolved in water (80 wt% MOF dry content). The thus-formed suspension was further added dropwise through a syringe into liquid nitrogen. The pellets were collected and dried after solvent-exchange. This procedure enabled spherical MOF/PVA beads and had no impact on the crystal structure as well as on textural properties. Thus, MOF/PVA spheres retained 74–99% of the MOF original surface area (with respect to the MOF content). Besides, the beads exhibited macropores of a few microns. Importantly, there was a slight increase in water uptake shown by the Zr-based MOFs upon shaping (113% for Zr-fumarate/PVA and 103% for UiO-66/PVA beads). This was

attributed to the generation of new defect sites upon freeze-granulation.

Monoliths

While phase separation is mostly applied to prepare MOF-based composite beads, monoliths can also be obtained using similar approaches. In particular, Hasturk et al.[154] shaped Al-fumarate and Cr-based MIL-100 into mechanically stable monoliths. For this, they first dissolved some PVA in water, prior to the addition of the MOF powder. Further acetone was added dropwise to the MOF/PVA suspension, and the thus-formed two phase mixture was left still for 48 h until complete separation. During this period, acetone gradually penetrated the polymer-enriched phase and initiated its gelation. Eventually, it was washed with fresh acetone and dried in a vacuum at room temperature, thus yielding monoliths with up to 80 wt% MOF. This procedure was shown to have no effect on the crystal structure nor on the textural properties.

Following spinodal decomposition, which is also a phase separation method, Hara et al.[155] prepared UiO-66_NH$_2$-based monolithic materials with a trimodal pore structure. For that, all MOF precursors were dissolved into DMF along with poly(propylene glycol) (PPG) at 60 °C, and the clear solution was sealed in a hydrophobic glass tube kept at 80 °C. After 12 hours, hydrophilic UiO-66_NH$_2$ MOF mismatched growth occurred, as well as phase separation with the hydrophobic PPG. After washing with solvent, PPG was evacuated from the monolithic solid, leading to the formation of macropores whose diameter, between 0.9 and 1.8 μm, can be controlled by the amount of PPG. The XRD patterns displayed a few broad reflections, with 2θ positions comparable to those of the simulated UiO-66. The structural properties of the MOF were proven by FT-IR spectroscopy, yielding a spectrum comparable to that of standard UiO-66_NH$_2$ powder. All samples presented specific surface areas between 712 and 749 m^2 g^{-1}, further underlining the presence of a microporous network, while interparticular mesoporosity could also be deduced from N$_2$ sorption isotherms at higher relative pressure. Indeed, the TEM images showed particles with sizes below 50 nm. Uniaxial compression tests demonstrated that these monoliths presented a maximal compressive strength of 2.5 MPa. Interestingly, the authors showed that addition of acetic acid, a known modulator accelerating the crystallization, allowed obtaining larger mesopores. Alternatively, a post-shaping solvothermal treatment also allowed controlling the final size of the mesopores following the secondary growth of the MOF crystals.

In 2014 Ahmed et al.[156] proposed a different method for MOF shaping based on controlled freezing. According to it, a MOF powder in suspension can be shaped into monoliths upon controlled freezing of the solvent with its subsequent elimination via freeze-drying. The authors applied this methodology to obtain Cu-based HKUST-1 monoliths. For this, the MOF precursors were dissolved in DMSO and left for 24 h at 80 °C. After that, the solution was frozen in liquid nitrogen for 1 min and placed into a freeze-dryer to sublime the solvent. This procedure yielded highly crystalline HKUST-1 monoliths as

confirmed by XRD. Moreover, the specific surface area was 870 m^2 g^{-1} with characteristics of both micropores and meso-pores, as visible from the N$_2$ physisorption isotherms. Additionally, as shown by Hg intrusion, the monoliths exhibited macropores with diameters around 0.4 and 10 μm. Importantly, these macropores generated upon ice-templating were oriented in one particular direction due to the orientational growth of ice crystals during freezing. Lastly, the authors showed that the size of these macropores could be varied by altering the freezing temperature. Thus, upon freezing at 5 °C the macro-pores were two times bigger (∼50 μm) than the macropores generated upon freezing at −80 and −20 °C (32 and 25 μm, respectively).

Fu et al.[157] studied the preparation of ice-templated composite monoliths based on UiO-66 MOF and chitosan for waste-water treatment. In a typical procedure, the parent UiO-66 was added into a solution containing pre-dissolved chitosan with 1:1 and 1:2 weight ratios. After that, part of the suspension was immersed in liquid nitrogen for 5 min followed by freeze-drying for 48 h. The results suggest that the thus-formed monoliths preserved the crystal structure of the parent UiO-66, with a surface area in accordance with the MOF ratio (339 m^2 g^{-1} for the UiO-66/chitosan composite with a 1:2 weight ratio, as compared to a S_{BET} of 1034 m^2 g^{-1} for the parent UiO-66). However, the monoliths were stated to undergo disintegration upon immersion in an aqueous solution of methylchlorophenoxypropionic acid (a toxic pesticide). This was attributed to the presence of residual acetic acid used in the preparation step. Therefore, the monoliths were washed with NaOH solution to remove the acid and overcome the disintegration. Interestingly, the results indicated a pesticide removal capacity of the UiO-66/chitosan (1:2) composite as high as that of the parent UiO-66 (34 and 36 mg g^{-1}, respectively). This is due to the contribution of the chitosan, which also presented a consequent pesticide removal capacity (27 mg g^{-1}).

Other studies by Fu et al.[158,159] include the further pyrolysis of ice-templated MOF/polymers composites to produce hier-archically porous carbon materials. Thus, they formed carbon/ZrO$_2$ composites upon the carbonization of ice-templated UiO-66/poly(4-styrenesulfonate) composites at 800 °C under Ar.[159] Although a drastic loss in surface area was observed upon pyrolysis (368 m^2 g^{-1} vs. 1034 m^2 g^{-1} for the parent UiO-66), the newly-formed material presented an interesting hierarchi-cal porosity composed of micropores inherited from the MOF, mesopores generated due to interparticular voids, and macro-pores generated by the ice-templating process. Moreover, metal oxide-free porous carbons were obtained by replacing UiO-66 with ZIF-8, and subsequently carbonizing ice-templated ZIF-8/polyacrylonitrile (PAN) monoliths at 1000 °C under Ar. The textural properties of the thus-formed monoliths were also described by micro-meso-macroporous features, with a S_{BET} of 530 m^2 g^{-1}.

Tian et al.[160] showed the possibility to form ZIF-8 monoliths without using binders nor high pressures. For this, they immersed a newly-formed ZIF-8 powder into an ethanolic solution containing dissolved precursors (Zn-nitrate and

methylimidazole), and the solid product was recovered *via* centrifugation. The authors outlined the importance of drying the solid at room temperature so that it retained its monolithic shape. Besides, when extra amounts of precursors were added, mechanically stable monoliths were formed due to the extension of polymerization reactions. The mechanical resistance was assessed by measuring the elastic modulus (7 GPa) and hardness (0.6 GPa) by nanoindentation. The thus-formed monoliths retained the original crystal structure of ZIF-8 as well as high specific surface area, up to 1395 $m^2\ g^{-1}$.

To conclude, there is a plethora of studies which show the possibility to produce robust MOF objects using (bio)polymers as the cross-linking/binding agents as well as through sublimation or phase transition phenomena. These so-called "phase separation" methods enable the shaping of MOF powders into differently objects – mostly beads or monoliths – without using specific equipment; with the exception being freeze-drying for which, as its name suggests, a freeze-dryer is needed. Interestingly, the final produced MOF composites present high BET surface areas, in line with their weight composition, as well as good mechanical stability.

Conclusion and perspectives

The outstanding properties of Metal–Organic Frameworks rapidly grabbed the interest of both academics and industrialists, and an abundant body of literature covering all related aspects is available nowadays. On the specific aspect of shaping, since the late 2000s an increasing number of articles can be found, first based on unidirectional compression which is the most straightforward technology for shaping powders, then on other classical technologies (extrusion, granulation). Nowadays, all available techniques can be employed to shape MOF-based materials, each with specific strengths and weaknesses that have been underlined in this review.

Pelletization has been regarded for long as the "reference" technology for comparing shaping techniques. Obviously, when applying forces in the range of the ones applied industrially to zeolites and activated carbons, the MOF structures typically collapse which directly impact their final performances. However, recent developments show that when applying mild compression, along with the presence of a scaffolding compound (solvent or other), the collapsing is greatly limited. Moreover, binderless pelletization is possible owing to MOF crystals' binding ability. Therefore, pelletization offers some of the best compromises between mechanical stability, and volumetric and gravimetric uptakes, making it a leading technique for mobility applications. To further limit the effect of compression on MOFs while reaching high mechanical resistance, isostatic compression could be advantageously used.

Extrusion is another classical technique which is especially used to produce extrudates and honeycombs for catalytic converters. When it is applied to MOFs, limited impact on the structural and textural properties can be observed for most MOFs, due to lower pressures and shear forces applied.

Extrusion requires, however, finely controlling the formulation and related rheological properties of the extruded paste. Advantageously, extrusion can also be used for the direct preparation of MOF objects starting from precursors (reactive extrusion). The latter is of particular interest as it allows limiting or avoiding completely the toxic solvents traditionally used for the synthesis of MOF powders. At the same time, reactive extrusion implies a continuous process with high potential space time yields. While this approach might not be applicable to all MOF structures, the reactive extrusion presents several advantages over more conventional methods such as solvo/hydrothermal or microwave-assisted syntheses of MOFs. On the other hand, these conventional methods remain better in terms of obtained crystallinity and surface area for most MOF structures.

Since 2013, another technique for both forming and shaping MOFs has become popular. Based on the principle of spray-drying, which is the pulverization of a suspension in a heated environment for fast drying, microbeads of calibrated diameters can be obtained starting from precursors. Herein, the fast reaction rates within the nanodroplets of suspensions, acting like nanoreactors, allow obtaining highly crystalline MOF particles which agglomerate into hollow or dense fluidized powder.

Granulation is the last industrially-mature technology reviewed herein, and allows producing millimeter-sized grains. Two types of granulation techniques are typically discussed: wet granulation, when powders are aggregated in a high-shear rate mixer in the presence of a solvent; and dry granulation, when grains are obtained from a previously shaped object either mildly crushed and sieved, or spheronized. Due to higher stresses applied, the dry granulation implies more severe losses in the initial physicochemical properties of the MOFs, while the wet granulation has a less pronounced effect and therefore might be more adequate. Especially, replacing water with another solvent with a lower surface tension is highly beneficial.

Starting from 2015, the additive fabrication techniques, also called 3D printing, have been widely applied to a large selection of MOF structures to produce precisely designed objects. Among the various technologies available, SLS and DLP might not be the most adequate as, contrarily to ceramics and metals, MOFs cannot handle high temperatures and therefore are partially decomposed under laser irradiation. Moreover, the photopolymerizable resins used in DLP cannot be eliminated by thermal decomposition, thus blocking the porosity and largely affecting the performances of the MOFs. Therefore DIW, which can be viewed as the three-dimensional extrusion of a shear-thinning MOF-based paste, has been largely adopted. Highly interesting results have been obtained in terms of gravimetric uptake and mechanical stability, and therefore this technology is promising for atypical applications necessitating unconventional shapes. These advances should be consolidated with the development of new setups with increased printing accuracy, smaller nozzle diameter and improved paste/ink formulations.

Table 15 Comparison between some of the shaping techniques on their performance and main characteristics

Technique	Specifics	Advantages	Disadvantages	Use of binders	Use of plasticizers/solvents	Impact on textural properties	Impact on mechanical properties
Pelletization	High pressure applied uniaxially	Ease, cost and accessibility	Marked amorphization above a threshold of pressure (MOF-dependent)	Possible, not required	Not required	Pore destruction due to applied pressure	Considerable reinforcement
Granulation	Shearing forces used for coagulation	Good sphericity and fair control over the size	Non-uniform size distribution, sieving step needed	Mostly required	Required	Pore blocking due to binders	Reinforcement
Extrusion	Paste pushed through a die	Continuous process, large choice of shapes, reactive extrusion possible	Difficult to control the paste rheology	Required	Required	Pore blocking due to binders	Reinforcement
3D printing	Space-controlled deposition of a paste	High control over the final shape and size	Difficult to control the paste rheology, no commercial setup	Required	Required	Pore blocking due to binders	Reinforcement
Spray-drying	Instantaneous evaporation of a suspension or a solution	Continuous process, one-step synthesis and shaping possible	Heat expense, product quality sensitive to the operating conditions	Not required	Not required	None	None

Finally, other less-popular techniques have been successfully applied for shaping MOFs, among which have been reviewed the so-called molecular gastronomy, ice-templating (also called freeze-casting), and phase separation (also called spinodal decomposition). These three techniques presented very low impact on the physicochemical properties of the MOFs applied and are therefore worth investigating more in detail. It should be noted, however, that ice-templating and phase separation both involve the creation of a second level of porosity macrosized (>50 nm) following the replication of ice crystals and polymers, respectively.

In order to better understand the failing mechanisms and improve the resistance of the final objects produced while not sacrificing the physicochemical properties brought about by the MOFs, the modeling of the porous microstructure would be highly beneficial. Modeling software packages based on either finite elements or discrete elements, and coupled with X-ray tomography observations and different mechanical characterization studies such as micro-indentation, have been applied to porous catalysts and could be advantageously used as well on these objects.

While keeping in mind the final application, for energy storage, fixed bed reactors, or toxic gas masks just to name a few, specific shaping methods have been developed and most prerequisites can be met nowadays in order to bring MOFs to the forefront of highly performing materials. However, to be durably implemented, besides cutting down their cost and carefully evaluating their environmental and health impacts, efforts are still needed to reach or even exceed the mechanical resistance of inorganic-based objects. This would ensure industrial acceptance, the way zeolites were broadly introduced in refining and petrochemical processes in the last century.

Lastly, comparative data on the specifics and general performance of the conventional shaping techniques are given in Table 15.

Conflicts of interest

There are no conflicts to declare.

References

1 O. M. Yaghi and H. Li, Hydrothermal Synthesis of a Metal–Organic Framework Containing Large Rectangular Channels, *J. Am. Chem. Soc.*, 1995, **117**, 10401–10402, DOI: 10.1021/ja00146a033.

2 O. M. Yaghi, M. O'Keefe, N. W. Ockwig, H. K. Chae, M. Eddaoudi and J. Kim, Reticular synthesis and the design of new materials, *Nature*, 2003, **423**, 705–714, DOI: 10.1038/nature01650.

3 S. S.-Y. Chui, S. M.-F. Lo, J. P. H. Charmant, A. G. Orpen and I. D. Williams, A Chemically Functionalizable Nanoporous Material [Cu₃(TMA)₂(H₂O)₃]n, *Science*, 1999, **283**, 1148–1151, DOI: 10.1126/science.283.5405.1148.

4 J. H. Cavka, S. Jakobsen, U. Olsbye, N. Guillou, C. Lamberti, S. Bordiga and K. P. Lillerud, A New Zirconium Inorganic Building Brick Forming Metal Organic Frameworks with Exceptional Stability, *J. Am. Chem. Soc.*, 2008, **130**, 13850–13851, DOI: 10.1021/ja8057953.

5 J. Y. Choi, R. Huang, F. J. Uribe-romo, H. K. Chae, K. S. Park, Z. Ni, A. P. Co, M. O. Keeffe and O. M. Yaghi, Exceptional chemical and thermal stability of zeolitic imidazolate frameworks, *Proc. Natl. Acad. Sci. U. S. A.*, 2006, **103**, 10186–10191, DOI: 10.1073/pnas.0602439103.

6 G. Férey, C. Mellot-Draznieks, C. Serre, F. Millange, J. Dutour, S. Surblé and I. Margiolaki, A Chromium Terephthalate-Based Solid with Unusually Large Pore Volumes and Surface Area, *Science*, 2005, **309**, 2040–2042, DOI: 10.1126/science.1116275.

7 Z. R. Herm, R. Krishna and J. R. Long, CO_2/CH_4, CH_4/H_2 and $CO_2/CH_4/H_2$ separations at high pressures using Mg_2(dobdc), *Microporous Mesoporous Mater.*, 2012, **151**, 481–487, DOI: 10.1016/j.micromeso.2011.09.004.

8 A. Dhakshinamoorthy, Z. Li and H. Garcia, Catalysis and photocatalysis by metal organic frameworks, *Chem. Soc. Rev.*, 2018, **47**, 8134–8172, DOI: 10.1039/C8CS00256H.

9 L. Wang, M. Zheng and Z. Xie, Nanoscale metal–organic frameworks for drug delivery: a conventional platform with new promise, *J. Mater. Chem. B*, 2018, **6**, 707–717, DOI: 10.1039/C7TB02970E.

10 X. Fang, B. Zong and S. Mao, Metal–Organic Framework-Based Sensors for Environmental Contaminant Sensing, *Nano-Micro Lett.*, 2018, **10**, 64, DOI: 10.1007/s40820-018-0218-0.

11 M. Mon, R. Bruno, J. Ferrando-Soria, D. Armentano and E. Pardo, Metal–organic framework technologies for water remediation: towards a sustainable ecosystem, *J. Mater. Chem. A*, 2018, **6**, 4912–4947, DOI: 10.1039/C8TA00264A.

12 Y. Zhao, Z. Song, X. Li, Q. Sun, N. Cheng, S. Lawes and X. Sun, Metal organic frameworks for energy storage and conversion, *Energy Storage Mater.*, 2016, **2**, 35–62, DOI: 10.1016/j.ensm.2015.11.005.

13 Y. V. Kaneti, J. Tang, R. R. Salunkhe, X. Jiang, A. Yu, K. C. Wu and Y. Yamauchi, Nanoarchitectured Design of Porous Materials and Nanocomposites from Metal–Organic Frameworks, *Adv. Mater.*, 2017, **29**, 1604898, DOI: 10.1002/adma.201604898.

14 Q. Wang and D. Astruc, State of the Art and Prospects in Metal−Organic Framework (MOF) – Based and MOF-Derived Nanocatalysis, *Chem. Rev.*, 2020, **120**, 1438–1511, DOI: 10.1021/acs.chemrev.9b00223.

15 R. R. Salunkhe, Y. V. Kaneti and Y. Yamauchi, Metal−Organic Framework-Derived Nanoporous Metal Oxides toward Supercapacitor Applications: Progress and Prospects, *ACS Nano*, 2017, **11**, 5293–5308, DOI: 10.1021/acsnano.7b02796.

16 M. Zhong, L. Kong, N. Li, Y. Liu, J. Zhu and X. Bu, Synthesis of MOF-derived nanostructures and their applications as anodes in lithium and sodium ion batteries, *Coord. Chem. Rev.*, 2019, **388**, 172–201, DOI: 10.1016/j.ccr.2019.02.029.

17 C. Wang, Y. V. Kaneti, Y. Bando, J. Lin, C. Liu, J. Li and Y. Yamauchi, Metal–organic framework-derived one-dimensional porous or hollow carbon-based nanofibers for energy storage and conversion, *Mater. Horiz.*, 2018, **5**, 394–407, DOI: 10.1039/C8MH00133B.

18 C. Perego and P. Villa, Catalyst preparation methods, *Catal. Today*, 1997, **34**, 281–305, DOI: 10.1016/S0920-5861(96)00055-7.

19 F. Lorignon, A. Gossard and M. Carboni, Hierarchically porous monolithic MOFs: An ongoing challenge for industrial-scale effluent treatment, *Chem. Eng. J.*, 2020, **393**, 124765, DOI: 10.1016/j.cej.2020.124765.

20 R. Bingre, B. Louis and P. Nguyen, An Overview on Zeolite Shaping Technology and Solutions to Overcome Diffusion Limitations, *Catalysts*, 2018, **8**, 163, DOI: 10.3390/catal8040163.

21 R. V. Jasra, B. Tyagi, Y. M. Badheka, V. N. Choudary and T. S. G. Bhat, Effect of Clay Binder on Sorption and Catalytic Properties of Zeolite Pellets, *Ind. Eng. Chem. Res.*, 2003, **42**, 3263–3272, DOI: 10.1021/ie010953l.

22 G. T. Whiting, A. D. Chowdhury, R. Oord, P. Paalanen and B. M. Weckhuysen, The curious case of zeolite – clay/binder interactions and their consequences for catalyst preparation, *Faraday Discuss*, 2016, **188**, 369–386, DOI: 10.1039/c5fd00200a.

23 V. Finsy, L. Ma, L. Alaerts, D. E. De Vos, G. V. Baron and J. F. M. Denayer, Separation of CO_2 / CH_4 mixtures with the MIL-53 (Al) metal–organic framework, *Microporous Mesoporous Mater.*, 2009, **120**, 221–227, DOI: 10.1016/j.micromeso.2008.11.007.

24 V. Finsy, H. Verelst, L. Alaerts, D. E. De Vos, P. A. Jacobs, G. V. Baron and J. F. M. Denayer, Pore-Filling-Dependent Selectivity Effects in the Vapor-Phase Separation of Xylene Isomers on the Metal−Organic Framework MIL-47, *J. Am. Chem. Soc.*, 2008, **130**, 7110–7118, DOI: 10.1021/ja800686c.

25 J. Alcañiz-Monge, G. Trautwein, M. Pérez-Cadenas and M. C. Román-Martínez, Effects of compression on the textural properties of porous solids, *Microporous Mesoporous Mater.*, 2009, **126**, 291–301, DOI: 10.1016/j.micromeso.2009.06.020.

26 Y. H. Hu and L. Zhang, Amorphization of metal–organic framework MOF-5 at unusually low applied pressure, *Phys. Rev. B: Condens. Matter Mater. Phys.*, 2010, **81**, 174103, DOI: 10.1103/PhysRevB.81.174103.

27 Z. Jia, H. Li, Z. Yu, P. Wang and X. Fan, Densification of MOF-5 synthesized at ambient temperature for methane adsorption, *Mater. Lett.*, 2011, **65**, 2445–2447, DOI: 10.1016/j.matlet.2011.04.099.

28 J. J. Purewal, D. Liu, J. Yang, A. Sudik, D. J. Siegel, S. Maurer and U. Mu, Increased volumetric hydrogen uptake of MOF-5 by powder densification, *Int. J. Hydrogen Energy*, 2012, **37**, 2723–2727, DOI: 10.1016/j.ijhydene.2011.03.002.

29 J. Purewal, D. Liu, A. Sudik, M. Veenstra, J. Yang, S. Maurer, U. Mu and D. J. Siegel, Improved Hydrogen Storage and Thermal Conductivity in High-Density MOF-5

Composites, *J. Phys. Chem. C*, 2012, **116**, 20199–20212, DOI: 10.1021/jp305524f.

30 D. Liu, J. J. Purewal, J. Yang, A. Sudik, S. Maurer, U. Mueller, J. Ni and D. J. Siegel, MOF-5 composites exhibiting improved thermal conductivity, *Int. J. Hydrogen Energy*, 2012, **37**, 6109–6117, DOI: 10.1016/j.ijhydene.2011.12.129.

31 Y. Ming, J. Purewal, J. Yang, C. Xu, R. Soltis, J. Warner, M. Veenstra, M. Gaab, U. Mu and D. J. Siegel, Kinetic Stability of MOF-5 in Humid Environments: Impact of Powder Densification, Humidity Level, and Exposure Time, *Langmuir*, 2015, **31**, 4988–4995, DOI: 10.1021/acs.langmuir.5b00833.

32 R. Zacharia, D. Cossement, L. Lafi and R. Chahine, Volumetric hydrogen sorption capacity of monoliths prepared by mechanical densification of MOF-177, *J. Mater. Chem.*, 2010, **20**, 2145–2151, DOI: 10.1039/B922991D.

33 A. Dailly and E. Poirier, Environmental Science Evaluation of an industrial pilot scale densified MOF-177 adsorbent as an on-board hydrogen storage medium, *Energy Environ. Sci.*, 2011, **4**, 3527–3534, DOI: 10.1039/C1EE01426A.

34 N. Heymans, S. Vaesen and G. De Weireld, A complete procedure for acidic gas separation by adsorption on MIL-53 (Al), *Microporous Mesoporous Mater.*, 2012, **154**, 93–99, DOI: 10.1016/j.micromeso.2011.10.020.

35 M. A. Moreira, J. C. Santos, A. F. P. Ferreira, U. Müller, N. Trukhan, J. M. Loureiro and A. E. Rodrigues, Selective Liquid Phase Adsorption and Separation of ortho-Xylene with the Microporous MIL-53 (Al), *Sep. Sci. Technol.*, 2011, **46**, 1995–2003, DOI: 10.1080/01496395.2011.594481.

36 I. Majchrzak-kuce, Shaping metal–organic framework (MOF) powder materials for CO_2 capture applications—a thermogravimetric study, *J. Therm. Anal. Calorim.*, 2019, **138**, 4139–4144, DOI: 10.1007/s10973-019-08314-5.

37 R. P. P. L. Ribeiro, C. L. Antunes, A. U. Garate, A. F. Portela, M. G. Plaza, J. P. B. Mota and I. A. A. C. Esteves, Binderless shaped metal–organic framework particles: impact on carbon dioxide adsorption, *Microporous Mesoporous Mater.*, 2018, **275**, 111–121, DOI: 10.1016/j.micromeso.2018.08.002.

38 K. W. Chapman, G. J. Halder and P. J. Chupas, Pressure-Induced Amorphization and Porosity Modification in a Metal–Organic Framework, *J. Am. Chem. Soc.*, 2009, **131**, 17546–17547, DOI: 10.1021/ja908415z.

39 D. Bazer-bachi, L. Assié, V. Lecocq, B. Harbuzaru and V. Falk, Towards industrial use of metal–organic framework: impact of shaping on the MOF properties, *Powder Technol.*, 2014, **255**, 52–59, DOI: 10.1016/j.powtec.2013.09.013.

40 J. Zhu, C. Dai, N. Yang, L. Jiang and Z. Lei, Gas adsorption in shaped zeolitic imidazolate framework-8, *Chin. J. Chem. Eng.*, 2015, **23**, 1275–1282, DOI: 10.1016/j.cjche.2015.01.015.

41 O. Ardelean, G. Blanita, G. Borodi, M. D. Lazar, I. Misan, I. Coldea and D. Lupu, Volumetric hydrogen adsorption capacity of densified MIL-101 monoliths, *Int. J. Hydrogen Energy*, 2013, **38**, 7046–7055, DOI: 10.1016/j.ijhydene.2013.03.161.

42 H. Oh, D. Lupu, G. Blanita and M. Hirscher, Experimental assessment of physical upper limit for hydrogen storage capacity at 20 K in densified MIL-101 monoliths, *RSC Adv.*, 2014, **4**, 2648–2651, DOI: 10.1039/c3ra46233a.

43 G. Blanita, I. Coldea, I. Misan and D. Lupu, Hydrogen cryo-adsorption by hexagonal prism monoliths of MIL-101, *Int. J. Hydrogen Energy*, 2014, **39**, 17040–17046, DOI: 10.1016/j.ijhydene.2014.08.038.

44 G. Blanita, M. Streza, M. D. Lazar and D. Lupu, Kinetics of hydrogen adsorption in MIL-101 single pellets, *Int. J. Hydrogen Energy*, 2017, **42**, 3064–3077, DOI: 10.1016/j.ijhydene.2017.01.010.

45 M. Tagliabue, C. Rizzo, R. Millini, P. D. C. Dietzel, R. Blom and S. Zanardi, Methane storage on CPO-27-Ni pellets, *J. Porous Mater.*, 2011, **18**, 289–296, DOI: 10.1007/s10934-010-9378-0.

46 T. Remy, S. A. Peter, S. Van Der Perre, D. E. De Vos, G. V. Baron and J. F. M. Denayer, Selective Dynamic CO_2 Separations on Mg-MOF-74 at Low Pressures: A Detailed Comparison with 13X, *J. Phys. Chem. C*, 2013, **117**, 9301–9310, DOI: 10.1021/jp401923v.

47 G. W. Peterson, J. B. Decoste, T. G. Glover, Y. Huang, H. Jasuja and K. S. Walton, Effects of pelletization pressure on the physical and chemical properties of the metal–organic frameworks $Cu_3(BTC)_2$ and UiO-66, *Microporous Mesoporous Mater.*, 2013, **179**, 48–53, DOI: 10.1016/j.micromeso.2013.02.025.

48 J. Kim, S. Kim, S. Yang and W. Ahn, Bench-scale preparation of $Cu_3(BTC)_2$ by ethanol reflux: Synthesis optimization and adsorption / catalytic applications, *Microporous Mesoporous Mater.*, 2012, **161**, 48–55, DOI: 10.1016/j.micromeso.2012.05.021.

49 J. Dhainaut, J. Troyano, A. Legrand, J. Canivet, I. Imaz, D. Maspoch, H. Reinsch and D. Farrusseng, Systematic study of the impact of MOF densification into tablets on textural and mechanical properties, *CrystEngComm*, 2017, **19**, 4211–4218, DOI: 10.1039/C7CE00338B.

50 A. Terracina, M. Todaro, M. Mazaj, F. M. Gelardi and G. Buscarino, Unveiled the Source of the Structural Instability of HKUST-1 Powders upon Mechanical Compaction: Definition of a Fully Preserving Tableting Method, *J. Phys. Chem. C*, 2019, **123**, 1730–1741, DOI: 10.1021/acs.jpcc.8b08846.

51 G. W. Peterson, J. B. Decoste, F. Fatollahi-fard and D. K. Britt, Engineering UiO-66-NH2 for Toxic Gas Removal, *Nd. Eng. Chem. Res.*, 2014, **53**, 701–707, DOI: 10.1021/ie403366d.

52 M. A. Moreira, C. Santos, A. F. P. Ferreira, J. M. Loureiro, F. Ragon, P. Horcajada, K. Shim, Y. Hwang, U. Lee, J. Chang, C. Serre and E. Rodrigues, Reverse Shape Selectivity in the Liquid-Phase Adsorption of Xylene Isomers in Zirconium Terephthalate MOF UiO-66, *Langmuir*, 2012, **28**, 5715–5723, DOI: 10.1021/la3004118.

53 S. E. Bambalaza, H. W. Langmi, R. Mokaya, N. M. Musyoka and L. E. Khotseng, Compaction of a zirconium metal–organic framework (UiO-66) for high density hydrogen storage applications, *J. Mater. Chem. A*, 2018, **6**, 23569–23577, DOI: 10.1039/C8TA09227C.

54 S. Edubilli and S. Gumma, A systematic evaluation of UiO-66 metal organic framework for CO_2/N_2 separation, *Sep.*

Purif. Technol., 2019, **224**, 85–94, DOI: 10.1016/j.seppur.2019.04.081.

55 Y. Khabzina, J. Dhainaut, M. Ahlhelm, H. Richter, H. Reinsch, N. Stock and D. Farrusseng, Synthesis and Shaping Scale-up Study of Functionalized UiO-66 MOF for Ammonia Air Purification Filters, Ind. Eng. Chem. Res., 2018, **57**, 8200–8208, DOI: 10.1021/acs.iecr.8b00808.

56 J. Yang, H. Bai, F. Zhang, J. Liu, J. Winarta, Y. Wang and B. Mu, Effects of Activation Temperature and Densification on Adsorption Performance of MOF MIL-100 (Cr), J. Chem. Eng. Data, 2019, **64**, 5814–5823, DOI: 10.1021/acs.jced.9b00770.

57 A. H. Valekar, K. Cho, U. Lee, S. Lee, W. Yoon, Y. K. Hwang, G. Lee, J. Cho and J. Chang, Shaping of porous metal–organic framework granules using mesoporous r-alumina as a binder, RSC Adv., 2017, **7**, 55767–55777, DOI: 10.1039/C7RA11764G.

58 M. Taddei, M. J. McPherson, A. Gougsa, J. Lam and J. Sewell, An Optimised Compaction Process for Zr-fumarate (MOF-801), Inorganics, 2019, **7**, 110, DOI: 10.3390/inorganics7090110.

59 B. Kraushaar-Czarnetzki and S. P. Muller, in Shaping of Solid Catalysts, ed. K. P. de Jong, Synth. Solid Catal., 2009, pp. 173–199, DOI: 10.1002/9783527626854.ch9.

60 Y. Liu, D. Scharf and F. J. Clemens, Granulation processing parameters on the mechanical properties of diatomite-based porous granulates, Powder Technol., 2014, **263**, 159–167, DOI: 10.1016/j.powtec.2014.04.094.

61 G. Liu, J. Guo, F. Meng, X. Zhang and L. Wang, Effects of Colloidal Silica Binder on Catalytic Activity and Adhesion of HZSM-5 Coatings for Structured Reactors, Chin. J. Chem. Eng., 2014, **22**, 875–881, DOI: 10.1016/j.cjche.2014.06.010.

62 X. Kong and J. Liu, Influence of Alumina Binder Content on Catalytic Performance of Ni/HZSM-5 for Hydrodeoxygenation of Cyclohexanone, PLoS One, 2014, **9**, e101744, DOI: 10.1371/journal.pone.0101744.

63 M. S. Afarani, A. Samimi and E. B. Yekta, Synthesis of alumina granules by high shear mixer granulator: processing and sintering, Powder Technol., 2013, **237**, 32–40, DOI: 10.1016/j.powtec.2013.01.007.

64 T. M. Chitu, D. Oulahna, M. Hemati, T. M. Chitu, D. Oulahna, M. H. Wet, T. M. Chitu, D. Oulahna and M. Hemati, Wet granulation in laboratory scale high shear mixers: Effect of binder properties, Powder Technol., 2011, **206**, 25–33, DOI: 10.1016/j.powtec.2010.07.012.

65 G. T. Whiting, S. Chung, D. Stosic, A. D. Chowdhury, L. I. Van Der Wal, D. Fu, J. Zecevic, A. Travert, K. Houben, M. Baldus and B. M. Weckhuysen, Multiscale Mechanistic Insights of Shaped Catalyst Body Formulations and Their Impact on Catalytic Properties, ACS Catal., 2019, **9**, 4792–4803, DOI: 10.1021/acscatal.9b00151.

66 P. Perez-Uriarte, M. Gamero, A. Ateka, M. Diaz, A. T. Aguayo and J. Bilbao, Effect of the Acidity of HZSM-5 Zeolite and the Binder in the DME Transformation to Olefins, Ind. Eng. Chem. Res., 2016, **55**, 1513–1521, DOI: 10.1021/acs.iecr.5b04477.

67 A. Permyakova, O. Skrylnyk, E. Courbon and M. Affram, Synthesis Optimization, Shaping, and Heat Reallocation Evaluation of the Hydrophilic Metal–Organic Framework MIL-160 (Al), ChemSusChem, 2017, **10**, 1419–1426, DOI: 10.1002/cssc.201700164.

68 P. Kim, Y. You, H. Park, J. Chang, Y. Bae, C. Lee and J. Suh, Separation of SF_6 from SF_6/N_2 mixture using metal–organic framework MIL-100 (Fe) granule, Chem. Eng. J., 2015, **262**, 683–690, DOI: 10.1016/j.cej.2014.09.123.

69 V. D. Martins, R. A. Seabra, P. M. Silva, M. Ribeiro, K. H. Cho, U. Lee, J. Chang, M. Loureiro, A. E. Rodrigues and A. F. P. Ferreira, C_2/C_3 Hydrocarbon Separation by Pressure Swing Adsorption on MIL-100 (Fe), Ind. Eng. Chem. Res., 2020, **59**, 10568–10582, DOI: 10.1021/acs.iecr.0c00410.

70 P. Iacomi, U. Lee, A. H. Valekar, J. Chang and P. L. Llewellyn, Investigating the effect of alumina shaping on the sorption properties of promising metal–organic frameworks, RSC Adv., 2019, **9**, 7128–7135, DOI: 10.1039/c9ra00534j.

71 N. Chanut, A. D. Wiersum, U. Lee, K. Hwang, F. Ragon, H. Chevreau, S. Bourrelly, B. Kuchta, J. Chang, C. Serre and P. L. Llewellyn, Observing the Effects of Shaping on Gas Adsorption in Metal–Organic Frameworks, Eur. J. Inorg. Chem., 2016, 4416–4423, DOI: 10.1002/ejic.201600410.

72 S. Ohsaki, Y. Nakahara, H. Nakamura, S. Watano, M. Materials, Y. Nakahara, H. Nakamura and S. Watano, Flowability improvement of soft metal–organic framework particles by wet granulation, Microporous Mesoporous Mater., 2020, **293**, 109785, DOI: 10.1016/j.micromeso.2019.109785.

73 J. Ren, N. M. Musyoka, H. W. Langmi, A. Swartbooi, B. C. North and M. Mathe, A more efficient way to shape metal–organic framework (MOF) powder materials for hydrogen storage applications, Int. J. Hydrogen Energy., 2015, **40**, 4617–4622, DOI: 10.1016/j.ijhydene.2015.02.011.

74 S. Hindocha and S. Poulston, Study of the scale-up, formulation, ageing and ammonia adsorption capacity of MIL-100 (Fe), Cu-BTC and CPO-27 (Ni) for use in respiratory protection filters, Faraday Discuss, 2017, **201**, 113–125, DOI: 10.1039/c7fd00090a.

75 M. J. Regufe, J. Tamajon, A. M. Ribeiro, A. F. P. Ferreira, U. Lee, Y. K. Hwang, J. Chang, C. Serre, J. M. Loureiro and A. E. Rodrigues, Syngas Purification by Porous Amino-Functionalized Titanium Terephthalate MIL-125, Energy Fuels, 2015, **29**, 4654–4664, DOI: 10.1021/acs.energyfuels.5b00975.

76 M. Leloire, J. Dhainaut, P. Devaux, O. Leroy, H. Desjonqueres, S. Poirier, P. Nerisson, L. Cantrel, S. Royer, T. Loiseau and C. Volkringer, Stability and radioactive gaseous iodine-131 retention capacity of binderless UiO-66-NH_2 granules under severe nuclear accidental conditions, J. Hazard. Mater., 2021, **416**, 125890, DOI: 10.1016/j.jhazmat.2021.125890.

77 Z. Vajglova, N. Kumar, P. Arvela-Maki, K. Eranen, M. Peurla, L. Hupa, M. Nurmi, M. Toivakka and D. Y. Murzin, Synthesis and Physicochemical Characterization of Shaped Catalysts of β and Y Zeolites for Cyclization of Citronellal, Ind. Eng. Chem. Res., 2019, **58**, 18084–18096, DOI: 10.1021/acs.iecr.9b02829.

78 P. Kusgens, A. Zgaverdea, H. Fritz, S. Siegle and S. Kaskel, Metal–Organic Frameworks in Monolithic Structures, *J. Am. Ceram. Soc.*, 2010, **93**, 2476–2479, DOI: 10.1111/j.1551-2916.2010.03824.x.

79 G. Majano and J. Pérez-ramírez, Scalable Room-Temperature Conversion of Copper(II) Hydroxide into HKUST-1 (Cu₃(btc)₂), *Adv. Mater.*, 2013, **25**, 1052–1057, DOI: 10.1002/adma.201203664.

80 W. Y. Hong, S. P. Perera and A. D. Burrows, Manufacturing of metal–organic framework monoliths and their application in CO₂ adsorption, *Microporous Mesoporous Mater.*, 2015, **214**, 149–155, DOI: 10.1016/j.micromeso.2015.05.014.

81 W. Y. Hong, S. P. Perera and A. D. Burrows, Comparison of MIL-101 (Cr) metal–organic framework and 13X zeolite monoliths for CO₂ capture, *Microporous Mesoporous Mater.*, 2020, **308**, 110525, DOI: 10.1016/j.micromeso.2020.110525.

82 C. A. Grande, V. I. Águeda, A. Spjelkavik and R. Blom, An efficient recipe for formulation of metal–organic frameworks, *Chem. Eng. Sci.*, 2015, **124**, 154–158, DOI: 10.1016/j.ces.2014.06.048.

83 V. I. Agueda, J. A. Delgado, M. A. Uguina, P. Brea, A. I. Spjelkavik, R. Blom and C. Grande, Adsorption and diffusion of H₂, N₂, CO, CH₄ and CO₂ in UTSA-16 metal–organic framework extrudates, *Chem. Eng. Sci.*, 2015, **124**, 159–169, DOI: 10.1016/j.ces.2014.08.039.

84 J. A. Delgado, V. I. Águeda, M. A. Uguina, P. Brea and C. A. Grande, Comparison and evaluation of agglomerated MOFs in biohydrogen purification by means of pressure swing adsorption (PSA), *Chem. Eng. J.*, 2017, **326**, 117–129, DOI: 10.1016/j.cej.2017.05.144.

85 S. Pu, J. Wang, Z. Bao and Q. Yang, Performance Comparison of Metal–Organic Framework Extrudates and Commercial Zeolite for Ethylene/Ethane Separation, *Ind. Eng. Chem. Res.*, 2018, **57**, 1645–1654, DOI: 10.1021/acs.iecr.7b04391.

86 J. Cousin-Saint-Remi, A. Finoulst, C. Jabbour, G. V. Baron and J. F. M. Denayer, Selection of binder recipes for the formulation of MOFs into resistant pellets for molecular separations by fixed-bed adsorption, *Microporous Mesoporous Mater.*, 2020, **304**, 109322, DOI: 10.1016/j.micromeso.2019.02.009.

87 M. Kriesten, V. Schmitz, J. Siegel, C. E. Smith, M. Kaspereit and M. Hartmann, Shaping of Flexible Metal–Organic Frameworks: Combining Macroscopic Stability and Framework Flexibility, *Eur. J. Inorg. Chem.*, 2019, 4700–4709, DOI: 10.1002/ejic.201901100.

88 M. Klimakow, P. Klobes, A. F. Thunemann, K. Rademann and F. Emmerling, Mechanochemical Synthesis of Metal–Organic Frameworks: A Fast and Facile Approach toward Quantitative Yields and High Specific Surface Areas, *Chem. Mater.*, 2010, **22**, 5216–5221, DOI: 10.1021/cm1012119.

89 S. Tanaka, K. Kida, T. Nagaoka, T. Ota and Y. Miyake, Mechanochemical dry conversion of zinc oxide to zeolitic imidazolate framework, *Chem. Commun.*, 2013, **49**, 7884–7886, DOI: 10.1039/c3cc43028f.

90 A. M. Fidelli, B. Karadeniz, A. J. Howarth, I. Huskic, L. S. Germann, I. Halasz, M. Etter, S.-Y. Moon, R. E. Dinnebier,

V. Stilinovic, O. K. Farha, T. Friscic and K. Uzarevic, Green and rapid mechanosynthesis of high-porosity NU- and UiO-type metal–organic frameworks, *Chem. Commun.*, 2018, **54**, 6999–7002, DOI: 10.1039/C8CC03189D.

91 D. Lv, Y. Chen, Y. Li, R. Shi, H. Wu, X. Sun, J. Xiao, H. Xi, Q. Xia and Z. Li, Efficient Mechanochemical Synthesis of MOF-5 for Linear Alkanes Adsorption, *J. Chem. Eng. Data.*, 2017, **62**, 2030–2036, DOI: 10.1021/acs.jced.7b00049.

92 D. Crawford, J. Casaban, R. Haydon, N. Giri, T. McNally and S. L. James, Synthesis by extrusion: continuous, large-scale preparation of MOFs using little or no solvent, *Chem. Sci.*, 2015, **6**, 1645–1649, DOI: 10.1039/c4sc03217a.

93 T. D. Ngo, A. Kashani, G. Imbalzano, K. T. Q. Nguyen and D. Hui, Additive manufacturing (3D printing): a review of materials, methods, applications and challenges, *Composites, Part B*, 2018, **143**, 172–196, DOI: 10.1016/j.compositesb.2018.02.012.

94 V. G. Rocha, E. Saiz, L. S. Tirichenko and E. García-Tuñón, Direct ink writing advances in multi-material structures for a sustainable future, *J. Mater. Chem. A*, 2020, **8**, 15646–15657, DOI: 10.1039/D0TA04181E.

95 J. Azuaje, C. R. Tubío, L. Escalante, M. Gómez, F. Guitián, A. Coelho, O. Caamaño, A. Gil and E. Sotelo, An Efficient and Recyclable 3D Printed α-Al₂O₃ Catalyst for the Multi-component Assembly of Bioactive Heterocycles, *Appl. Catal., A*, 2017, **530**, 203–210, DOI: 10.1016/j.apcata.2016.11.031.

96 H. V. Thakkar, S. Eastman, A. Hajari, A. A. Rownaghi, J. C. Knox and F. Rezaei, 3D-Printed Zeolite Monoliths for CO Removal from Enclosed Environments, *ACS Appl. Mater. Interfaces*, 2016, **8**, 27753–27761, DOI: 10.1021/acsami.6b09647.

97 J. P. Lewicki, J. N. Rodriguez, C. Zhu, M. A. Worsley, A. S. Wu, Y. Kanarska, J. D. Horn, E. B. Duoss, J. M. Ortega, W. Elmer, R. Hensleigh, R. A. Fellini and M. J. King, 3D-Printing of Meso-structurally Ordered Carbon Fiber/Polymer Composites with Unprecedented Orthotropic Physical Properties, *Sci. Rep.*, 2017, **7**, 1–14, DOI: 10.1038/srep43401.

98 H. Thakkar, S. Eastman, A. Al-mamoori, A. Hajari, A. A. Rownaghi, F. Rezaei, H. Thakkar, S. Eastman, A. Al-mamoori, A. Hajari and A. A. Rownaghi, Formulation of Aminosilica Adsorbents into 3D-Printed Monoliths and Evaluation of their CO₂ Capture Performance, *ACS Appl. Mater. Interfaces.*, 2017, **9**, 7489–7498, DOI: 10.1021/acsami.6b16732.

99 C. Parra-Cabrera, C. Achille, S. Kuhn, R. Ameloot and C. Parra-cabrera, 3D printing in chemical engineering and catalytic technology: structured catalysts, mixers and reactors, *Chem. Soc. Rev.*, 2018, **47**, 209–230, DOI: 10.1039/C7CS00631D.

100 Z. Wang, J. Wang, M. Li, K. Sun and C. Liu, Three-dimensional Printed Acrylonitrile with Cu-BTC Metal–organic Frameworks for the Removal of Methylene Blue, *Sci. Rep.*, 2014, **4**, 1–7, DOI: 10.1038/srep05939.

101 Z. Shi, C. Xu, F. Chen, Y. Wang, L. Li, Q. Meng and R. Zhang, Renewable metal–organic-frameworks-coated

3D printing film for removal of malachite green, *RSC Adv.*, 2017, **7**, 49947–49952, DOI: 10.1039/c7ra10912a.

102 S. Lawson, Q. Al-naddaf, A. Krishnamurthy, M. S. Amour, C. Griffin, A. A. Rownaghi, J. C. Knox and F. Rezaei, UTSA-16 Growth within 3D-Printed Co-Kaolin Monoliths with High Selectivity for CO_2/CH_4, CO_2/N_2, and CO_2/H_2 Separation, *ACS Appl. Mater. Interfaces*, 2018, **10**, 19076–19086, DOI: 10.1021/acsami.8b05192.

103 D. Liu, P. Jiang, X. Li, J. Liu, L. Zhou, X. Wang and F. Zhou, 3D printing of metal–organic frameworks decorated hierarchical porous ceramics for high-efficiency catalytic degradation, *Chem. Eng. J.*, 2020, **397**, 125392, DOI: 10.1016/j.cej.2020.125392.

104 M. C. Kreider, J. A. Fedchak, J. Scherschligt, E. Abigail, N. Nikolai, Z. Ahmed and M. R. Hartings, Toward 3D printed hydrogen storage materials made with ABS-MOF composites, *Polym. Adv. Technol.*, 2017, **29**, 867–873, DOI: 10.1002/pat.4197.

105 M. Bible, M. Sefa, J. A. Fedchak, J. Scherschligt, B. Natarajan, Z. Ahmed and M. R. Hartings, 3D-Printed Acrylonitrile Butadiene Styrene-Metal Organic Framework Composite Materials and Their Gas Storage Properties, 3D Print, *Addit. Manuf.*, 2018, **5**, 63–72, DOI: 10.1089/3dp.2017.0067.

106 K. A. Evans, Z. C. Kennedy, B. W. Arey, J. F. Christ, H. T. Schaef, S. K. Nune and R. L. Erikson, Chemically Active, Porous 3D-Printed Thermoplastic Composites, *ACS Appl. Mater. Interfaces*, 2018, **10**, 15112–15121, DOI: 10.1021/acsami.7b17565.

107 H. Thakkar, S. Eastman, Q. Al-naddaf, A. A. Rownaghi and F. Rezaei, 3D-Printed Metal−Organic Framework Monoliths for Gas Adsorption Processes, *ACS Appl. Mater. Interfaces*, 2017, **9**, 35908–35916, DOI: 10.1021/acsami.7b11626.

108 H. Thakkar, Q. Al-naddaf, N. Legion, M. Hovis, A. Krishnamurthy, A. A. Rownaghi and F. Rezaei, Adsorption of Ethane and Ethylene over 3D-Printed Ethane-Selective Monoliths, ACS Sustain, *Chem. Eng.*, 2018, **6**, 15228–15237, DOI: 10.1021/acssuschemeng.8b03685.

109 S. Lawson, C. Gri, K. Rapp, A. A. Rownaghi and F. Rezaei, Amine-Functionalized MIL-101 Monoliths for CO_2 Removal from Enclosed Environments, *Energy Fuels*, 2019, **33**, 2399–2407, DOI: 10.1021/acs.energyfuels.8b04508.

110 S. Lawson, M. Snarzyk, D. Hanify, A. A. Rownaghi and F. Rezaei, Development of 3D-Printed Polymer-MOF Monoliths for CO_2 Adsorption, *Ind. Eng. Chem. Res.*, 2020, **59**, 7151–7160, DOI: 10.1021/acs.iecr.9b05445.

111 S. Lawson, A. Alwakwak, A. A. Rownaghi and F. Rezaei, Gel−Print−Grow: A New Way of 3D Printing Metal−Organic Frameworks, *ACS Appl. Mater. Interfaces*, 2020, **12**, 56108–56117, DOI: 10.1021/acsami.0c18720.

112 J. Lefevere, B. Claessens, S. Mullens, G. Baron, J. Cousin-saint-remi and J. F. M. Denayer, 3D-Printed Zeolitic Imidazolate Framework Structures for Adsorptive Separations, *ACS Appl. Nano Mater.*, 2019, **2**, 4991–4999, DOI: 10.1021/acsanm.9b00934.

113 B. Claessens, N. Dubois, J. Lefevere, S. Mullens, J. Cousin-saint-remi and J. F. M. Denayer, 3D-Printed ZIF-8 Monoliths for Biobutanol Recovery, *Ind. Eng. Chem. Res.*, 2020, **59**, 8813–8824, DOI: 10.1021/acs.iecr.0c00453.

114 Z. Lyu, G. J. H. Lim, R. Guo, Z. Kou, T. Wang, C. Guan, J. Ding, W. Chen and J. Wang, 3D-Printed MOF-Derived Hierarchically Porous Frameworks for Practical High-Energy Density LiO_2 Batteries, *Adv. Funct. Mater.*, 2019, **29**, 1806658, DOI: 10.1002/adfm.201806658.

115 J. Dhainaut, M. Bonneau, R. Ueoka, K. Kanamori and S. Furukawa, Formulation of Metal–Organic Framework Inks for the 3D Printing of Robust Microporous Solids Towards High-Pressure Gas Storage and Separation, *ACS Appl. Mater. Interfaces*, 2020, **12**, 10983–10992, DOI: 10.1021/acsami.9b22257.

116 R. Pei, L. Fan, F. Zhao, J. Xiao, Y. Yang, A. Lai, S. Zhou and G. Zhan, 3D-Printed metal–organic frameworks within biocompatible polymers as excellent adsorbents for organic dyes removal, *J. Hazard. Mater.*, 2020, **384**, 121418, DOI: 10.1016/j.jhazmat.2019.121418.

117 G. J. H. Lim, Y. Wu, B. B. Shah, J. J. Koh, C. K. Liu, D. Zhao, A. K. Cheetham, J. Wang and J. Ding, 3D-Printing of Pure Metal–Organic Framework Monoliths, *ACS Mater. Lett.*, 2019, **1**, 147–153, DOI: 10.1021/acsmaterialslett.9b00069.

118 C. A. Grande, R. Blom, V. Middelkoop, D. Matras, A. Vamvakeros, S. D. M. Jacques, A. M. Beale, M. Di, K. Anne and A. M. Bouzga, Multiscale investigation of adsorption properties of novel 3D printed UTSA-16 structures, *Chem. Eng. J.*, 2020, **402**, 126166, DOI: 10.1016/j.cej.2020.126166.

119 S. Sultan, H. N. Abdelhamid, X. Zou and A. P. Mathew, CelloMOF: Nanocellulose Enabled 3D Printing of Metal–Organic Frameworks, *Adv. Funct. Mater.*, 2018, **29**, 1805372, DOI: 10.1002/adfm.201805372.

120 A. J. Young, R. Guillet-Nicolas, E. S. Marshall, F. Kleitz, A. J. Goodhand, L. B. L. Glanville, M. R. Reithofer and J. M. Chin, Direct ink writing of catalytically active UiO-66 polymer composites, *Chem. Commun.*, 2019, **55**, 2190–2193, DOI: 10.1039/c8cc10018g.

121 O. Halevi, J. M. R. Tan, P. S. Lee and S. Magdassi, Hydrolytically Stable MOF in 3D-Printed Structures, *Adv. Sustainable Syst.*, 2018, **2**, 1700150, DOI: 10.1002/adsu.201700150.

122 W. Liu, O. Erol and D. H. Gracias, 3D Printing of an In Situ Grown MOF Hydrogel with Tunable Mechanical Properties, *ACS Appl. Mater. Interfaces*, 2020, **12**, 33267–33275, DOI: 10.1021/acsami.0c08880.

123 R. Li, S. Yuan, W. Zhang, H. Zheng and W. Zhu, 3D printing of mixed matrix films based on metal–organic frameworks and thermoplastic polyamide 12 by selective laser sintering for water applications, *ACS Appl. Mater. Interfaces*, 2019, **11**, 40564–40574, DOI: 10.1021/acsami.9b11840.

124 E. Lahtinen, R. L. M. Precker, M. Lahtinen and E. Hey-hawkins, Selective Laser Sintering of Metal–Organic Frameworks: Production of Highly Porous Filters by 3D Printing onto a Polymeric Matrix, *ChemPlusChem*, 2019, **84**, 222–225, DOI: 10.1002/cplu.201900081.

125 A. Gharsallaoui, G. Roudaut, O. Chambin, A. Voilley and R. Saurel, Applications of spray-drying in microencapsulation

of food ingredients: An overview, *Food Res. Int.*, 2007, **40**, 1107–1121, DOI: 10.1016/j.foodres.2007.07.004.

126 A. Sosnik and K. P. Seremeta, Advantages and challenges of the spray-drying technology for the production of pure drug particles and drug-loaded polymeric carriers, *Adv. Colloid Interface Sci.*, 2015, **223**, 40–54, DOI: 10.1016/j.cis.2015.05.003.

127 B. Vertruyen, N. Eshraghi, C. Piffet, J. Bodart, A. Mahmoud and F. Boschini, Spray-Drying of Electrode Materials for Lithium- and Sodium-Ion Batteries, *Materials*, 2018, **11**, 1076, DOI: 10.3390/ma11071076.

128 J. Troyano, C. Ceren, L. Garzo, A. Carne, I. Imaz and D. Maspoch, Spray-Drying Synthesis of MOFs, COFs, and Related Composites, *Acc. Chem. Res.*, 2020, **53**, 1206–1217, DOI: 10.1021/acs.accounts.0c00133.

129 C. du Fresne von Hohenesche, V. Stathopoulos, K. K. Unger, A. Lind and M. Linden, Formation of hierarchically ordered silicas prepared by spray drying of nanosized spheres, *Stud. Surf. Sci. Catal.*, 2002, **144**, 339–346, DOI: 10.1016/S0167-2991(02)80153-7.

130 A. B. D. Nandiyanto, T. Ogi, W.-N. Wang, L. Gradon and K. Okuyama, Template-assisted spray-drying method for the fabrication of porous particles with tunable structures, *Adv. Powder Technol.*, 2019, **30**, 2908–2924, DOI: 10.1016/j.apt.2019.08.037.

131 A. Carne-Sanchez, I. Imaz, M. Cano-Sarabia and D. Maspoch, A spray-drying strategy for synthesis of nanoscale metal–organic frameworks and their assembly into hollow superstructures, *Nat. Chem.*, 2013, **5**, 203–211, DOI: 10.1038/nchem.1569.

132 J. Huo, M. Brightwell, S. El Hankari, A. Garai and D. Bradshaw, A versatile, industrially relevant, aqueous room temperature synthesis of HKUST-1 with high space-time yield, *J. Mater. Chem. A*, 2013, **1**, 15220–15223, DOI: 10.1039/C3TA14409G.

133 A. Carné-Sánchez, K. C. Stylianou, C. Carbonell, M. Naderi, I. Imaz and D. Maspoch, Protecting Metal–Organic Framework Crystals from Hydrolytic Degradation by Spray-Dry Encapsulating Them into Polystyrene Microspheres, *Adv. Mater.*, 2015, **27**, 869–873, DOI: 10.1002/adma.201403827.

134 S. Tanaka and R. Miyashita, Aqueous-System-Enabled Spray-Drying Technique for the Synthesis of Hollow Polycrystalline ZIF-8 MOF Particles, *ACS Omega*, 2017, **2**, 6437–6445, DOI: 10.1021/acsomega.7b01325.

135 Y.-R. Lee, M.-S. Jang, H.-Y. Cho, H.-J. Kwon, S. Kim and W.-S. Ahn, ZIF-8: a comparison of synthesis methods, *Chem. Eng. J.*, 2015, **271**, 276–280, DOI: 10.1016/j.cej.2015.02.094.

136 S. Chaemchuen, K. Zhou, B. Mousavi, M. Ghadamyari, P. M. Heynderickx, S. Zhuiykov, M. S. Yusubov and F. Verpoort, Spray drying of zeolitic imidazolate frameworks: investigation of crystal formation and properties, *CrystEngComm*, 2018, **20**, 3601–3608, DOI: 10.1039/C8CE00392K.

137 Y. Mitsuka, K. Nagashima, H. Kobayashi and H. Kitagawa, A Seed-mediated Spray-drying Method for Facile Syntheses of Zr-MOF and a Pillared-layer-type MOF, *Chem. Lett.*, 2016, **45**, 1313–1315, DOI: 10.1246/cl.160651.

138 L. Garzón-Tovar, M. Cano-Sarabia, C. Carbonell, I. Imaz and D. Maspoch, A spray-drying continuous-flow method for simultaneous synthesis and shaping of microspherical high nuclearity MOF beads, *React. Chem. Eng.*, 2016, **1**, 533–539, DOI: 10.1039/C6RE00065G.

139 S. Bae, N. Zaini, K. S. N. Kamarudin, K. S. Yoo, J. Kim and M. Roslee, Rapid solvothermal synthesis of microporous UiO-66 particles for carbon dioxide capture, *Korean J. Chem. Eng.*, 2018, **35**, 764–769, DOI: 10.1007/s11814-017-0334-4.

140 M. J. Katz, Z. J. Brown, Y. J. Colon, P. W. Siu, K. A. Scheidt, R. Q. Snurr, J. T. Hupp and O. K. Farha, A facile synthesis of UiO-66, UiO-67 and their derivatives, *Chem. Commun.*, 2013, **49**, 9449–9451, DOI: 10.1039/C3CC46105J.

141 C. Avci-Camur, J. Troyano, J. Pérez-Carvajal, A. Legrand, D. Farrusseng, I. Imaz and D. Maspoch, Aqueous production of spherical Zr-MOF beads *via* continuous-flow spray-drying, *Green Chem.*, 2018, **20**, 873–878, DOI: 10.1039/C7GC03132G.

142 G. C. Shearer, S. Chavan, S. Bordiga, S. Svelle, U. Olsbye and K. P. Lillerud, Defect Engineering: Tuning the Porosity and Composition of the Metal–Organic Framework UiO-66 via Modulated Synthesis, *Chem. Mater.*, 2016, **28**, 3749–3761, DOI: 10.1021/acs.chemmater.6b00602.

143 G. Boix, J. Troyano, L. Carlos, G. Tovar, C. Camur, N. Bermejo, A. Yazdi, J. Piella, N. G. Bastús, V. Puntes, I. Imaz and D. Maspoch, MOF-Beads containing inorganic nanoparticles for the simultaneous removal of multiple heavy metals from water, *ACS Appl. Mater. Interfaces*, 2020, **12**, 10554–10562, DOI: 10.1021/acsami.9b23206.

144 G. Boix, X. Han, I. Imaz and D. Maspoch, Millimeter-Shaped Metal–Organic Framework/Inorganic Nanoparticle Composite as a New Adsorbent for Home Water-Purification Filters, *ACS Appl. Mater. Interfaces.*, 2021, **13**, 17835–17843, DOI: 10.1021/acsami.1c02940.

145 A. I. Spjelkavik, S. Divekar, T. Didriksen and R. Blom, Forming MOFs into Spheres by Use of Molecular Gastronomy Methods, *Chem. – Eur. J.*, 2014, **20**, 1–7, DOI: 10.1002/chem.201402464.

146 D. W. Lee, T. Didriksen, U. Olsbye, R. Blom and C. A. Grande, Shaping of metal–organic framework UiO-66 using alginates: Effect of operation variables, *Sep. Purif. Technol.*, 2020, **235**, 116182, DOI: 10.1016/j.seppur.2019.116182.

147 D. Farrusseng, C. Daniel, C. Hamill, J. Casaban, T. Didriksen, R. Blom, A. Velte, G. Fueldner, P. Gantenbein, P. Persdorf, X. Daguenet-Frick and F. Meunier, Adsorber heat exchanger using Al-fumarate beads for heat-pump application – a transport study, *Faraday Discuss*, 2020, **225**, 384–402, DOI: 10.1039/D0FD00009D.

148 S. Yang, L. Peng, O. A. Syzgantseva, O. Trukhina, I. Kochetygov, A. Justin, D. T. Sun, H. Abedini, M. A. Syzgantseva, E. Oveisi, G. Lu and W. L. Queen, Preparation of Highly Porous Metal–Organic Framework Beads for Metal Extraction from Liquid Streams, *J. Am. Chem. Soc.*, 2020, **142**, 13415–13425, DOI: 10.1021/jacs.0c02371.

149 X.-X. Liang, N. Wang, Y. Qu, L.-Y. Yang, Y.-G. Wang and X.-K. Ouyang, Facile Preparation of Metal–Organic Framework

(MIL-125)/Chitosan Beads for Adsorption of Pb(II) from Aqueous Solutions, *Molecules*, 2018, **23**, 1524, DOI: 10.3390/molecules23071524.

150 A. M. Omer, E. M. A. El-monaem, M. M. A. El-latif, G. M. El-subruiti and A. S. Eltaweil, Facile fabrication of novel magnetic ZIF-67 MOF@aminated chitosan composite beads for the adsorptive removal of Cr(VI) from aqueous solutions, *Carbohydr. Polym.*, 2021, **265**, 118084, DOI: 10.1016/j.carbpol.2021.118084.

151 B. J. Riley, W. Kuang, T. Varga, S. Ahmed, M. Galanek, J. Li, Z. Nelson and P. K. Thallapally, Metal–organic framework-polyacrylonitrile composite beads for xenon capture, *ACS Appl. Mater. Interfaces.*, 2020, **12**, 45342–45350, DOI: 10.1021/acsami.0c13717.

152 J. Park, Y. S. Chae, D. W. Kang, M. Kang, J. H. Choe, S. Kim, J. Y. Kim, Y. W. Jeong and C. S. Hong, Shaping of a Metal−Organic Framework − Polymer Composite and Its CO$_2$ Adsorption Performances from Humid Indoor Air, *ACS Appl. Mater. Interfaces.*, 2021, **13**, 25421–25427, DOI: 10.1021/acsami.1c06089.

153 S. Gökpinar, S. Ernst, E. Hastürk, M. Möllers, E. Aita, R. Wiedey, N. Tannert, S. Nießing, S. Abdpour, J. Quodbach, G. Füldner, S. K. Henninger and C. Janiak, Air-con Metal–Organic Frameworks in Binder Composites for Water Adsorption Heat Transformation Systems, *Ind. Eng. Chem. Res.*, 2019, **58**, 21493–21503, DOI: 10.1021/acs.iecr.9b04394.

154 E. Hastürk, C. Schlüsener, J. Quodbach, A. Schmitz and C. Janiak, Shaping of metal–organic frameworks into mechanically stable monoliths with poly(vinyl alcohol) by

155 Y. Hara, K. Kanamori and K. Nakanishi, Self-Assembly of Metal–Organic Frameworks into Monolithic Materials with Highly Controlled Trimodal Pore Structures, *Angew. Chem., Int. Ed.*, 2019, **58**, 19047–19053, DOI: 10.1002/anie.201911499.

156 A. Ahmed, T. Hasell, R. Clowes, P. Myers, A. I. Cooper and H. Zhang, Aligned macroporous monoliths with intrinsic microporosity via a frozen-solvent-templating approach, *Chem. Commun.*, 2015, **51**, 1717–1720, DOI: 10.1039/C4CC08919G.

157 Q. Fu, L. Wen, L. Zhang, X. Chen, D. Pun, A. Ahmed, Y. Yang and H. Zhang, Preparation of Ice-templated MOF-polymer composite monoliths and their application for wastewater treatment with high capacity and easy recycling, *ACS Appl. Mater. Interfaces*, 2017, **9**, 33979–33988, DOI: 10.1021/acsami.7b10872.

158 Q. Fu, L. Zhang, H. Zhang, X. Chen, M. Li and M. Gong, Ice- and MOF-templated porous carbonaceous monoliths for adsorptive removal of dyes in water with easy recycling, *Environ. Res.*, 2020, **186**, 109608, DOI: 10.1016/j.envres.2020.109608.

159 Q. Fu, L. Wen, L. Zhang, X. Chen and H. Zhang, Porous Carbon and Carbon/Metal Oxide Composites by Ice Templating and Subsequent Pyrolysis, *Ind. Eng. Chem. Res.*, 2019, **58**, 14312–14322, DOI: 10.1021/acs.iecr.9b01081.

160 T. Tian, J. Velazquez-Garcia, T. D. Bennett and D. Fairen-Jimenez, Mechanically and chemically robust ZIF-8 monoliths with high volumetric adsorption capacity, *J. Mater. Chem. A*, 2015, **3**, 2999–3005, DOI: 10.1039/c4ta05116e.

phase separation technique, *Microporous Mesoporous Mater.*, 2019, **280**, 277–287, DOI: 10.1016/j.micromeso.2019.02.011.